Summer 5-10-2018

SPLIT-RING RESONATOR WAVEGUIDE STRUCTURE CHARACTERIZATION BY SIMULATIONS, MEASUREMENTS AND LINEAR TIME-INVARIANT MODELING

Mohamed Aziz Hmaidi
University of New Mexico

Mohamed Aziz Hmaidi

Candidate

Electrical and Computer Engineering

Department

This thesis is approved, and it is acceptable in quality and form for publication:

Approved by the Thesis Committee:

Dr. Mark Gilmore, Chairperson

Dr. Edl Schamiloglu

Dr. Christos Christodoulou

SPLIT-RING RESONATOR WAVEGUIDE STRUCTURE CHARACTERIZATION BY SIMULATIONS, MEASUREMENTS AND LINEAR TIME-INVARIANT MODELING

by

MOHAMED AZIZ HMAIDI

NATIONAL ENGINEERING DEGREE IN INSTRUMENTATION AND INDUSTRIAL MAINTENANCE INSTITUT NATIONAL DES SCIENCES APPLIQUEES ET DE TECHNOLOGIE, 2013

THESIS

Submitted in Partial Fulfillment of the
Requirements for the Degree of

Master of Science
Electrical Engineering

The University of New Mexico
Albuquerque, New Mexico

July 2018

DEDICATION

A mes parents Najoua et Hamdi,

Ma plus grande fierté dans la vie est d'être votre progéniture,

A Selim et Nour,

Sans qui la vie serait morose, terne et insipide,

A Aymen,

Qui a redéfini le sens du mot amitié,

A Nana Saida Khadija,

Parce que tu n'as jamais quitté mes pensées,

Tu me manques.

ACKNOWLEDGEMENTS

I would like to thank Dr. Gilmore for his advisement and guidance throughout the duration of this Master's degree. The help and support that you provided since my first day in this track is immeasurably valuable.

I would like to thank as well Dr. Schamiloglu and Dr. Christodoulou for taking the time to assess this work and for their valuable feedback.

Thank you especially to all the people that I had the chance to meet in the Plasma and Fusion Science Lab, from post-docs to Bachelor, Master and Phd students for their friendliness and their insightful feedback.

Thank you to Dr. Firas Ayoub, Dr. Joseph Costantine and the Antennas' laboratory peers for the help and guidance in running simulations and experiments.

Thank you to the friends that I met here and that kept supporting me through hard times and providing me with essential moral support.

Thank you to my family, Najoua, Hamdi, Selim and Nour, my friends Aymen, Malek, Nesrine, Nader, Salaheddine and all my friends in Tunisia for the emotional support, shipped through thousands of miles.

Thank you, Tunisia, for providing me with free education, which filled me with the necessary knowledge and ambition that I needed to take part in this curriculum.

Thank you, Erin, for everything.

This research was supported by AFOSR MURI Grant FA9550-12-1-0489.

SPLIT-RING RESONATOR WAVEGUIDE STRUCTURE CHARACTERIZATION BY SIMULATIONS, MEASUREMENTS AND LINEAR TIME-INVARIANT MODELING

by

Mohamed Aziz Hmaidi

National Engineering Degree Instrumentation and Industrial Maintenance,
Institut National des Sciences Appliquées et de Technologie, 2013

M.S., Electrical Engineering,
University of New Mexico2018

ABSTRACT

Interest in Metamaterials has been rising drastically in the recent years as they have been used in several optical and RF applications, from antennas to perfect lenses and pulsed power devices. Nevertheless, the time-behavior of metamaterials remains opaque and poorly understood.

In this research work, characterization of a metamaterial structure in time and frequency-domain was made through simulations and experiments. The structure consists in a series of edge-side coupled Split Ring Resonators (SRRs) in a below cutoff waveguide. A linear time invariant model of distributed elements has been elaborated as well in an attempt to approach the structure's behavior. The comparison between simulations, measurements and model demonstrated agreement and confirmed qualitatively behavior that was previously observed in similar structures. The linear model constitutes a basis for further studies to understand metamaterial behavior or for the design of metamaterial with controlled characteristics.

Table of Contents

Table of Figures

1. Chapter 1: Introduction Motivation and Theory Review

This thesis details the work done on frequency and time-domain behavior of split-ring resonators (SRR) inside a cutoff waveguide structure. This research aims to explain and model more in depth the temporal behavior of the structure to get a better understanding of split-ring resonator structures and metamaterials on a general level. In particular, this research focuses on creating a model that maps the frequency and time behavior. The model seeks to draw the strength of linear distributed models.

In this first chapter, the history and applications of metamaterials are presented, followed by a theory review of metamaterials and double negative media. Design examples for split ring resonators, and the SRR-waveguide based systems are highlighted. Modeling techniques for such systems, like left-handed and right left-handed transmission lines are discussed as well.

1.1. History and Applications of Metamaterials

1.1.1. History of Metamaterials

The prefix "meta" generally defines a new discipline that is related to the original one described by the original word that the prefix is attached to. In the electromagnetics' field, the definition of metamaterials is used in a very generic way. In fact, the word designates any material with properties that are inexistent in nature. The word then designates man-made, engineered materials with "uncommon" or "exotic" properties. These properties include negative refraction index, and phase and group velocities that have opposite signs. These properties will be discussed in detail in the following chapters. The definition includes a wide range of materials: "Double Positive" (DPS), "Double Negative" (DNG), or "Single Negative" (SNG)

metamaterials among others. The negative and positive denomination is related to the sign of the constitutive electromagnetic parameters of the medium; the electric permittivity (ε) and the magnetic permeability (μ).

The idea of the first metamaterials arises from assumptions made by Viktor Veselago in the 1960's [15]. Veselago hypothetically considered the implications of negative constitutive parameters to obtain a negative refraction index. This idea didn't get much interest until Pendry's publication about the matter in the 1990's [1]. He presented a way of creating negative magnetic permeability by creating a periodic structure with metallic wires. The design evolved then into thin cylindrical sheets with an internal structure that has a capacitance to lead finally to his famous design of split-ring resonators. Since then, Pendry's original design has been used for multiple structure and applications. It also laid the ground for the design for other split ring-resonator designs [1]. Figure 1 presents some of Pendry's designs; from left to right, the wire array medium, cylindrical sheets and his first split-ring resonator (SRR) design. Figure 1 shows the evolution of Pendry's designs and that lead to the first SRR.

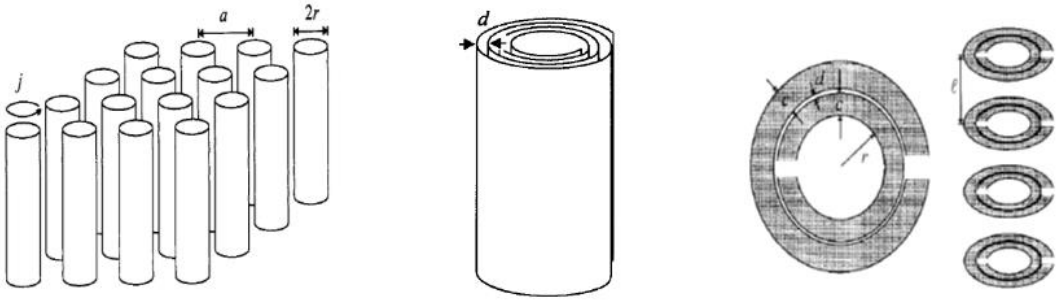

FIGURE 1: PENDRY'S MULTIPLE DESIGNS

LEFT: WIRE ARRAY, CENTER: CYLINDRICAL SHEETS, RIGHT: SRR FIRST DESIGN [1]

After the interest in these structures was triggered, several research initiatives were published, confirming theoretically and experimentally the properties of Split Ring Resonators. In 2000, Smith [2] formulated expressions of permeability and

permittivity of a Left-Handed medium. In 2001, Shelby et al. conducted an experiment proving the negative refraction index using a two-dimensional array of SRR and copper strips. By measuring the refraction angle from the medium, they were able then to confirm the negativity of the index [3]. Figure 2 illustrates the experimental set-up as well as the negative refractive index results obtained. Following that in 2002, Smith et al. [4] confirmed the antiparallel group and phase velocity properties of LHM by studying modulated waves at the interface between a positive and negative refractive index material. The work done by Foteinopoulou et al. [5] confirmed the negative refraction and studied the evolution of the electromagnetic waves as they hit the interface between the media using FDTD techniques.

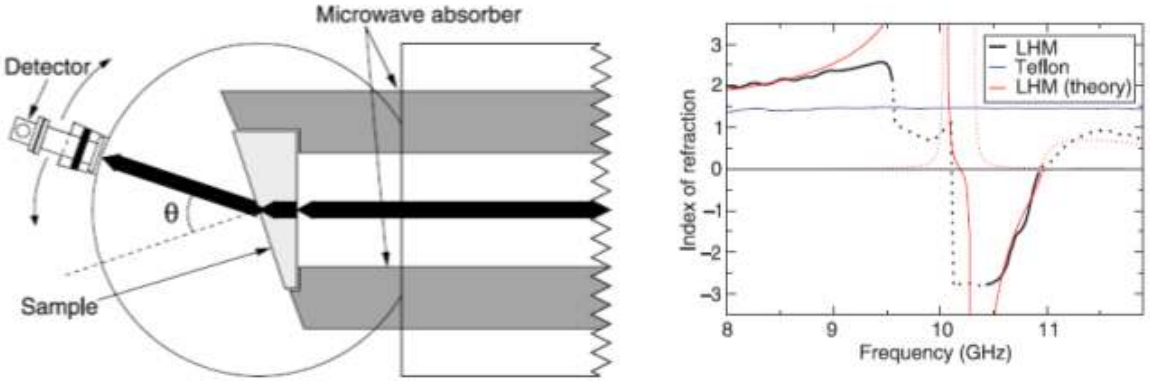

FIGURE 2: LEFT: SHELBY ET AL. EXPERIMENTAL SET UP FOR NEGATIVE REFRACTION INDEX MEASUREMENT, RIGHT: NEGATIVE REFRACTION INDEX FOR THEORETICAL AND EXPERIMENTAL LHM AND TEFLON [3]

Marques et al. [6] presented several achievements related to metamaterial, from exhibiting the interest of the bi-anisotropy properties of SRRs, modeling SRRs with distributed circuit elements carrying out experiments of SRR in a cutoff Waveguide

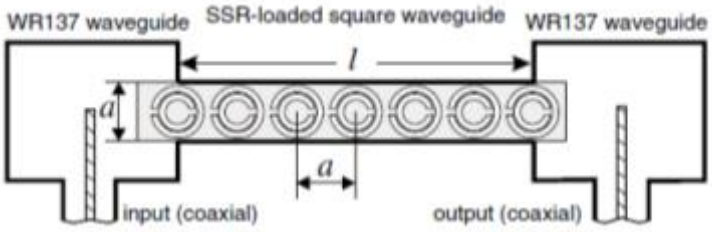

FIGURE 3: BAENA'S EXPERIMENTAL SET UP OF SRR IN WG BELOW CUTOFF [6]

and showing propagation in waveguides below cutoff. In the meantime, Caloz contributed to the matter by introducing distributed models for the Left-Handed materials. He considered the medium as transmission lines that have reactive distributed elements that fulfill the left-handedness properties of Metamaterial [7].

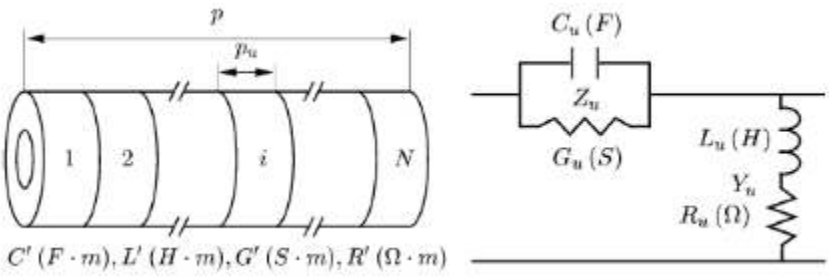

FIGURE 4 : LEFT: LHTL DIVIDED IN UNIT CELLS - RIGHT: UNIT CELL TRANSMISSION LINE MODEL [7]

The model was extended then to Left-Right Handed transmission lines which is a model that includes the parasitic inductances and capacitances of the medium and give a more accurate approximation than the pure left-handed transmission line [8]. More recently, the interest of the Air Force Office of Scientific Research in the Metamaterial field led to the reproduction of experiments at different frequencies confirming the SRR properties [9].

All the previously cited research works accomplished a step towards a better understanding the time-domain behavior of metamaterials. Pendry et al. and Marques et al., through deriving the expression of the constitutive elements of SRR media and explicating the differential equations of wave propagation is such media laid the ground

for future research about time domain aspects [1][6][13][16]. Ziolkowski et al., based on Pendry's assumptions extensively investigated the propagation of waves in DNG media using finite time-difference techniques (FDTD) [19]. Semouchkina et al. studied resonance in metamaterials using FTDT to visualize standing-waves. [20]. Foteinopoulou et al. used the same technique to analyze a time wave as it hits a slab of a negative refractive index (NRI) [5]. Their work demonstrated that the wave front moves in the negative direction and confirms the existence of a backward wave. FDTD technique was used as well for the analysis of metamaterial based leaky wave antennas [21].

The transmission line model used by Caloz et al. has as well been used greatly in the analysis and modeling of metamaterial structures and double negative media [7][8]. Gómez-Díaz et al. in [22], presented a time-domain analysis of highly dispersive metamaterial waveguide and antenna structures in the impulse regime. They proposed a numerical method for the analysis of linear and non-linear metamaterial guiding structures using Transmission-Line Matrix (TLM) modeling. Grbic et al. used the TLM technique to perform a periodic analysis of a 2-D NRI transmission line[23]. So et al. used as well the time domain TLM technique to model metamaterials with NRI[24].

FDTD and TLM techniques were as well used together for a better modeling and analysis of metamaterial structures. In [25], Kokkinos et al. and Erickson et al. [26] modeled metamaterial structures using FDTD techniques with lumped element inclusions in their extended-FDTD approach to characterize numerically NRI materials. This method overcomes the shortcomings of TLM modeling which cannot consider certain parameters such as surface waves between the two media.

In 2015, Wynkoop analyzed different split-ring resonators and determined the factors that impact the resonance of the SRRs. In fact, by varying the dimensions of and between rings, he determined that the gap between the two rings in SRR is the most predominant factor in determining the capacitance of the SRR. This was followed by the design of waveguide filters based on SRR and waveguides to create band pass and band stop filters. Wynkoop simulated, measured and analyzed the temporal response of these structure using a time-gated sinusoid as an input. The analysis of the rise time of the output signal showed the presence of three linear slopes before reaching the maximum of the signal.

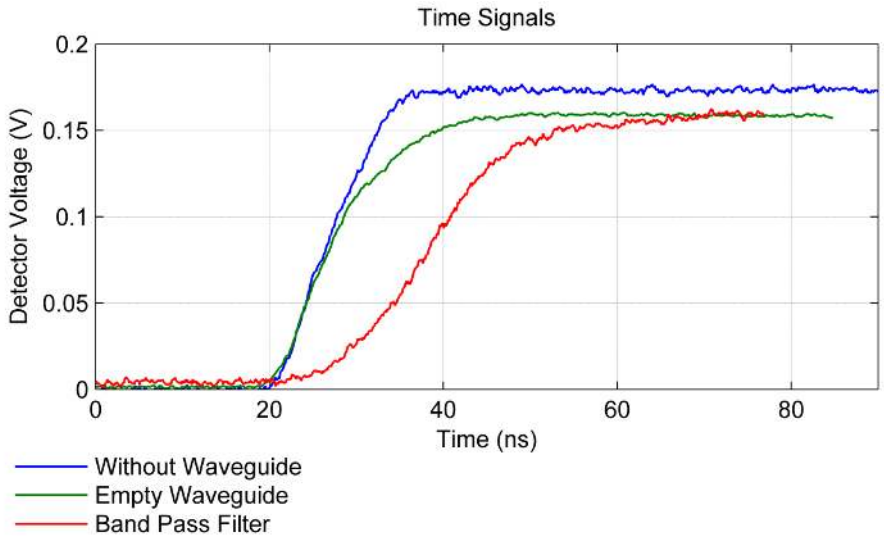

FIGURE 5: NORMALIZED TRANSMITTED SIGNALS OF VARIOUS CONFIGURATIONS [17]

Figure 5 depicts the normalized signals of three set-ups: the measurement bench without the waveguide structure, the bench with an empty waveguide and finally the bench with the passband filter structure. The figure shows that while the last linear slope is attributed to the waveguide (closeness between pass band system and empty waveguide close to saturation), the first two slopes are attributed to the SRR array. It

was as well shown that these slopes were inversely proportional to the exponential time constants of the phenomena. Furthermore, this research work confirmed the presence of a backward wave using time-domain field simulations.

1.1.2. Applications of Metamaterials

The interest in metamaterials was exhibited by the numerous applications that arose from the unusual properties of these structures. One of the direct applications of metamaterial is its ability to reduce the size of microwave structures [10]. From waveguide filters to high power devices, metamaterials can have an advantage in reducing the dimension of these structures by their capabilities of transmitting waves below cutoff. Metamaterials saw also an increasing interest from the high-power electromagnetics field, thanks to the compactness advantage but also to the periodicity of the structures and their dispersive behavior that can be used in backward wave oscillators among other structures. McGregor et al. [11] presented in 2013 a metamaterial-based traveling accelerating wave structure. Besides, metamaterials are used nowadays to design several types filters, transmission lines with controllable characteristics as well as for improving antennae radiated power and in optics to create perfect lenses. [12][13][8]

1.2. Review of Theory and Prior Results

1.2.1. Double negative media, the first assumptions

The assumptions of Veselago of negative permittivity and permeability were the first step in developing metamaterials. By simply taking Maxwell's equations [14]

$$\begin{cases} \nabla \times E = M - \dfrac{\partial B}{\partial t} \\ \nabla \times H = J - \dfrac{\partial D}{\partial t} \\ \nabla . D = \rho \\ \nabla . B = 0 \end{cases} \qquad \text{Eq.1.1}$$

For an isotropic medium such as free space, we have as well $D = \varepsilon E$ and $B = \mu H$

With:

- E: electric field intensity
- H: magnetic field intensity
- D: current flux density
- B: magnetic flux density
- J: electric current density
- M: magnetic current density
- ε: electric permittivity
- μ: magnetic permeability

For a monochromatic wave, Maxwell's equations reduce to [15]:

$$\begin{cases} \mathrm{k} \times E = \dfrac{\omega}{c} \mu H \\ \mathrm{k} \times H = -\dfrac{\omega}{c} \varepsilon E \end{cases} \qquad \text{Eq.1.2}$$

With k being the wavenumber and ω the angular frequency of the wave. We also know that the refraction index of the medium n can be written:

$$n^2 = \varepsilon \mu \qquad \text{Eq.1.3}$$

Inverting the signs of the permittivity and the permeability, Eq.1.2 becomes

$$\begin{cases} \mathrm{k} \times E = \dfrac{\omega}{c} (-\mu) H \\ \mathrm{k} \times H = \dfrac{\omega}{c} \varepsilon E \end{cases} \qquad \text{Eq.1.4}$$

From the previous equations the signs of $\mathrm{k} \times E$ and $\mathrm{k} \times H$ are inverted. The triad E, H, k changes from being right-handed to left-handed.

From Eq.1.3,

$$\sqrt{n} = \pm \varepsilon\mu \qquad \text{Eq.1.5}$$

The refraction index can be either positive or negative, and mathematically, both solutions are valid. However, several indications from previous experiments prove the existence of a negative backward wave and a negative refraction index [5]. It is important to note as well that the Poynting vector sign does not change. This indicates that the energy is still directed to the output port. The group velocity then, which is a representation of the energy, is positive.

1.2.2. Diamagnetic response of Double Negative Media

Pendry's motivation behind the design of the Split Ring Resonators was to create materials that would have tunable properties, and more specifically tunable magnetic permeability. His idea consisted in doping materials with small non-linear, resonant material which would greatly enhance the energy distribution in these locations and create properties specific to that material depending on its resonant state. This field enhancement would also reduce the power requirements for the material. Examples of these materials are wire media, and split ring resonators. A common magnetic material is composed of small magnetic dipoles that are randomly oriented. Under a magnetic excitation, these dipoles will tend to align in the direction of the applied field resulting in a magnetization vector M.

The presence of the magnetization increases the magnetic flux density which becomes

$$B = \mu_0 (H + M) \qquad \text{Eq.1.9}$$

μ_0 being the permeability of the free space. Since M is a quantity that depends on the external field, then

$$M = \chi_M H \qquad \text{Eq.1.6}$$

With χ_M being the unitless magnetic susceptibility, we have

$$B = \mu_0 (1 + \chi_M) H \qquad \text{Eq.1.7}$$

And since for an arbitrary medium $B = \mu H$, we can deduce that

$$\mu = \mu_0 (1 + \chi_M) = \mu_0 \mu_r \qquad \text{Eq.1.8}$$

If μ_r is negative, then the permeability of the medium is negative. This is achieved by Pendry's different media designs. The question is then, how to make μ_r negative or $\chi_M < 1$?

The answer to this question resides in the diamagnetic response of the cell. In fact, currents are induced in the cell when it is under the effect of an external time-varying magnetic field.

These currents themselves induce a magnetic flux that is opposite to the external applied field.

If this response is higher than the applied field itself, then we will have a total magnetic field in the opposite direction of the applied one and this would turn the triad E, H, k from right-handed to a left handed.

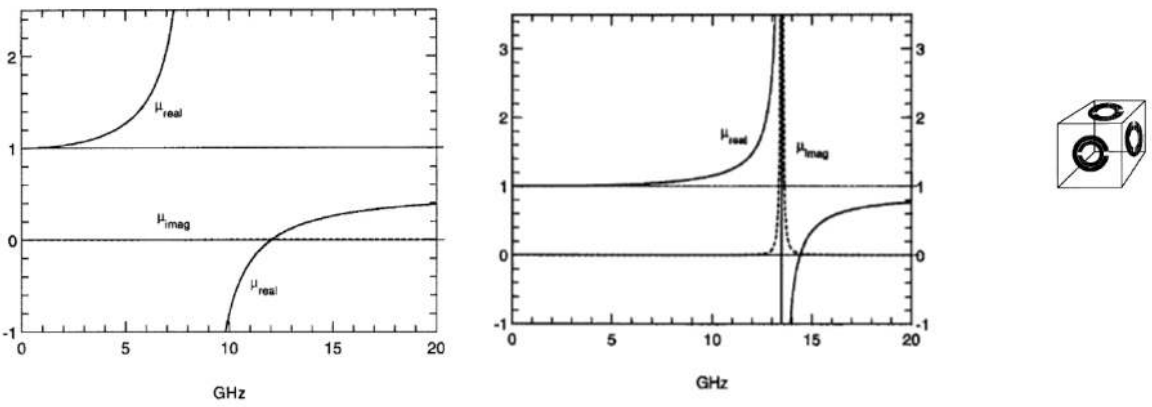

FIGURE 6: LEFT, DISPERSION WITH FREQUENCY OF PERMEABILITY FOR A SWISS ROLL STRUCTURE, CENTER: DISPERSION WITH FREQUENCY OF PERMEABILITY FOR A CUBIC SPLIT-RING STRUCTURE, RIGHT- CUBIC 3D SPLIT-RING STRUCTURE [1]

1.3. Split-Ring Resonator equations, characteristics and different designs

1.3.1. Split-ring resonator assumptions and equations

The split- Ring Resonator cell is constituted of two coupled conductive rings printed on a dielectric slab. Each of the rings have a cut that are opposite to each other. We should emphasize that the size of one cell should not exceed approximately one tenth of a wavelength at resonance to ensure that the external fields are spatially quasi-static.

For this analysis, an external electric field E oriented along $\hat{y}$, a magnetic field H oriented along $\hat{z}$ are considered. $\hat{x}$ is be the direction of propagation of the wave. The SRR is be placed such that the rings are in the (x, y) plane, perpendicular to the magnetic field direction. These considerations are extremely important since the following equations depend strongly on the direction of the magnetic and the electric field which explains the strong bianisotropy of the SRRs. With all the previous considerations, when an external field is applied, the SRR behaves as an LC resonator with the capacitance C being the sum of capacitances of both halves of the rings and

where the inductance is approximated to the inductance of a metallic ring having the average radius of the rings of the cell[13]. The resonance frequency of the cell is given by

$$\omega_0 = \sqrt{\frac{1}{LC}} \qquad \text{Eq.1.10}$$

With L and C respectively the inductance and capacitance of the entire cell.

The inductance C can be expressed as a function of the per unit length capacitance between the rings C_{pul} and the average radius $r_0$of the considered SRR such that

$$C = \pi r_0 C_{pul} \qquad \text{Eq.1.11}$$

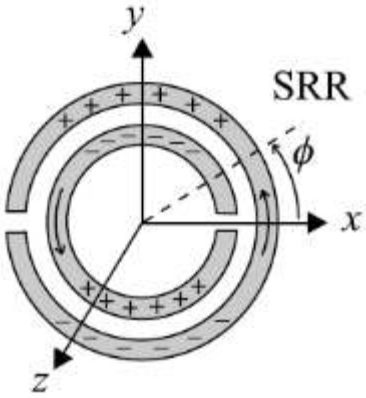

FIGURE 7: SKETCH OF THE EC-SRR WITH CHARGE DISTRIBUTION [13]

Due to the current distribution between the SRR rings [13], the cell behaves near resonance as the combination of one magnetic and two parallel electric dipoles.

The induced current in the rings creates a magnetic and electric polarization vector the depends on both external magnetic and electric fields such that

$$m_z = \alpha_{zz}^{mm} B_z - \alpha_{yz}^{em} E_y \qquad \text{Eq.1.12}$$

$$p_y = \alpha_{yy}^{ee} E_y + \alpha_{yz}^{em} B_z \qquad \text{Eq.1.13}$$

With

$$\alpha_{zz}^{mm} = \frac{\pi^2 {r_0}^4}{L} \left(\frac{{\omega_0}^2}{\omega^2} - 1\right)^{-1}, \qquad \text{Eq.1.14}$$

the magnetic polarizability induced from the external magnetic field,

$$\alpha_{yz}^{em} = -\alpha_{zy}^{me} = -2j\pi {r_0}^3 d_{eff} C_{pul} \frac{{\omega_0}^2}{\omega} \left(\frac{{\omega_0}^2}{\omega^2} - 1\right)^{-1} \quad \text{Eq.1.15}$$

the cross-polarizability derived from the Onsager theorem [16], ω being the frequency of the incident wave,

$$\alpha_{yy}^{ee} = \varepsilon_0 \frac{16}{3} {r_{ext}}^3 + 4{d_{eff}}^2 r^2 {C_{pul}}^2 L \frac{{\omega_0}^2}{\omega} \left(\frac{{\omega_0}^2}{\omega^2} - 1\right)^{-1} \quad \text{Eq.1.16}$$

r_{ext} being the outer diameter of the external ring. It is demonstrated as well that the Split-ring resonator exhibits a non-resonant polarizability [16] such that

$$p_x = \alpha_{xx}^{ee} E_y \quad \text{Eq.1.17}$$

With

$$\alpha_{xx}^{ee} = \varepsilon_0 \frac{16}{3} {r_{ext}}^3 \quad \text{Eq.1.18}$$

It is important to note that the model presented assumes that there are no losses. The introduction of losses changes the equations and ultimately losses cap the diamagnetic response of the cell or the structure. It will be assumed through all the thesis that the SRRs are loss free for the convenience of the calculations.

Going back to the expression of the total magnetic flux density, we have now

$$B_{tot} = \mu_0 (H_z + m_z) = \mu_0 H_z + \mu_0 \alpha_{zz}^{mm} H_z - j\alpha_{yz}^{em} E_y \quad \text{Eq.1.19}$$

The previous calculations shown are for a single SRR cell. We are considering the SRR cell as a unit cell in a homogenous medium. Therefore, and for the consistency of units,

We consider

$$\chi_M = {\mu_0 \alpha_{zz}^{mm}} \Big/ {(a \times b \times l)} \quad \text{Eq.1.20}$$

Where a, b and l are respectively, the height, width and length of the unit cell. Consequently

$$\mu = \mu_0 (1 + \chi_M) = \mu_0 \mu_r = \mu_0 (1 + {}^{\mu_0 \alpha_{zz}^{mm}}/_{a \times b \times l}) \qquad \text{Eq.1.21}$$

Thus, for a certain range of frequencies close to the resonance, μ is negative and negative permeability is achieved. This approach is the simplest for the computation of the constitutive susceptibility elements. This method also does not consider couplings between adjacent elements and each susceptibility is simply the corresponding polarizability, divided by the volume of the unit cell.

1.3.2. Split-Ring Resonator designs

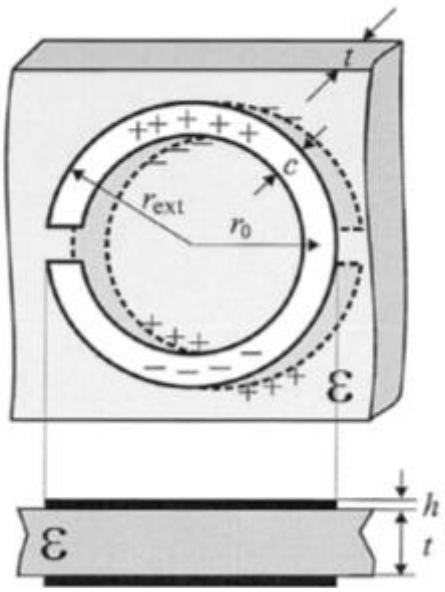

FIGURE 8: BROAD-SIDE COUPLED SRR

Several SRR designs arose from the original design. Broad-side coupled SRRs were built where the rings have the same size and are printed on each side of the dielectric slab. These rings' main advantage is to get rid of the cross polarizabilities in the expressions of the total fields. They are called broad-side coupled as opposed to the regular rings, which are referred to as "edge-side coupled" and where the rings are printed on the same side of the dielectric. The expressions of polarizabilities for the BC-SRRs are detailed by Marques in [13]. Several other designs were also presented, such as the non bianisotropic design where bianisotropy is avoided by linking the break of the outer ring to the inner ring

and vice versa. One of the other important designs is the isotropic SRR which is a cubic cell where each two parallel faces constitute a BC-SRR. This type of SRR does not depend on the direction of the fields and creates a 3D-negative permeability, while the conventional EC-SRR creates a negative permeability only in the direction perpendicular to the plane of the rings.

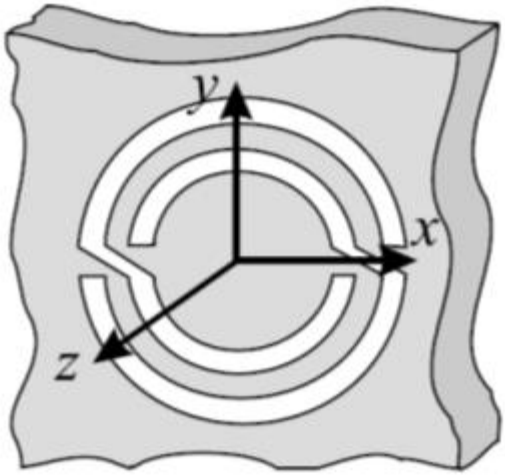

FIGURE 9: NON BIANISOTROPIC SPLIT RING RESONATOR [13]

1.3.3. Permeability of a Split-Ring Resonator

The next question to address, after detailing the theory behind negative permeability and explicating the EC-SRR model equations, is how to obtain a negative permittivity. Equation (Eq.1.19) highlights how, due to the bianisotropy, the external electric field has effect on the magnetization of the SRR cell. We now, derive analogous equations from the effect of the magnetic field on the electric polarization P (P is analogous to M).

A dielectric material is composed of negative and positive charges that are randomly distributed. Under the effect of an external electric field, these charges align in small electrical dipoles resulting in an electric polarization vector P such that

$$D = \varepsilon_0 E + P \qquad \text{Eq.1.22}$$

Where $P = \varepsilon_0 \chi_e E$, χ_e being the unit less electric susceptibility of the material

Ultimately, we will have

$$D = \varepsilon_0(1 + \chi_e)E = \varepsilon_0 \varepsilon_r E \qquad \text{Eq.1.23}$$

And

$$\varepsilon = \varepsilon_0 (1 + \chi_e) = \varepsilon_0 \varepsilon_r \qquad \text{Eq.1.24}$$

Combining equation (Eq 1.23) with the polarizability equation from (Eq 1.16), we obtain

$$D_{tot} = \varepsilon_0 \left(E_{yy} + p_y\right) = \varepsilon_0 E_y + \varepsilon_0 \alpha_{yy}^{ee} H_z - \alpha_{yz}^{em} E_y \qquad \text{Eq.1.25}$$

As we did for the magnetic susceptibility, we need to divide the polarizability by the volume of one cell and multiply it by the external medium permeability to conserve unit consistency.

Then

$$\chi_e = \frac{\alpha_{yy}^{ee}}{\varepsilon_0 (a \times b \times l)} \qquad \text{Eq.1.26}$$

And consequently

$$\varepsilon = \varepsilon_0 (1 + \chi_e) = \varepsilon_0 \varepsilon_r = \varepsilon_0 \left(1 + {\alpha_{yy}^{ee}}/{\varepsilon_0}\right) \qquad \text{Eq.1.27}$$

As opposed to the previous case, the polarizability α_{yy}^{ee} is negligible and will not be enough to make ε negative. It is noted as well that the non-resonant polarizability is not included in these equations since the external applied electric field involved in these equations is the field in the $\hat{y}$ direction. The easiest way to achieve a negative permittivity is putting the SRRs in a waveguide.

1.4. Split-Ring Resonator in Below Cutoff waveguides and Transmission Line Theory

1.4.1. SRRs in Waveguides Below Cutoff

Considering any hollow rectangular metallic waveguide, the wavenumber can be expressed as [14]

$$k^2 = \omega^2 \varepsilon_0 \mu_0 \left(1 - \frac{{\omega_c}^2}{\omega^2}\right) \quad \text{Eq.1.28}$$

Where ω_c is the cutoff frequency of the waveguide.

The similarity between this expression and the expression of an ideal plasma with the cutoff frequency being assimilated to the plasma frequency [13], we can consider the waveguide as a one-dimensional plasma with an effective permittivity

$$\varepsilon_{WG} = \varepsilon_0 (1 - \frac{{\omega_c}^2}{\omega^2}) \quad \text{Eq.1.29}$$

Now, if we consider a wave impingent on a waveguide below its cutoff frequency ω_c filled with SRRs with a resonant frequency ω_0 such that $\omega_0 < \omega < \omega_c$, then we have a propagation in the form of a backward wave in a left handed medium, where $\varepsilon < 0$ and $\mu < 0$.

For the small frequency range where we have $\mu < 0$, we will have a passband even though we are below the cutoff frequency of the waveguide. We have then a passband filter at a frequency very close to the resonant frequency of the SRR.

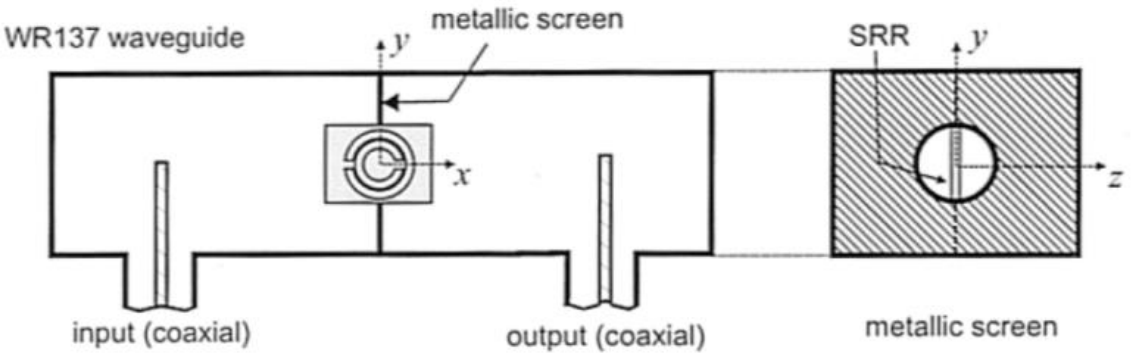

FIGURE 10: MARQUES' SCHEME OF THE EXPERIMENTAL SETUP FOR MEASURING THE SRRS MAGNETIC POLARIZABILITIES [16]

This system was experimentally demonstrated by Marques et al. and modeled by Hrabar et al.

We will consider in the rest of this manuscript that our system is composed of SRRs and a waveguide below cutoff fulfilling all the conditions for creating a DNG medium.

1.4.2. Left-Handed Transmission Lines (LHTL)

The transmission line theory is a very powerful theory and is widely used in Microwave and RF engineering. Since the conventional transmission line represents a right-handed medium (RHTL), Caloz et al. [7] imagined the analogous transmission line for left-handed media where the elements in series and parallel in a right-handed transmission line are interchanged. These transmission lines are called left-handed transmission lines (LHTL).

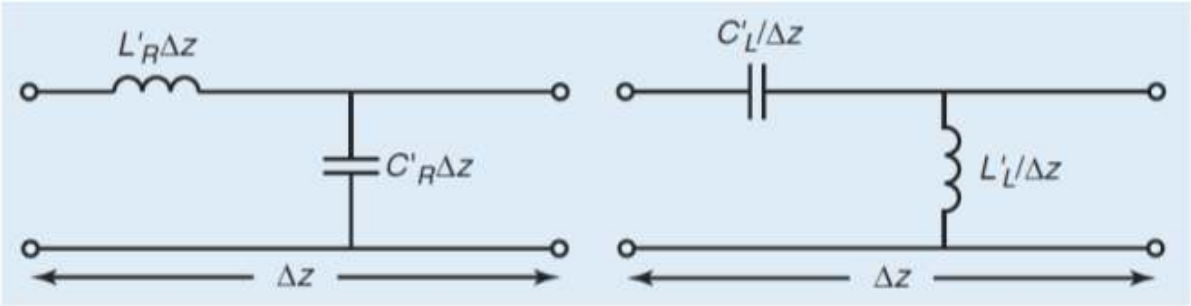

FIGURE 11: LEFT- RIGHT HANDED CONVENTIONAL TRANSMISSION LINE - RIGHT - LEFT HANDED TRANSMISSION LINE

The right sidee in figure 11 represents one cell of the transmission line. This cell is analogous to one cell of metamaterial and if the assumptions for the metamaterial cell size are conserved, the analogous TL model is valid. Looking at the distributed elements of the LHTL, it is evident that it is of high-pass nature in contrast to the conventional one. For the lossless LHTL, wavenumber calculated from the impedance is

$$\gamma(\omega) = \alpha + j\beta = \sqrt{ZY} = \sqrt{(j\omega C)^{-1}(j\omega L)^{-1}} = \sqrt{1/_{-\omega^2 LC}} \qquad \text{Eq.1.30}$$

For the lossless case, we have $\alpha = 0$ then

$$\beta = \pm\sqrt{1/_{\omega^2 LC}} \qquad \text{Eq.1.31}$$

On another hand, left-handed structures induce backward wave propagation where the phase velocity and the group velocity are antiparallel. Since the Poynting vector keeps the same direction, then the group velocity is positive, and the phase velocity is negative as we have a backward wave. This leads to the choice of the sign of β, which should be negative.

It is known from transmission line theory that the phase velocity is $v_p = \frac{\omega}{\beta} < 0$ and the group velocity is $v_g = \frac{\partial w}{\partial \beta} > 0$.

1.4.3. Composite Right Left-Handed Transmission Line (CRLHTL)

The Composite Right Left-Handed transmission line theory is an extension of the left-handed transmission line to a more realistic model. In fact, the LHTL model is purely theoretical because of the existence of parasitic elements that would introduce a right-handed behavior.

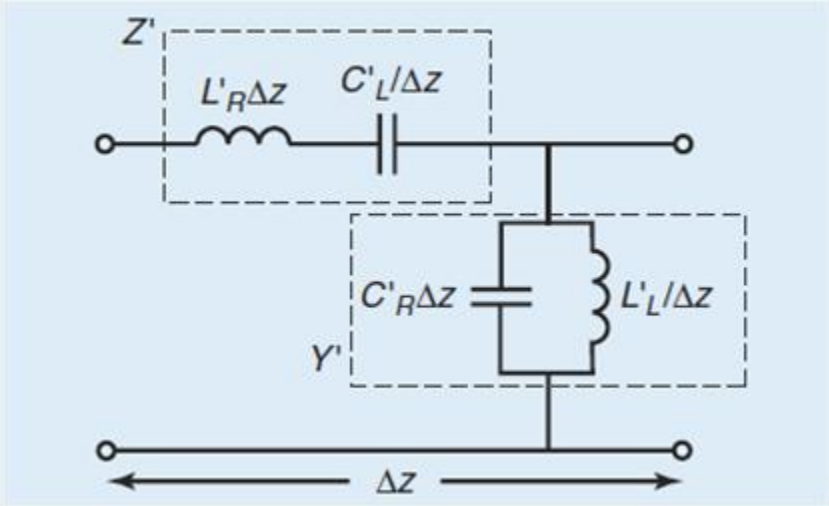

FIGURE 12: RIGHT LEFT-HANDED TRANSMISSION LINE MODEL[8]

The CRLHTL, as its name suggests, exhibits both behaviors, depending on the frequency.

FIGURE 13: DISPERSION DIAGRAM OF THE COMPOSITE RIGHT LEFT-HANDED TRANSMISSION LINE

In fact, considering the unit cell form the figure 12, the propagation constant is

$$\gamma(\omega) = \alpha + j\beta = \sqrt{Z'Y'} \qquad \text{Eq.1.32}$$

Where

$$Z' = j\omega L'_R - \frac{1}{j\omega C'_L} \qquad \text{Eq.1.33}$$

And

$$Y' = j\omega C'_R - \frac{1}{j\omega L'_L} \qquad \text{Eq.1.34}$$

are respectively the series impedance and the parallel admittance of the unit cell. Since it is assumed that the transmission line is lossless then $j\beta = \sqrt{Z'Y'}$. Depending on the value of β , the unit cell, will be either a band pass or a band stop filter. The mathematical solutions also for β can either be negative or positive, representing

respectively a left-handed or a right-handed behavior. In the dispersion diagram, the TL has antiparallel phase and group velocity for a certain frequency band. We notice also the presence of a stop-band and then another passband where the phase velocity and group velocity are parallel. The wavenumber β for this case has two solutions: a negative one when v_p and v_g are antiparallel [8].

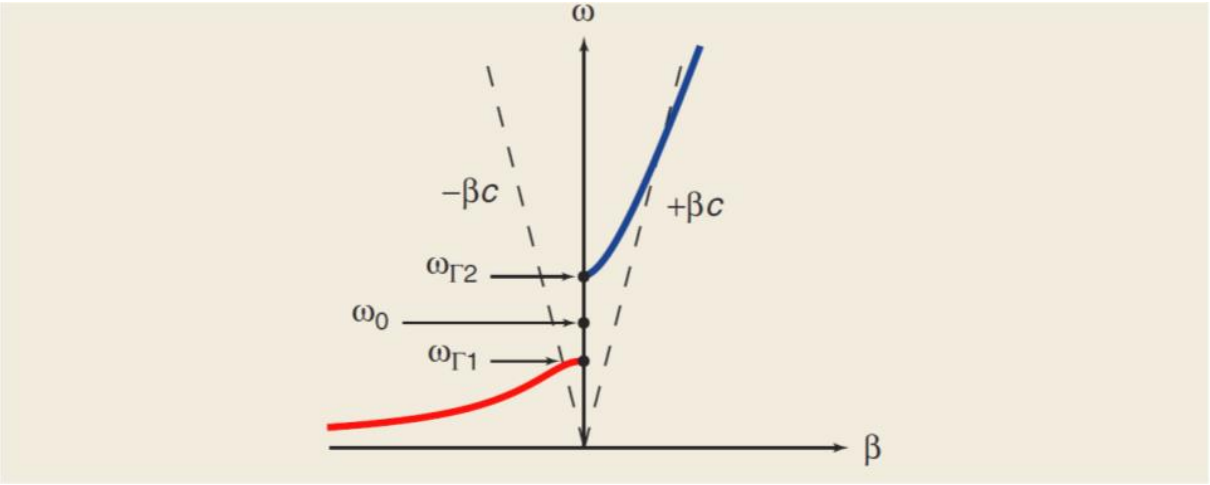

1.5. Motivation

The Applied Electromagnetics group of the University of New Mexico is interested in studying several aspects of using metamaterial in high and low power. The Plasma and Fusion Science Laboratory has already conducted some work in designing, simulating and measuring waveguide structures filled with SRRs to create band pass and band stop filters. The University of New Mexico Electromagnetics group, among others, have interest in the field where high-power devices using metamaterials are being studied and tested. The work conducted in the laboratory contributed as well in understanding frequency and time domain behavior of SRRs by designing, simulating and building SRRs and conducting experiments of SRR in a cut-off waveguide in frequency and time domains. The research work summarized in this thesis comes as an

extension of the previous work by developing a distributed linear model for this type of structure, comparing it to simulations and to measurements as well as by conducting other experiments that would support the previous research work accomplished with a particular focus on the time domain behavior.

1.6. Summary

This chapter summarizes the history and applications of metamaterial. Besides, it details the theory behind DNG media and the equations used to model SRR and metamaterial structures. These equations define the diamagnetic response in DNG media, and its effects on characteristics like the permeability, permittivity and the refraction index. This chapter also details equations for SRR resonance, which produce the polarizability parameters that define the permittivity and permeability of an SRR. Different SRR designs are briefly described to illustrate applications of the previous equations. The structure used in this research is composed of EC-SRRs in a waveguide below cutoff. There is limited knowledge of the behavioral characteristics of SRRs in waveguides.

The following chapter will describe a new model building on the CRLHTL model and the waveguide below cutoff equations. This new model attempts to understand and predict frequency and time domain behaviors of EC-SRRs.

2. Chapter 2: Linear Models

In this section, the linear models used to predict the SRR structure behavior are detailed. Before that, the structure used for simulations and measurements is briefly described. The results of the simulations and the experiment will be detailed later in the manuscript.

2.1. System Description

2.1.1. Simulated Structure

The simulations run for this project are numerous and varied. The first simulations are based on the initial design of the split-ring resonators [17]. Since the interest is focused mainly on the time domain behavior of the SRRs, simulations were run for a limited number of rings (maximum 3) as opposed to 3 SRR cards of 14 rings that were available in experiments.

The SRR cells, taken from [17] have the following dimensions:

- Outer ring large radius: 5 mm
- Outer ring small radius: 4.1 mm
- Ring width: 0.6mm
- Gap between rings: 0.3 mm
- Break in each ring: 0.5mm

The structure is composed of 3 waveguide sections which are the following:

- A WR-159 waveguide which has a cutoff frequency around 3.7 GHz when not loaded. The waveguide has inside dimensions of 1.59x.795 in or 4.039 x 2.019 cm. the waveguide section length varies depending on the number of cells. The length

is chosen to be equal to the SRR cell dimension (cubic cell). This means that if 1,2 or 3 SRR cells card are inserted in the waveguide, the WR-159 section will be respectively 1.2, 2.4, and 3.6 cm long. The reason for this is to avoid having attenuation caused by below cutoff empty waveguide portions.

- 2 sections of WR-284 waveguides attached to the ends of the WR-159 waveguide. These sections are 2.84 x 1.34 x 12 in or 7.214 x 3.404 x 30.5 cm (broad wall x narrow wall x length). The cutoff frequency of the 1st mode is 2.08 GHz

It is important to state that for all the simulations, the metal components are replaced by PEC and all the dielectric components are replaced by vacuum. This is to reduce the time of the lengthy simulations but also to enable us to increase in the number of mesh cells to get more precision for the time domain simulations.

2.1.2. Experimental Structure

The experimental structure is as well based on [17]. The SRR dimensions are identic to the SRR in simulations. The rings are printed on a rogers RT5880 which is a 0.017 mm copper cladding on a substrate with a relative permittivity $\varepsilon_r = 2.2$ with a thickness of 0.7874 mm. Low loss foam, "Eccostock PP-2" is used to maintain the SRR cards inside the waveguide. The foam has a dielectric constant $\varepsilon_r = 1.03$. The waveguide sections are as well made of copper. The dimensions of both WR-284 sections are identical to the ones in simulations. However, for the WR-159, the waveguide section used is 11.43 cm long. Two brass zero-length reducer flanges were also used that add 3.175 cm to the cutoff waveguide. To measure the signal at the end of the card in the waveguide, a slit is cut on the top of the middle section so that a small connector can be introduced in the waveguide.

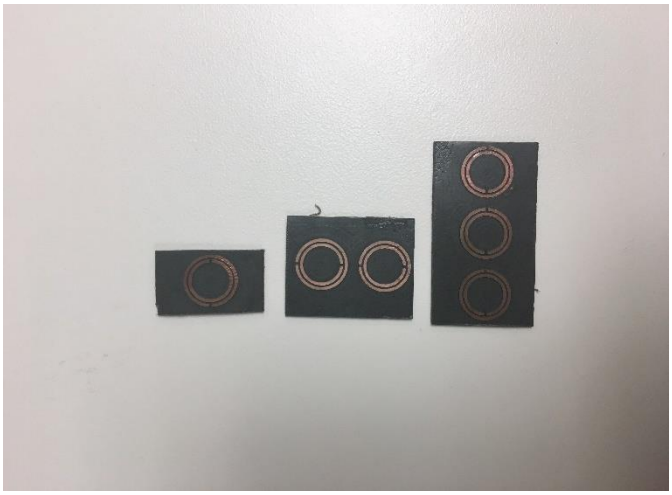

FIGURE 14: 1, 2 AND 3, CELL CARDS OF SPLIT-RING RESONATORS

The connector acts as a monopole antenna to capture the signal. The slit is approximately 0.16 cm wide and 9.5 cm long. Since the width is small compared to the waveguide, the losses from that slot should not be important. We note that, for the experimental set-up, the materials like copper, foam, dielectric, slit in the waveguide and all the parameters that are different from the simulation affect the response of the system, inducing a shift in the resonance but also creating losses which impact the time-domain response signals. However, the focus for this part will remain on the behavioral aspect of the response. The analysis is then more qualitative than quantitative. The description above depicts the system that measured and simulated and does not include all the components of the experimental set-up. The experimental measurement bench is detailed subsequently.

2.2. Composite Right-Left Handed Transmission Line Model

The composite right left-handed Transmission line model [8] constitutes the initial attempt to model the SRR structure described previously. The interest in constructing this model is to predict the metamaterial structure behavior in frequency

and time domain. The model will give insight on the interactions between the incident, reflected waves and the SRR cells inside the cutoff waveguide as well.

At first, the model considered is the model of Caloz et al. in [8]. Then, modifications are operated based on the results observed. As detailed in Chapter 1, the model is composed of a series and a parallel reactance. The series impedance is constituted of a capacitor C_l and an inductance L_r. Both elements are in series, as shows Figure 15. The elements with a subscript "r" account for the right-handed properties of the transmission line. These inductance and capacitance, which are also referred to as parasitic inductance and capacitance, are respectively due to unavoidable current flow along metallization and to the development of voltage gradients. Naturally, the elements with the subscript "l" account for the left-handedness of the line, which are generated by the metamaterial. It is important to note that the pure left-handed transmission line is a theoretical concept that does not exist in nature, due to those parasitic effects. Also, for simplicity, the transmission lines are assumed to be lossless for all the upcoming cases. In fact, while losses have an obvious role in controlling the behavior of the SRRs and their diamagnetic response [17], eliminating them will help greatly to simplify the equations in the analysis. Losses can always be added later in the model to approach the experimental case.

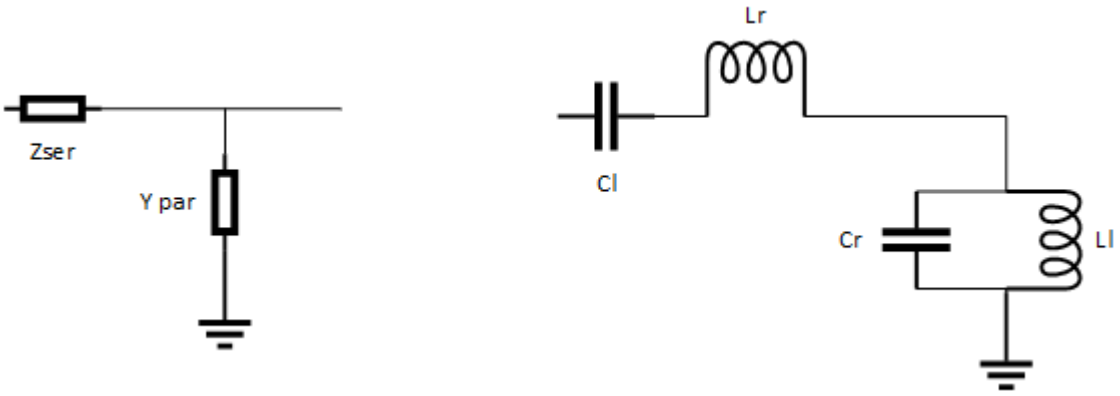

FIGURE 15: ONE UNIT CELL OF A CRLHTL

Since the SRRs are responsible for the left-handedness in the model, C_l and L_l are the reactive elements that constitute a split-ring resonator as theorized by Marques et al. [16]. The values of the left-handed elements will be taken from Marques' equations. Then $\omega_l = \frac{1}{\sqrt{L_l C_l}}$ is the angular velocity of resonance of the SRR. Since the two other elements represent the right-handed properties of the transmission line, they are chosen such that $\omega_r = \frac{1}{\sqrt{L_r C_r}} = \omega_c$, with ω_c being the cutoff frequency of the waveguide. All the elements in the unit cell in Figure 15 are per unit length and a unit length is equal to the SRR cell dimension.

It is important to state that a simple right-handed LC filter does not exactly correspond to a waveguide model. In fact, a right-handed LC filter is a lowpass filter while waveguides are known to be high pass filters. These values are considered in order to achieve the desired band pass filter that and that emulates the behavior of the whole system. Since it is known that the resonance frequency of the right-handed transmission line corresponds to the waveguide cut-off frequency, the value of at least one of the right-handed elements needs to be determined so that the other element's value can be calculated.

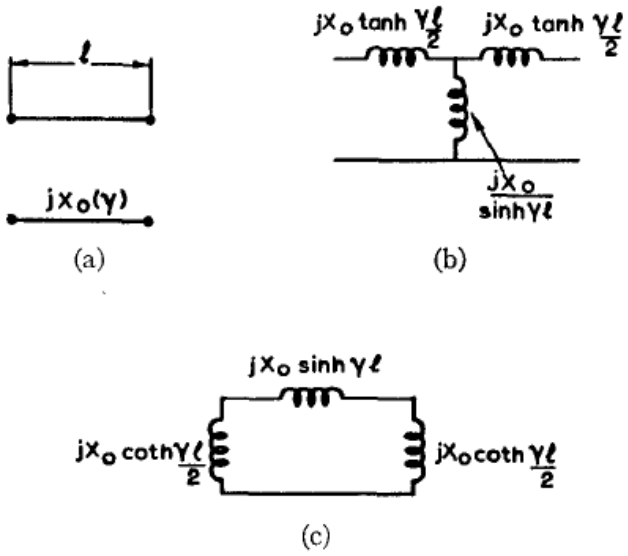

FIGURE 16: EQUIVALENT CIRCUIT OF EVANESCENT MODE WAVEGUIDE

While this work is based on error and trial, a reasonable and logical value of the right-handed elements is needed to start modeling. These values can be adjusted according to the obtained and desired results. In the early 1970's, Craven et al. developed a theory to create evanescent mode waveguide bandpass filters based on waveguides below cutoff. In [18], Craven et al. presented a lumped element approximation of a waveguide portion below cutoff. Hrabar et al. in [10], used a similar approximation for an SRR filled waveguide in his work. Figure 16 shows the equivalent model of a waveguide below cutoff. The elements of the model are a function of the propagation constant $\gamma = \frac{2\pi}{\lambda}\sqrt{\left(\frac{\lambda}{\lambda_c}\right)^2 - 1}$ and the variable X_0 where $X_0 = \frac{120\pi b}{a\sqrt{\left(\frac{\lambda}{\lambda_c}\right)^2 - 1}}$, λ being the free space wavelength, λ_c the cutoff wavelength, a the waveguide broad wall and b the waveguide narrow wall.

In the above model, the T-filter series impedance is

$$Z = jX_0 \tanh\left(\frac{\gamma l}{2}\right) = j \times \frac{120\pi b}{a\sqrt{\left(\frac{\lambda}{\lambda_c}\right)^2 - 1}} \times \tanh\left(\frac{\gamma l}{2}\right) \qquad \text{Eq.2.1}$$

Since the parasitic inductance is derived from the waveguide, L_r is considered as the double of the series inductance in Craven's T-filter model

$$L_r = 2 \times \frac{120\pi b}{a\sqrt{\left(\frac{\lambda}{\lambda_c}\right)^2 - 1}} \times \tanh\left(\frac{\gamma l}{2}\right) \times \frac{1}{\omega} \qquad \text{Eq.2.2}$$

If the wavelength is assumed to be at least 10x longer than the size of the unit cell, then γl is very small and thus, by expanding the term $\tanh\left(\frac{\gamma l}{2}\right)$ in a Taylor series, and considering only the first term of the series,

$$\tanh\left(\frac{\gamma l}{2}\right) \approx \frac{\gamma l}{2} \text{ and } L_r = \frac{120\pi b}{a\sqrt{\left(\frac{\lambda}{\lambda_c}\right)^2 - 1}} \times \gamma l \times \frac{\lambda}{2\pi C} \qquad \text{Eq.2.3}$$

By simplifying the inductance expression, the inductance value finally obtained is

$$L_r = \frac{60\pi l}{C} \qquad \text{Eq.2.4}$$

with C being the speed of light in free space. The right-handed inductance approximated value does not depend on the frequency and depends only on the dimensions of the cutoff waveguide. The value of C_r is, as mentioned previously, determined by the cutoff frequency where

$$C_r = \frac{1}{L_r \, {w_{co2}}^2} \qquad \text{Eq.2.5}$$

And the frequencies of interest are:

- $\omega_l = 21.425\ rad/ns$ corresponding to a frequency $f_0 = 3.41\ GHz$, frequency of the left-handed portion of the TL and resonance frequency of the SRR.
- $\omega_r = 23.311\ rad/ns$ corresponding to a frequency $f_c = 3.71\ GHz$, frequency of the right-handed portion of the TL and cutoff frequency of the waveguide. It is important to remember that the left-handed inductance was calculated directly from Marques' equations [13] and the dimensions of the SRR. The left-handed capacitance was derived from L_l and f_0 to ensure resonance at the desired frequency.

In the previous chapter, the diamagnetic response of the cells is generated by the negative permeability. It is as well crucial to notice the asymptotic behavior of μ, which is the key element in determining the elements of the model. In fact, μ and ε are approximated using the series and shunt elements of a single cell and thus, the series and parallel reactance elements will consequently be deduced. Two other key factors in determining the right composition of the model cell are the phase and group velocity that need to be antiparallel as shown in chapter 1. Looking back at equations Eq.1.33 and Eq.1.34, for the same cell:

$$\begin{cases} Z' = j\omega\mu = j\omega L_r + \dfrac{1}{j\omega C_l} \\ Y' = j\omega\varepsilon = j\omega C_r - \dfrac{1}{j\omega L_l} \end{cases} \quad \text{Eq.2.6}$$

Then

$$\begin{cases} \mu = L_r\left(1 - \dfrac{1}{\omega^2 L_r C_l}\right) = L_r\left(1 - \dfrac{{\omega_\mu}^2}{\omega^2}\right) \\ \varepsilon = C_r\left(1 - \dfrac{1}{\omega^2 L_l C_r}\right) = L_r\left(1 - \dfrac{{\omega_\varepsilon}^2}{\omega^2}\right) \end{cases} \quad \text{Eq.2.7}$$

where $\omega_\mu = \sqrt{\frac{1}{L_r C_l}}$ and $\omega_\varepsilon = \sqrt{\frac{1}{L_l C_r}}$.

Using [13] to calculate the left-handed elements and [18] for the right-handed elements, the graphs of permeability, permittivity and dispersion are drawn over a frequency sweep from 1 GHz to 6 GHz. The values of the elements are summarized in the table below:

Element	Value
L_r	7.539 nH

C_r	24.441 pF
L_l	16.8 nH
C_l	12.961 pF

2.3. Structure Modeled as a CRLHTL

2.3.1. Model à la Caloz

This model is the CRLHTL as described previously with the reactance values reported earlier. The focus in this part is in selecting the results (mu, ε, dispersion, line impedance) to evaluate the accuracy of the model.

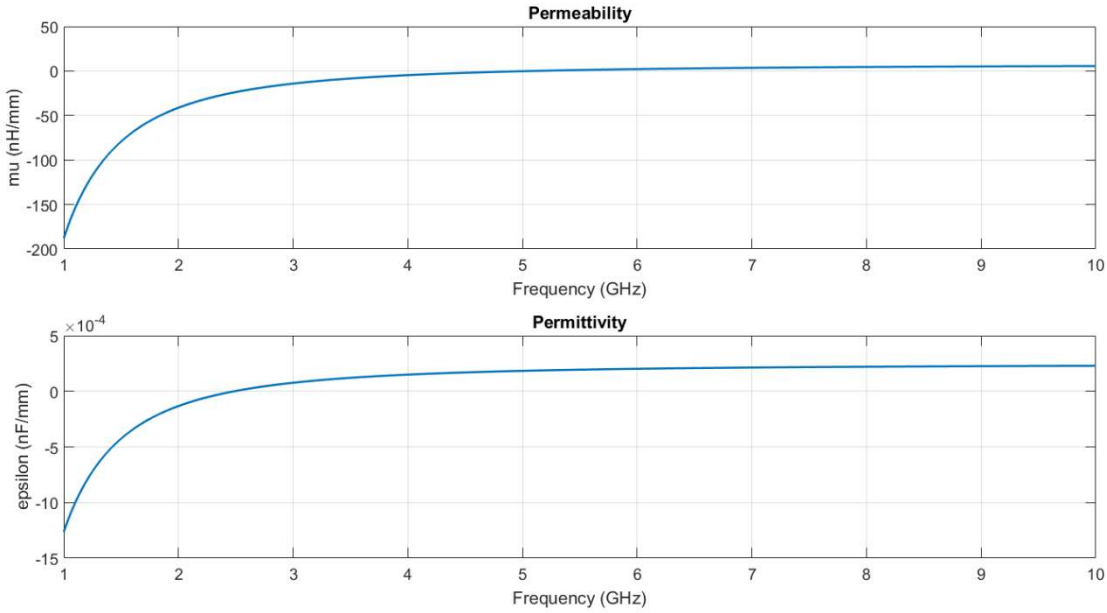

FIGURE 17: PERMITTIVITY AND PERMEABILITY OF A CRLHTL

Figure 17 shows that μ does not have an asymptotic behavior for this case and simply increases when ω increases. μ switches from negative to positive for a certain value of the frequency. The behavior of ε is similar as it increases from negative to positive. Both permittivity and permeability seem to reach a saturation or at least to have a very slow positive slope. Looking as well to the graphs of inverted μ and ε and to the

dispersion graph in Figure 19, the change of sign of μ and ε happens respectively at 5.091GHz and 2.48GHz. These values do not correspond to the target frequencies previously established. In fact, the medium parameters start to be negative at a frequency close to the resonance, which is expected to be 3.41 GHz. In the S-parameters graphs (Figure 18), the resonance is close to these values. This means that the model is close in terms of frequency behavior to the theory, but the element values are incorrect.

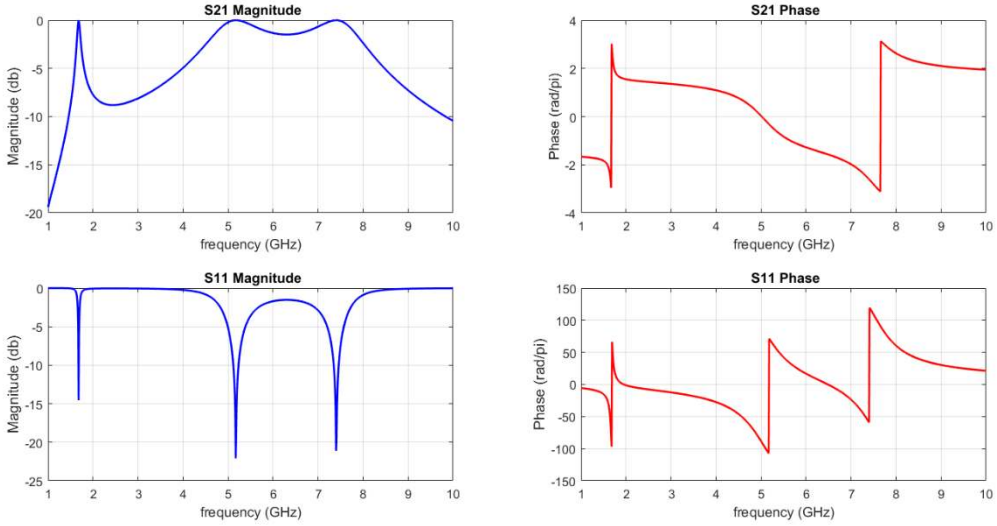

FIGURE 18: S-PARAMETERS OF CRLHTL

Two interesting phenomena are, however, observed: the stop band that is visible between those frequencies and the antiparallel group and phase velocity in the frequency range below 2.48GHz. Nevertheless, the behavior of the medium parameters does not correspond to Marques' theory behavior. In the previous chapter, it was determined that the transmitted wave is a result of a negative permeability and permittivity. The negative permeability is obtained from the magnetic polarizability of the SRR (Eq1.14) and by assuming that the waveguide below cutoff is a one-dimensional plasma with a plasma frequency equal to the cutoff of the waveguide (Eq.1.29).

$$\begin{cases} \varepsilon = \varepsilon_{eff} \propto (1 - \frac{{\omega_c}^2}{\omega^2}) \\ \mu = \mu_{eff} \propto (\frac{{\omega_0}^2}{\omega^2} - 1)^{-1} \end{cases} \quad \text{Eq.2.8}$$

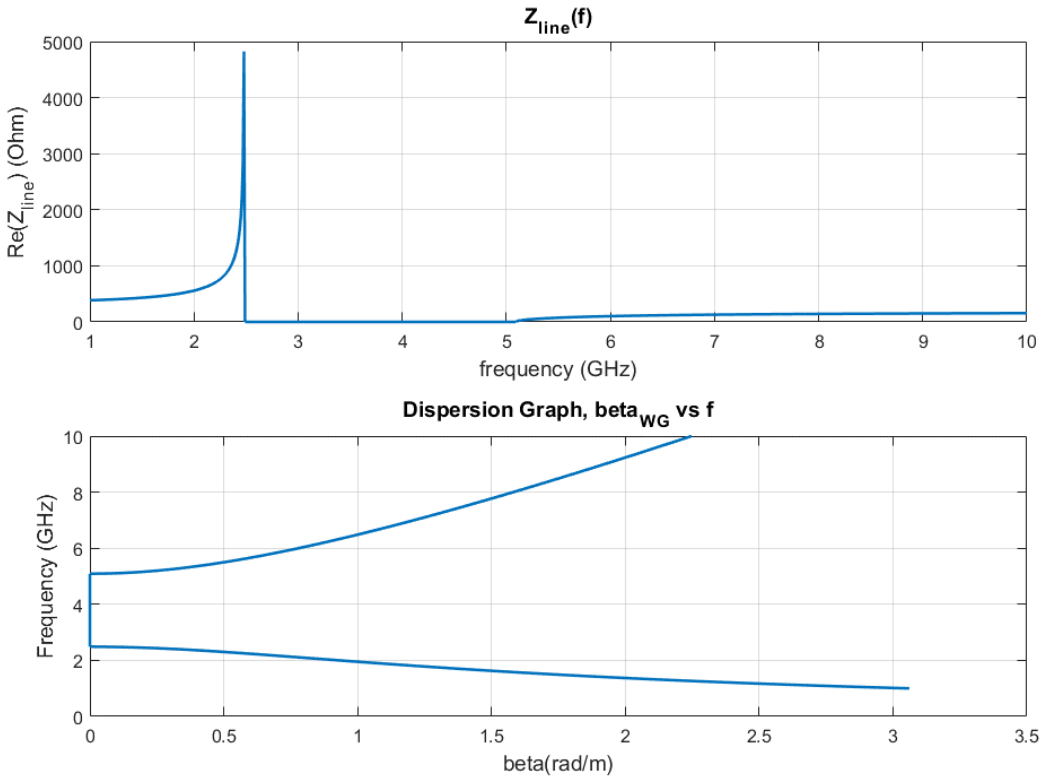

FIGURE 19: CRLHTL CHARACTERISTICS (LINE IMPEDANCE, DISPERSION)

- **Modified Model**

To create an asymptotic behavior, the zero of the S21 function needs to be changed to a pole. This can simply be done by putting the elements of Z' in parallel instead of in series. This gives:

$$Z' = j\omega\mu = \frac{1}{j\omega L_r + \frac{1}{j\omega C_l}} = \frac{1}{j\omega L_r \left(1 - \frac{1}{\omega^2 L_r C_l}\right)} \quad \text{Eq.2.9}$$

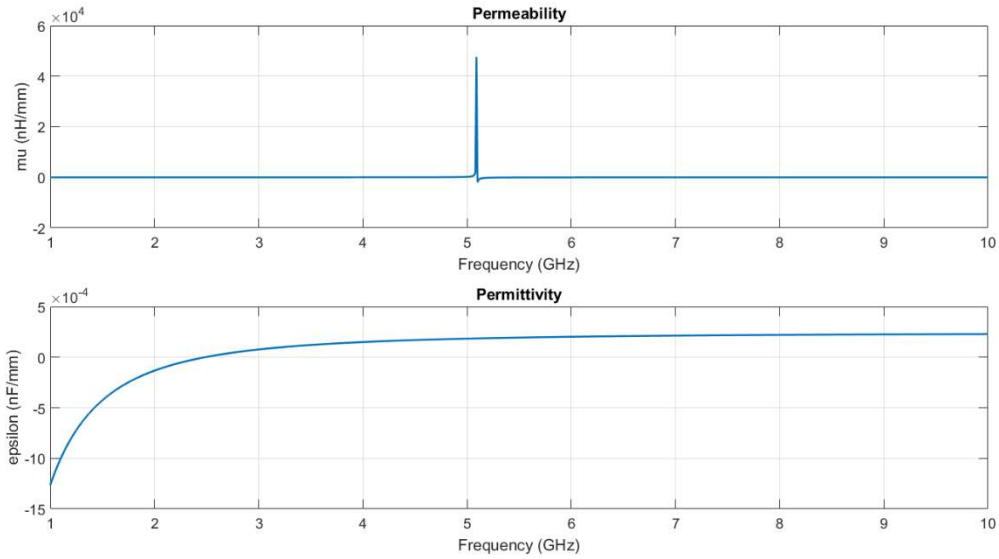

FIGURE 20: PERMEABILITY AND PERMITTIVITY OF THE MODIFIED MODEL

When putting the reactances of the series element of the T-filter in parallel, μ acquires an asymptotic behavior as predicted. ε is not modified in this model. When compared to the initial model, the inversion of the passband and the stop band is observed in the line impedance graph. Also, the group and phase velocity are both positive between 2.48 GHz and 5.091 GHz. This alongside the permittivity graph (figure 3-6) indicates that this model is not correct. In fact, a negative medium should be obtained for frequencies that are close to the resonance which corresponds here to 2.48 GHz. While this model shows behaviors of ε and μ close to the theoretical expressions, it is important to note that

$$f_\varepsilon = 2.48\ GHz\ < f_\mu = 5.091\ GHz$$

For a waveguide below cutoff filled with metamaterial, the transmitted wave is a result of negative μ and ε. However, for this case, ε switches from negative to positive while μ is positive and therefore this does not correspond to our model. Looking at f_ε , it is derived from the elements of Y'. The right-handed element can be modified to obtain a more realistic value for f_ε, which should be close to the waveguide cutoff frequency.

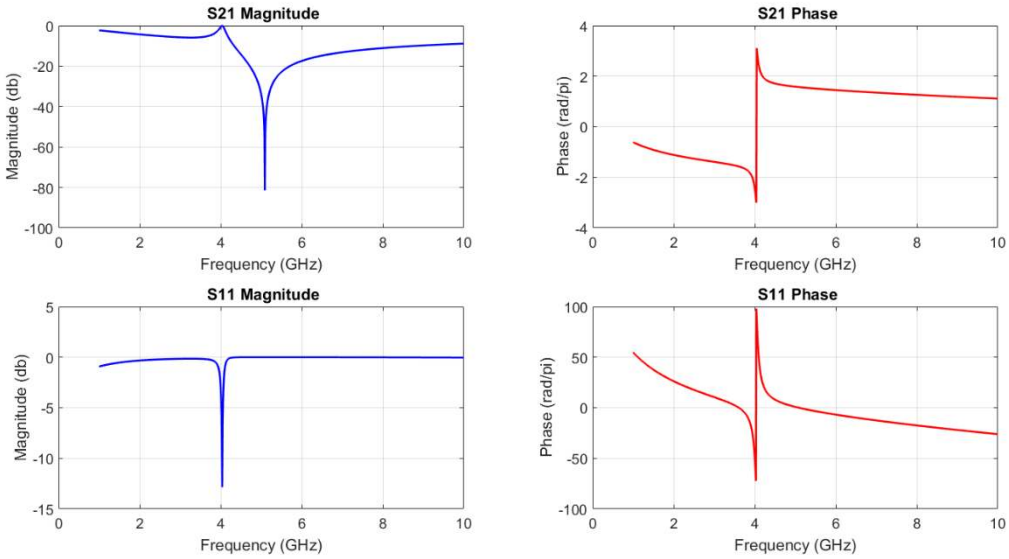

FIGURE 21: S-PARAMETERS OF THE MODIFIED MODEL

The S-parameter figure confirms it as a dip in S21 exists at 5.091 GHz corresponding to the asymptotic behavior of μ. The presence of a peak is noted as well in S12 at around 4GHz. While determine the origin of this peak could not be clearly determined, it is more likely that it is due to of the characteristic impedance. If input impedance, that is chosen to be 50 Ohms, is varied, the peak shifts which indicates that it does not correspond to resonance.

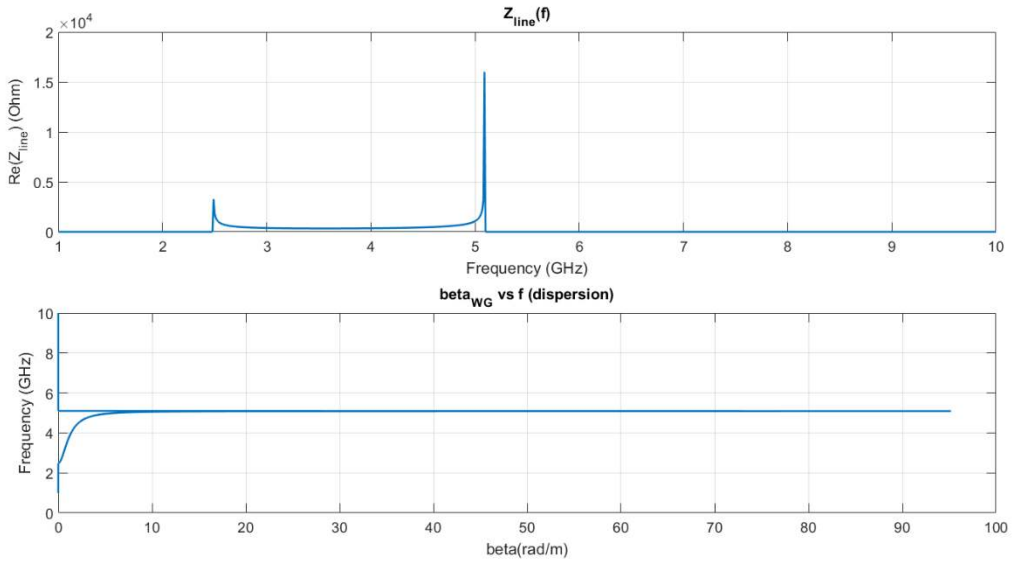

FIGURE 22: LINE CHARACTERISTICS OF THE MODIFIED MODEL

It is important to remember that the values of the inductances in the model are chosen first, and the values of the capacitances are derived from these values and the interest frequencies. Modifying the right-handed element in Y will impact f_μ as well which itself should be close to the resonance frequency of the SRR. Since $\omega_\mu = \frac{1}{\sqrt{L_r C_l}}$ and $\omega_\varepsilon = \frac{1}{\sqrt{L_l C_r}}$, then by simply choosing $L_r = L_l$, $\omega_\mu = \omega_0$ and $\omega_\varepsilon = \omega_c$ are obtained. From Figure 23, μ has an asymptotic behavior at 3.41 GHz and switches from positive to negative at that frequency and ε increases from negative to positive and changes sign at 3.71 GHz.

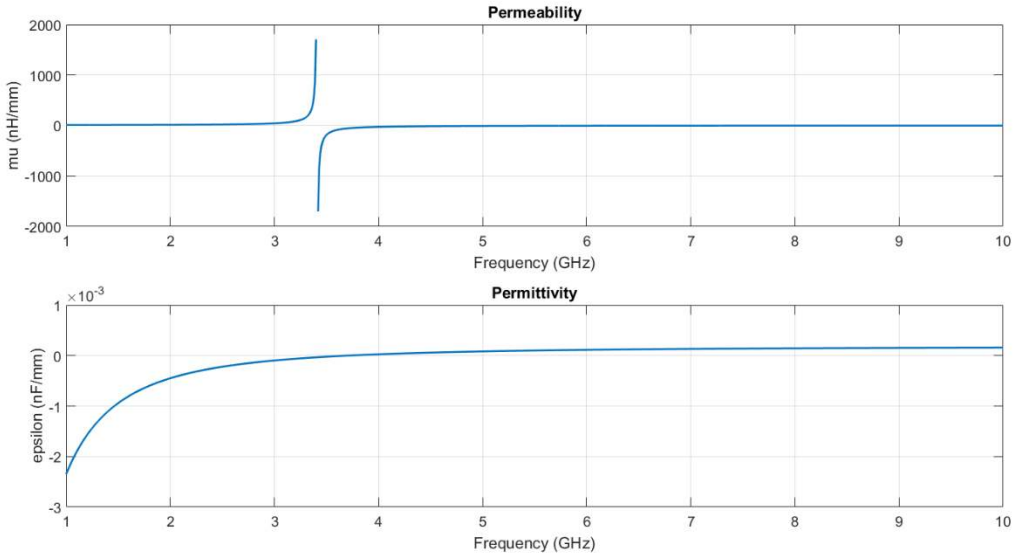

FIGURE 23: ADJUSTED PERMITTIVITY AND PERMEABILITY FOR THE MODIFIED MODEL

From characteristics of the transmission line, the line impedance is non null only between the frequencies of interest and is infinite at those frequencies. Antiparallel group and phase velocity in that same frequency band are as well observed for the same bandwidth. Furthermore, From the S-parameter graphs , a dip is noted in S21 with a negative infinite value at 3.41 GHz. This dip corresponds to the asymptotic behavior of the permeabilty at this frequency. Besides that, a peak exists at around 3.5 GHz that does not change when changing the input impedance and is then most likely to be due

to resonance. For frequencies above the frequency of that peak, the magnitude of the S21 drops by a certain amount and there is no second peak that would correspond to the medium switching to positive pemeability and positive permittivity.

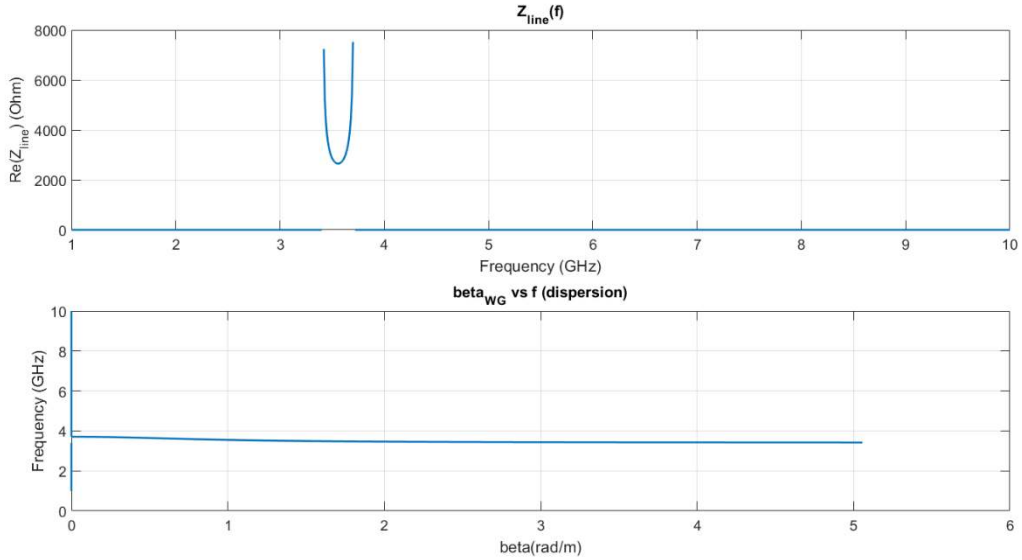

FIGURE 24: MODIFIED CRLHTL LINE IMPEDANCE AND DISPERSION

While the permittivity crosses the x-axis at 3.71 GHZ and becomes positive, the permeability stays negative while approaching asymptotically the x-axis and remaining negative. This is the reason why the real part of the line imedance is zero above that frequency, and while S12 shows an increase in transmission, that is corresponding to the increase of μ, there peak at that frequency which will indicate the the permability as reached a positive value again. This is considered as a major limitation in this model as it has to have right-handed properties for frequencies above the cutoff. Moreover, Eq 1.21 states that

$$\mu = \mu_0\left(1 + {\mu_0\alpha_{zz}^{mm}}/{a \times b \times l}\right) \qquad \text{Eq.1.21}$$

The presence of a constant which is not considered in the model is noted. This constant shifts the value of the permittivity across all frequencies. However, at the resonance, the absolute value of μ is also very high, and the constant can be neglected at this

particular frequency. An explanation for this discrepancy between the model and Marques' equations is that the model considers only the part of the permeability that is frequency dependent. This part of the permeability is generated by the interaction between the incident wave and the SRRs. For consistency purposes, it is assumed that the model is valid only at the resonance frequency where μ and ε are sufficiently negative to produce a peak in S21 and then would constitute the band pass filter.

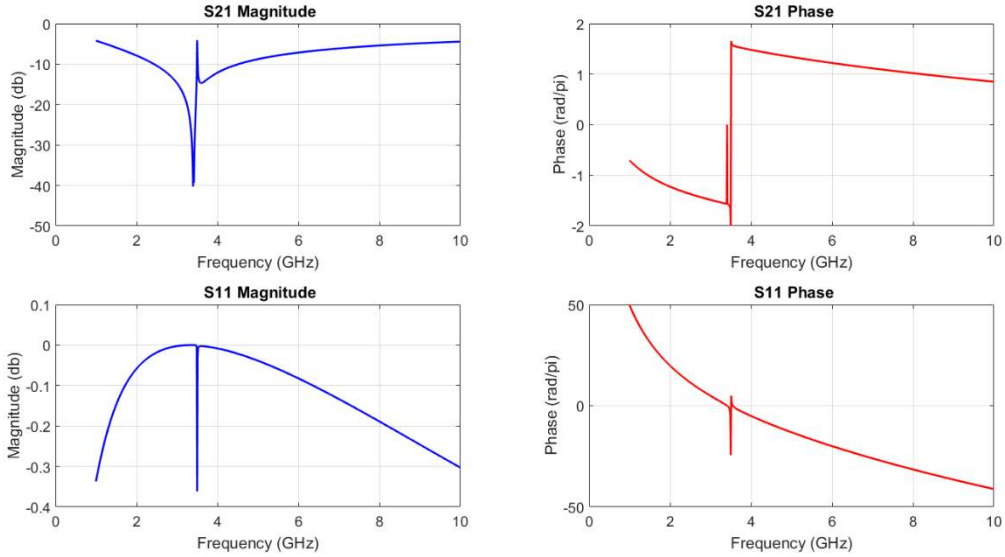

FIGURE 25: S-PARAMETERS OF ADJUSTED CRLHTL

A major drawback in this model is that lacks to include all the parameters that play a role in controlling the permeability. While the lossless case is treated, which means that there are no resistive values included in the equations, it is essential to note the existence of a constant in the equation of the permittivity. This constant comes from the medium of the waveguide and could as well be interpreted as a resistance coming from the medium characteristics or a combination of some or all the reactive elements in a fashion that would not be frequency dependent. It is also important to state that, to have a resonant behavior at the desired frequency, the asymptote in μ requires to be shifted and thus the reactance values to be corrected. The shift should correspond to the

effect of the characteristic permeability of the free space in this case. The frequency domain behavior however is considered consistent for the assumption made earlier, even though it is expected that this constant would play a role in the time-domain behavior. Additionally, shifting the values at which ε and μ are zero and infinite from the resonance frequency should be considered so that resonance happens exactly at the desired frequency.

2.3.2. Model Characteristics

Analysis of one cell

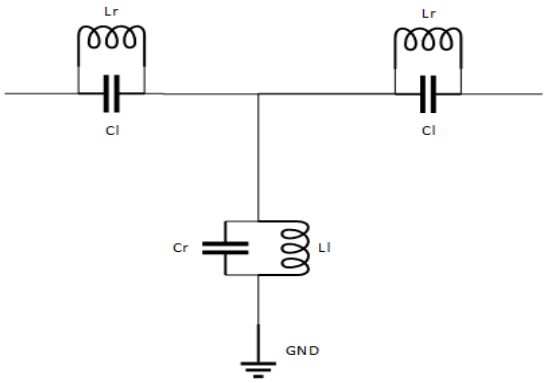

FIGURE 26: LUMPED ELEMENT MODIFIED CRLHTL MODEL

Since the latter model is closer to theory, it is considered in the following analysis to prove that it has the characteristics of a double negative media in the region of interest. Looking at the model of a CRLHTL represented in Figure 26, the expressions of the line characteristics can be easily derived,

$$Z_{ser} = \frac{1}{j\omega L_r + \frac{1}{j\omega C_l}}$$

$$Y_{par} = j\omega C_r + \frac{1}{j\omega L_l}$$

Knowing that,

$$\gamma = \sqrt{Z_{ser}Y_{par}}$$

$$\gamma = \sqrt{\frac{j\omega C_r + \frac{1}{j\omega L_l}}{j\omega L_r + \frac{1}{j\omega C_l}}} = \sqrt{f(\omega)}$$

If $f(\omega) > 0$ then γ is Real and is a pure loss. However if, $f(\omega) < 0$ then, γ is purely imaginary and $\gamma = j\beta$ with $\beta = \pm\sqrt{-f(\omega)}$.

Since β is the wavenumber, propagation exists only when $f(\omega) < 0$.

$$\beta = k\left(\frac{\omega^4 L_r C_r L_l C_l + 1 - \omega^2 C_l L_r - \omega^2 L_l C_r}{-\omega^2 L_l C_l}\right)^{\frac{1}{2}}$$

With $k = \pm 1$

The resonance frequency is a pole for β. This can be seen through the asymptotic behavior in the dispersion figure (Figure). The value of beta decreases from infinity and reaches zero at the frequency f_ε. Also, For frequencies below f_μ and above f_ε, beta is zero. From its numerator, the wavenumber has four zeros. These solutions correspond to the angular speeds $\omega = \pm\sqrt{\frac{1}{L_r C_l}}$, $\omega = \pm\sqrt{\frac{1}{L_l C_r}}$.

For a positive k, β $\omega < \min(\sqrt{\frac{1}{L_r C_l}}, \sqrt{\frac{1}{L_l C_r}})$ and $\omega > \max(\sqrt{\frac{1}{L_r C_l}}, \sqrt{\frac{1}{L_l C_r}})$

	$\omega < \min(\sqrt{\frac{1}{L_r C_l}}, \sqrt{\frac{1}{L_l C_r}})$	$\min(\sqrt{\frac{1}{L_r C_l}}, \sqrt{\frac{1}{L_l C_r}}) < \omega < \max(\sqrt{\frac{1}{L_r C_l}}, \sqrt{\frac{1}{L_l C_r}})$	$\omega > \max(\sqrt{\frac{1}{L_r C_l}}, \sqrt{\frac{1}{L_l C_r}})$
Sign of f	negative	positive	negative
β	Real and positive	imaginary	Real and positive
γ	$j\beta$	α	$j\beta$

For a negative k,

	$\omega < \min(\sqrt{\frac{1}{L_r C_l}}, \sqrt{\frac{1}{L_l C_r}})$	$\min(\sqrt{\frac{1}{L_r C_l}}, \sqrt{\frac{1}{L_l C_r}}) < \omega < \max(\sqrt{\frac{1}{L_r C_l}}, \sqrt{\frac{1}{L_l C_r}})$	$\omega > \max(\sqrt{\frac{1}{L_r C_l}}, \sqrt{\frac{1}{L_l C_r}})$
Sign(f)	positive	negative	positive
β	imaginary	Real and negative	imaginary
$\gamma =$	α	$j\beta$	α

It can easily be noted that for the model's case k is negative and β is a real negative number for the passband between f_μ f_ε. However, in the figures, β is positive. This is caused by Matlab that only computes the positive solution. The dispersion graph however confirms the latter results. In fact the phase velocity is $v_p = \frac{\omega}{\beta}$ and should have the same sign as the wavenumber. Looking at the group velcotity $v_g = \frac{\partial \omega}{\partial \beta}$. Depending on the expression of β, antiparallel group and phase velocity can exist. This is the case in the dispersion graph in Figure 24 where group velocity is negative and phase velocity is positive. However, through previous experiments that were conducted and that are reported in theory [6,9,10,16,17], an output power coming out of the metamaterial strucutres existsand therefore the group velocity cannot be negative. This leads to the conclusion that the phase velocity is negative and that the solution for β for the left-handed behavior is the negative solution. This is also backed by simulations done previously that show a backward wave traveling throughthe structure while having an output power at the same time. It is important to observe as well, from [8], that the left-handed behavior is expressed in Figure 2-9 for a negative β. All these support the idea that this model is correct from the standpoint that it creates a left-handed behavior

for a short passband that is below cutoff . All the characteristics of a double negative medium are then retereived. It is important to remind that this model is only valid at the resonance frequency as there is no right-handed behavior seen above the cutoff in the dispersion graph. This is due to the fact that μ remains negative after the resonance and ε becomes positive after the cutoff which leads to a stopband.

Extension to multiple cells

The model previously described is extended by cascading 3 cells together. The multiplication of the cells follows also the assumptions made in [8]. From Figure 27, the diamagnetic response is higher. In fact, for μ , the slope for 3 cells is higher . Its absolute value increases when it gets closer to the asymptote. It is noted as well that the absolute value of ε is higher for the whole frequency range. This suggests that there is an effect of the number of cells on the value of the permittivity. While the influence on ε exists [16], especially manifestating through the effect of the electric-electric polarizabilty and the magneto-electric polarizability, its presence over the whole frequency sweep is less likely. This behavior is more local to the resonance frequency region.

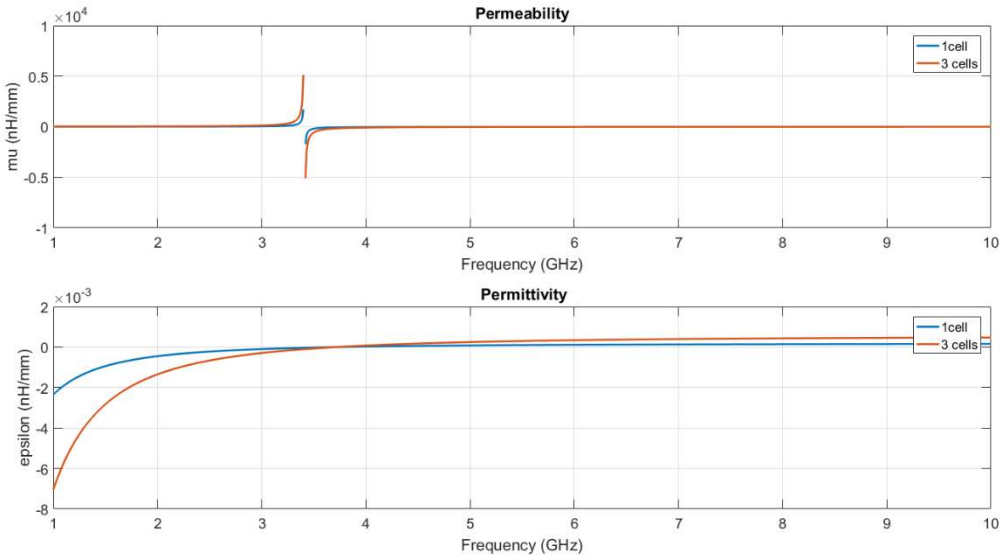

FIGURE 27: PERMITTIVITY AND PERMEABILITY OF 1 AND 3 CELL STRUCTURES

For the line characteristics (Figure 28), while the left-handed behavior is maintained for the same bandwidth, the phase velocity increases while the group velocity decreases. This means that the backward wave created in the structure travels faster while the transmitted power through the output port takes more time to travel to the port. This suggests that increases the number of cells induces a higher diamagnetic response and thus, creates a faster backward wave. The coupling between cells contributes then into maintaining and reinforcing this backward wave. It is important to note however that this claim is valid only for the direction of propagation of the wave. In fact, the permittivity and permeability are tensors depending on x, y and z directions. However, in the previous model, they are simplified to unidimensional equations and are valid only for the direction of propagation. It is considered as well that the TL model is uniaxial as the extension to multiple cells is done only in the direction of propagation. Since the SRRs are anisotropic, the medium parameters are not expected to be the same as the aforementioned findings in all the directions.

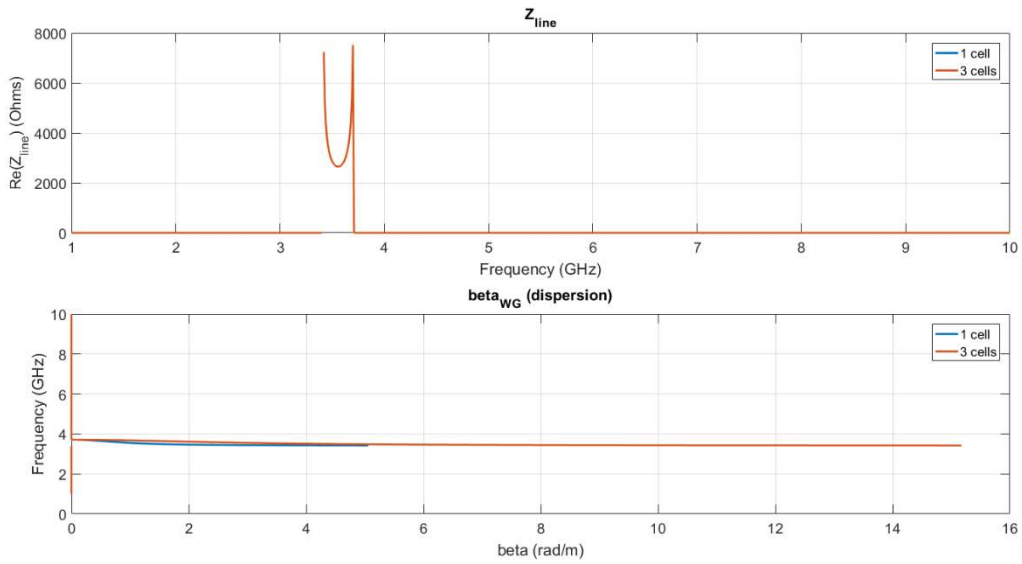

FIGURE 28: MODIFIED TL CHARACTERISTICS

It is important to observe that the characteristic impedance of the line did not change.

Since

$$Z_{line} = \sqrt{\frac{Z_{nser}}{Y_{npar}}}$$

With Z_{nser} and Y_{npar} respectively the series impedance and the parallel admittance of the mulitple cell TL and Z_{line} the characteristic impedance of the TL. And for multiple cells [8],

$$Z_{nser} = n \times Z_{ser}$$

$$Y_{npar} = n \times Y_{par}$$

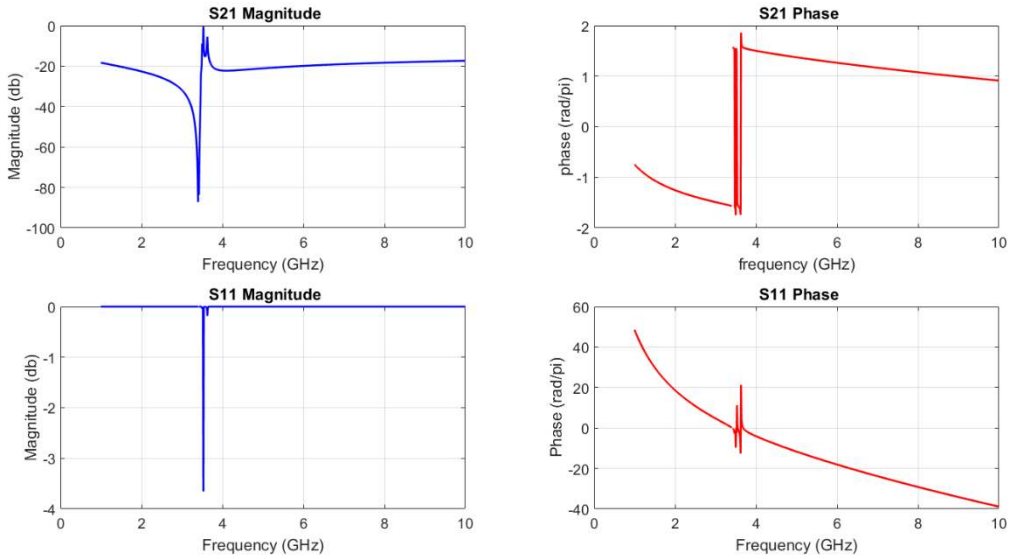

FIGURE 29: S-PARAMETERS OF MODIFIED AND ADJUSTED MODEL

The characteristic impedance of the line does not change with the number of the cells. From Figure 29, an expansion in the bandwidth is observed as well as the presence of multiple peaks in S21 around the resonance. However, the dip in S21 does not change with the number of cells. This is expected as the asymptotic behavior in μ is still present at the same frequency. The assumption that the model is only available for the resonance frequency is still maintained. This model can be extended to a higher number of cells where the same phenomena are observed for 3 cells. This means that the number of cells increases the diamagnetic response of the signal and increases the bandwidth of the passband.

2.3.3. Model with Marques' Approach

Single Cell Model

While the previous model exhibits left-handed behavior and shows that it can approach a waveguide below cutoff behavior to some extents, it remains a mere approximation of the structure as it does not show properly the passage from left handed

to right handed behavior. In this final model that constructed, the equations are based on Marques' approach [16] of SRR sand adapted it to the structure. Recalling the permeability expression (Eq.1.21)

$$\mu = \mu_0 (1 + \chi_M) = \mu_0 \mu_r = \mu_0 (1 + {}^{\mu_0 \alpha_{zz}^{mm}}/_{a \times b \times l})$$

Where (Eq.1.14)

$$\alpha^{mm} = \frac{\pi^2 {r_0}^4}{L} (\frac{{\omega_0}^2}{\omega^2} - 1)^{-1}$$

The direction of the polarizability is omitted since a unidimensional case is considered. L is the inductance of the SRR, r_0 is the mean radius of the SRR and $\omega_0$is the resonance frequency of the SRR. From [13],

$$L = \mu_0 r [\ln\left(\frac{16r}{d}\right) - 2] \qquad \text{Eq.2.10}$$

where d is the gap distance between the two rings. ω_0 is a pole of μ and therefore, μ has an asymptote for the value of ω_0. For the permittivity from (Eq.1.27)

$$\varepsilon = \varepsilon_0 (1 + \chi_e) = \varepsilon_0 \varepsilon_r = \varepsilon_0 \left(1 + {}^{\alpha_{yy}^{ee}}/_{\varepsilon_0}\right)$$

With (Eq.1.16)

$$\alpha_{yy}^{ee} = \varepsilon_0 \frac{16}{3} {r_{ext}}^3 + 4 {d_{eff}}^2 r^2 {C_{pul}}^2 L \frac{{\omega_0}^2}{\omega} \left(\frac{{\omega_0}^2}{\omega^2} - 1\right)^{-1}$$

These expressions are for a SRR in vacuum. Since the cells are in a cutoff waveguide where the permittivity is approximated to (Eq.1.29)

$$\varepsilon_{WG} = \varepsilon_0 (1 - \frac{{\omega_c}^2}{\omega^2})$$

ε_0 is replaced with ε_{WG} in the two previous equations to obtain

$$\varepsilon = \varepsilon_{WG}\left(1 + \frac{\varepsilon_{WG}\frac{16}{3}{r_{ext}}^3 + 4{d_{eff}}^2 r^2 {C_{pul}}^2 L\frac{{\omega_0}^2}{\omega}\left(\frac{{\omega_0}^2}{\omega^2} - 1\right)^{-1}}{\varepsilon_{WG}}\right)$$

Using these two equations with the SRR dimensions chosen previously, the permittivity and permeability are obtained and shown in Figure 30

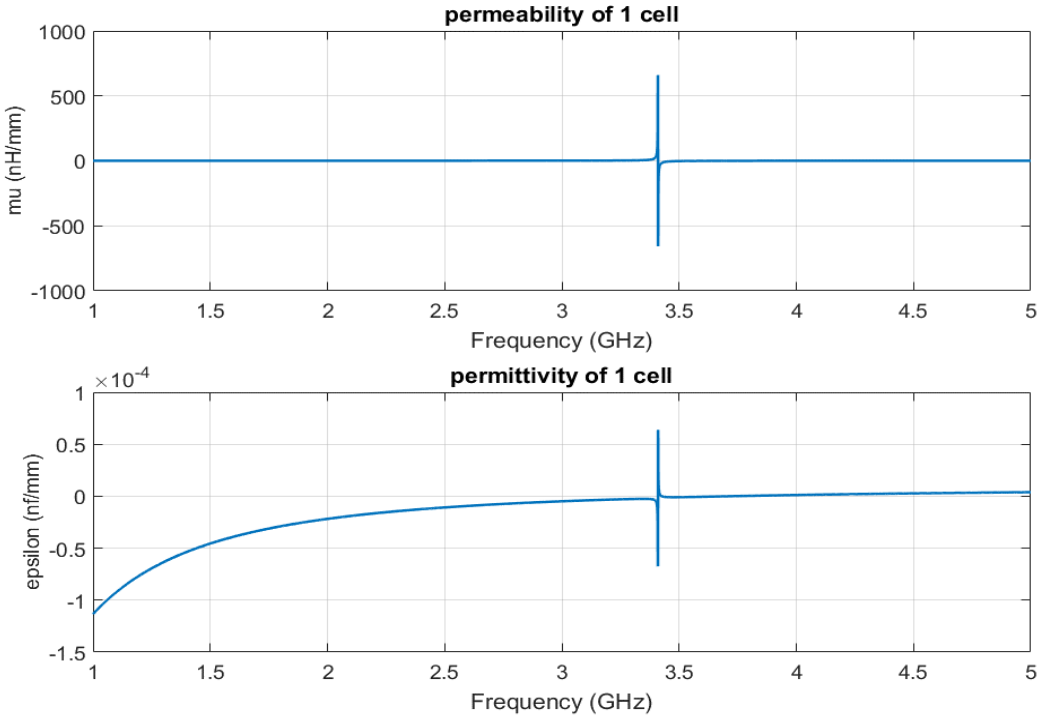

FIGURE 30: MARQUES' MODEL MEDIUM CHARACTERISTICS

The permittivity has an asymptote at the resonance frequency created by the electric polarizability of the SRRs. As opposed to previous models, the SRR here has an influence on the permittivity and contributes in changing its sign around the asymptote. Besides that, the permittivity goes back rapidly to a negative value for higher frequencies and switches sign as expected at the waveguide cutoff frequency. For the permeability, the behavior is similar to the previous model. The only difference between the two models is that the permittivity for this case is negative only for a small

bandwidthstarting from the resonance and stopping at 3.64 GHz. This behavior is closer to reality as ε and μ are negative at the same time only for a small bandwidth which constitutes the passband. Using the fact that [8]

$$\begin{cases} Z' = j\omega\mu \\ Y' = j\omega\varepsilon \end{cases}$$

The line characteristics and S-parameters of the transmission line are derived in a similar fahsion to the previous model. In Figure 31, the characteristic impedance and the dispersion graph are presented.

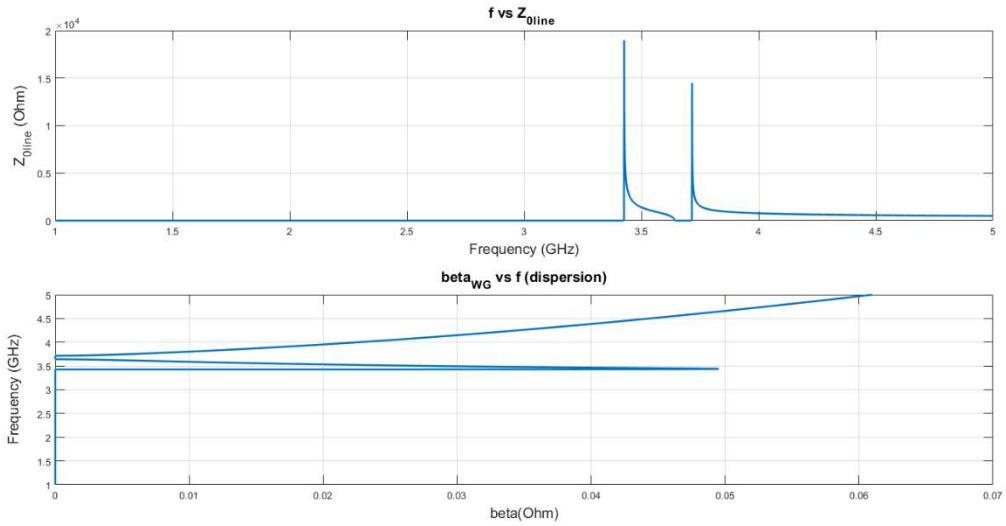

FIGURE 31: MARQUES' MODEL LINE CHARACTERISTICS

The characteristic impedance is real and positive for the same bandwidth where the permittivity and permeability are simultaneously negative. Moreover, in the dispersion diagram, the group and phase velocity are antiparallel for the same bandwidth. Starting from the waveguide cutoff, the group and phase velocities become both positive. This positive dispersion corresponds to μ and ε being simultaneously positive. The S-parameters are using the same equations for the previous model. The S21 has a dip at 3.41 GHz and a peaek at 3.641 GHz. The dip corresponds to a very positive μ and a

negative ε while the peak corresponds to a negative μ and a the negative value of ε created by the combination of the effect of the electric polarizability and the waveguide below cutoff.

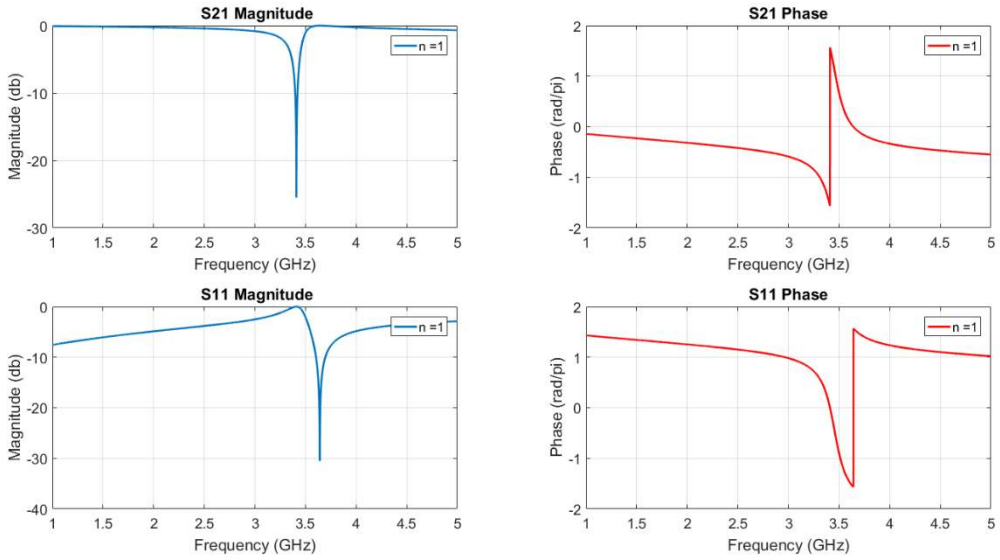

FIGURE 32: MARQUES' MODEL S-PARAMETERS

The dispersion and transmission line characteristics shown by this model map the behavior of the structure.

Extension to multiple cells:

As for the other models, the number of cells is extended to 3 cells. From the permittivity and permeability graphs, it is observed that the absolute value of these characteristics increases with the number of cells. This implies that the diamagnetic response increases with the number of cells.

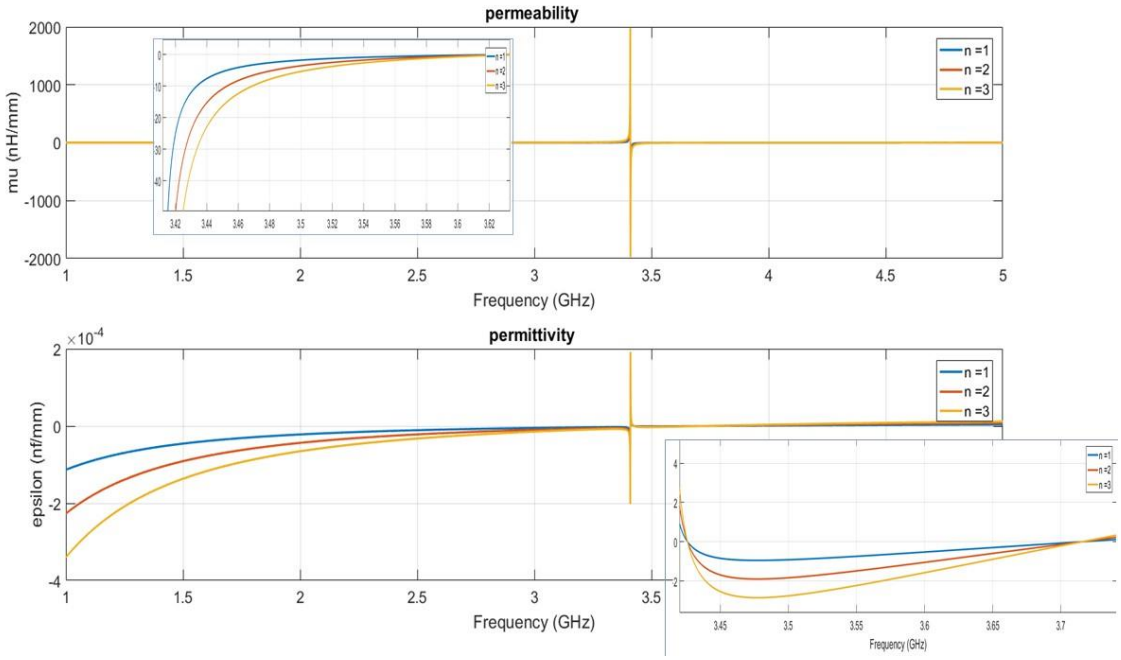

FIGURE 33: MEDIA CHARACTERISTICS OF MARQUES' MODEL FOR MULTIPLE CELLS

On one hand, in the line characteristics, the line impedance is constant. This is same assumptions in the equation in the preivious model are being used. On another hand, in the dispersion graph, the group velocity is decreasing while the phase velocity increases. This suggests that the delay from the power to reach the output port is higher while the speed of the backward wave is increasing with the number of cells. It is easily noted as well in the graph that the passband corresponds to the frequencies where ε and μ are both negative.

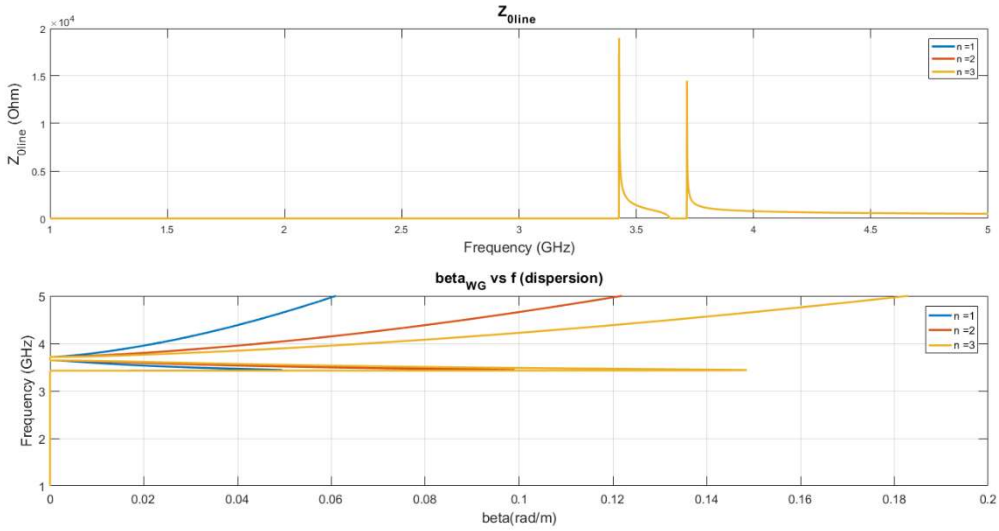

FIGURE 34: MARQUES' MODEL MULTIPLE CELL LINE CHARACTERISTICS

For the S-parameters, the dip and peak in S21 correspond to the same values for one, two or three cells. the bandwidth of the passband is narrower when the number of cells increase as well.

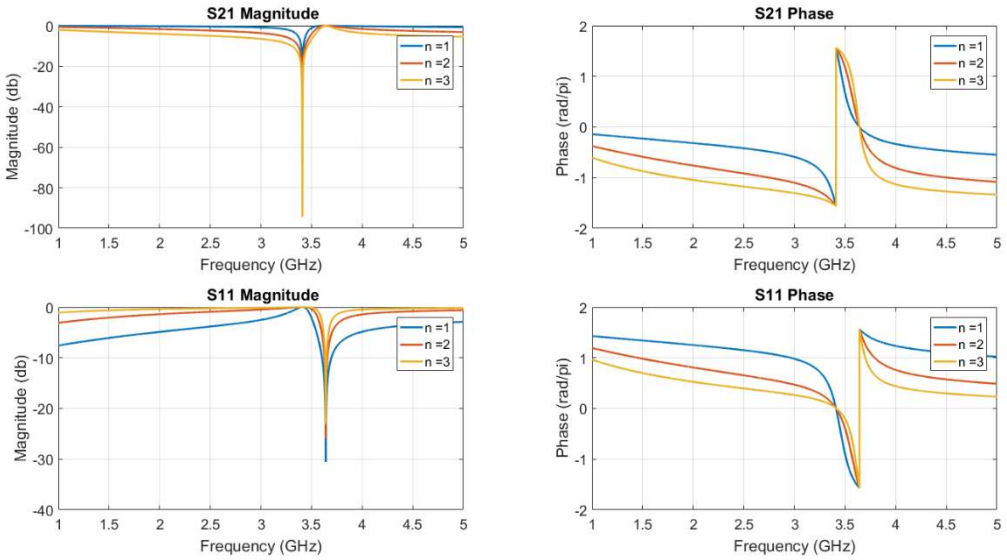

FIGURE 35: S-PARAMETERS OF MARQUES' MODEL WITH MULTIPLE CELLS

An interesting characteristic observed in the S21 figure is that, when zooming near the SRR resonance frequency, a peak is observed that is higher for the 3 cell strucutre and is almost non existent in the 1 cell structure. This peak in reality represents the real first passband created by the SRRs. In fact, due to the asymptotic behavior in the permittivity changes very fast around the resonance frequency from very high positive values to very high negative values. These very high negative values that exist in the frequency region that is slightly higher than the cutoff correspond to the peak of the diamagnetic response. This model highlights the shortcomings of the previous one as the previous model is limited by the relation betwwen the resonance, cutoff frequencies and also the frequencies that represent respectively a pole and a zero for the permeability and the permittivity.

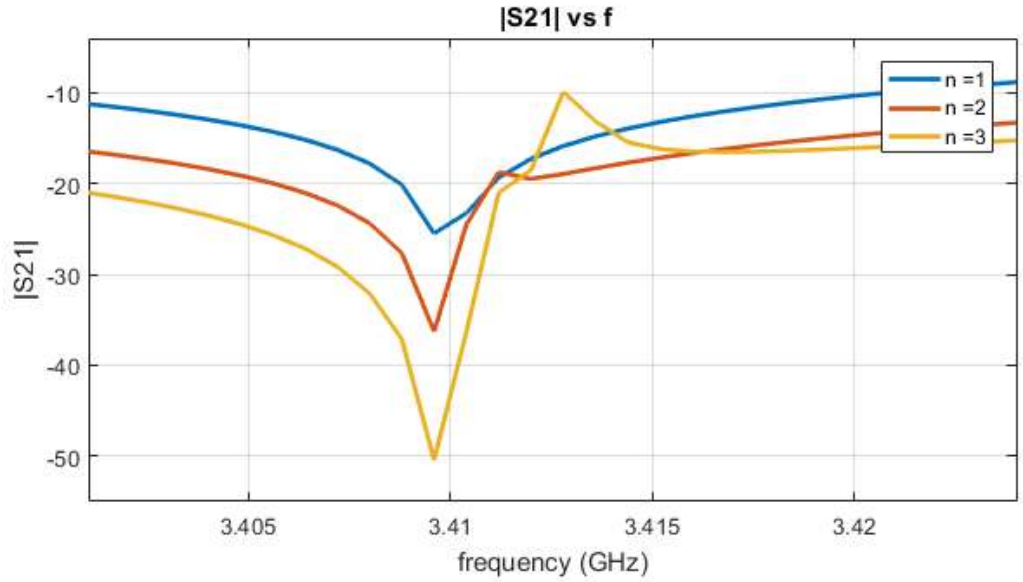

FIGURE 36: ZOOM ON S21 OF MARQUE'S MULTIPLE CELL MODEL

2.4. Summary

In this chapter, a model for SRRs in waveguide below cutoff was developed and detailed. The model was built on the CRLHTL and modified to construct a model compliant with the structure characteritics. The principal drawback of this model is that

it is only valid below for the resonance frequency and does not map the structure's behavior as a whole.

Another approach was also detailed based on Marques' equations and Caloz's model. This model has more realistic results and approaches the properties of the system. The model has as well an identical frequency domain behavior to the SRR structure. These odels will be important in the next Chapter as their capabilities to map the time domain behavior will be tested against the simulated structure and the measured results.

3. Chapter 3: Simulation and Experiment Results

With the rise of interest in metamaterials, a number of different designs have been created and studied. The interest in metamaterials remained mainly focused on the frequency domain characteristics. While the resonance frequency region of SRRs is the principal requirement when designing Split-rings, considering time-domain characteristics is useful for designing and predicting metamaterial behavior. Time-domain characteristics are important in pulsed high power microwaves applications, which focus primarily on the rise time and the amplitude of the microwave generated. If the models detailed in the previous chapter are considered accurate enough to emulate metamaterial behavior, they would then provide a knowledge on the time domain behavior of SRRs.

The goal in this chapter is to analyze the time and frequency domain characteristics of the SRR in waveguide below cutoff structure used, with an emphasis on the time characteristics. A comparison of the results of simulations, measurements and linear models is made. The motivation behind this comparison is to validate the time behavior of the linear model and thus, it will be used as a means of prediction and interpretation of the behavior of the structure.

3.1. Simulated Structure

3.1.1. Structure description

Several simulations were conducted for this work. These simulations aimed at first to reproduce the behavior of SRRs as known. The goal was then shifted from recreating the actual metamaterial structure available in the laboratory to the study of a single cell inside a waveguide. Since any wave becomes evanescent after a certain

distance in a waveguide below cutoff, it was decided that the waveguide in the simulations would have the exact length of a unit cell. The system as described in chapter 2 is comprised of 2 sections of WR-284 waveguide of a length of 30.5 cm and a section of WR-159 of length equal to $n \times 1.2\ cm$, n being the number of cells. The size of the whole system being relatively important, the metallic parts are chosen to be of PEC rather than copper to decrease the simulation time. The SRR dimensions are as specified in the previous Chapter. The simulations are done in CST Microwave Studio, more specifically using the time domain solver. This mode is used for multiple reasons; it has the capability to calculate the structure's S-Parameters after defining the ports and takes less computing time than the frequency mode especially for guided structures. The frequency mode was tried in order to compare the results that both simulations would give but unfortunately, the simulations never converged for the frequency domain. Another important reason for using the time-domain solver in this case is its capabilities to simulate the response of the structure in time with a given input signal. It is important to state that the time-domain solver uses hexahedral meshing along the x, y and z directions while the frequency domain meshing uses tetrahedral meshing.

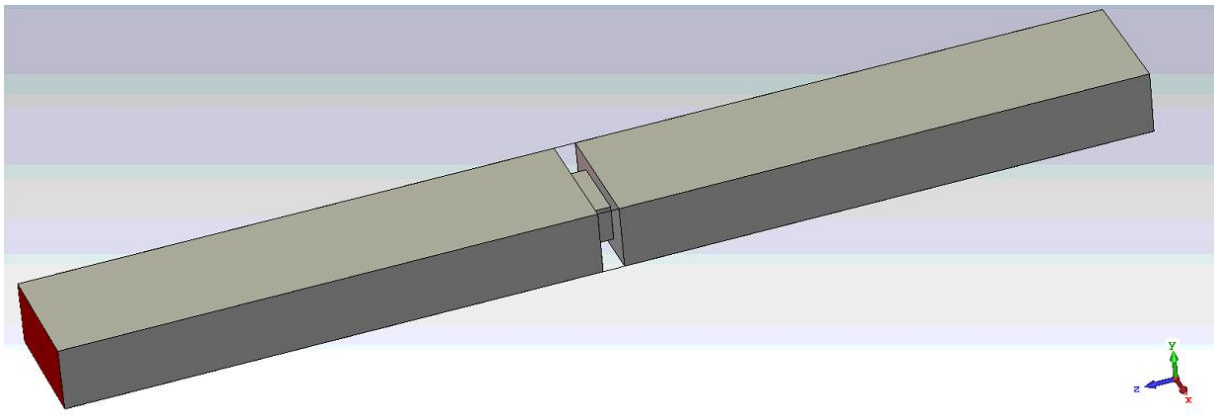

FIGURE 37: SIMULATED STRUCTURE IN CST FOR 1 CELL

Figure 37 shows the structure simulated for 1 cell. The wave in the structure propagates along the z-direction. The SRR is inserted in the central section of the structure that is

one cell length. Figure 38 shows the SRR cell in the WR-159. The SRR rings are floating as the dielectric is chosen to be vacuum and is not represented in the picture. The input signal is chosen for all the simulations to be of TE10 mode, the fundamental mode in rectangular waveguides. This mode has an E-field along the y-direction and an H-field that has a component oriented along x. The rings are placed in the center of the waveguide facing the narrow wall, to be perpendicular to the magnetic field.

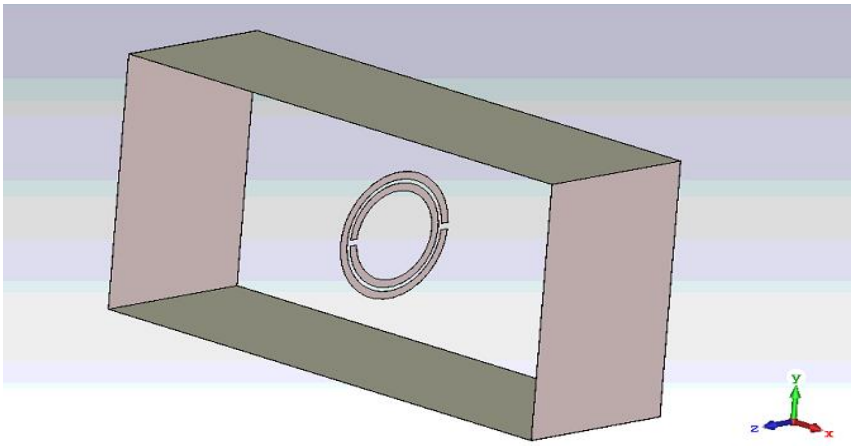

FIGURE 38: SRR CELL IN WG BELOW CUTOFF

In the simulations done at first, the meshing parameters are chosen by the software and refined for each calculation until a certain degree of precision is met. These simulations however have shown unstable results for reasons that are not totally clear. After several tries, it was decided to increase the resolution by choosing the smallest dimension of a mesh cell to be the fifth of the smallest dimension in the structure, which corresponds to the thickness of the SRR's ring (0.017 mm). This increase in resolution results in lengthier simulations, which take approximately from 2 to 3 days each, depending on the number of cells.

3.1.2. Results and Data

For S-parameter simulations, the input signal is left to default, which is a gaussian pulse that is swept over a range of frequencies. For time domain simulations, the signal is chosen to be an exponential sine with a rise time of 2 ns at the resonance frequency. Since this signal is monochromatic, the S-parameters calculated when choosing this input are not accurate and the simulation in only valid for time signals. The meshing parameters are maintained across all simulations.

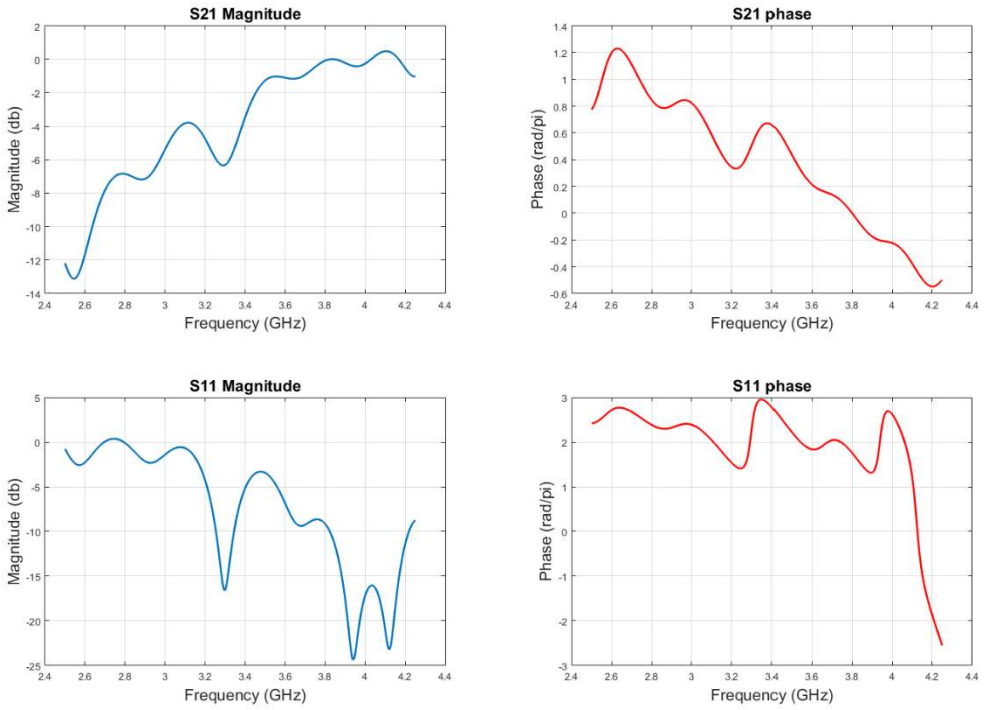

FIGURE 39: S-PARAMETERS OF SIMULATED 1 CELL STRUCTURE

The S-parameter figure shows two clear passband regions. A first narrow passband exists at around 3.3 GHz and a second passband exists starting around 3.9 GHz. While the graph shows results as predicted, with the two successive peaks corresponding to SRR resonance frequency and waveguide cutoff frequency, the S21 graph has an amplitude that exceeds zero in the region above 4 GHz. The S11 graph shows a positive value in dB at around 2.7 GHz. This indicates that the simulation is unstable. Several

unsuccessful adjustments were applied to the simulation to remove these instabilities. S21 and S11 figures show also a dip at the resonance, that is 3.3 GHz. The cause of these instabilities seems unclear but can arise from the resolution of the meshing compared to the size of the ring or the solver's error. This simulation is carried also for 2 and 3 cell structures.

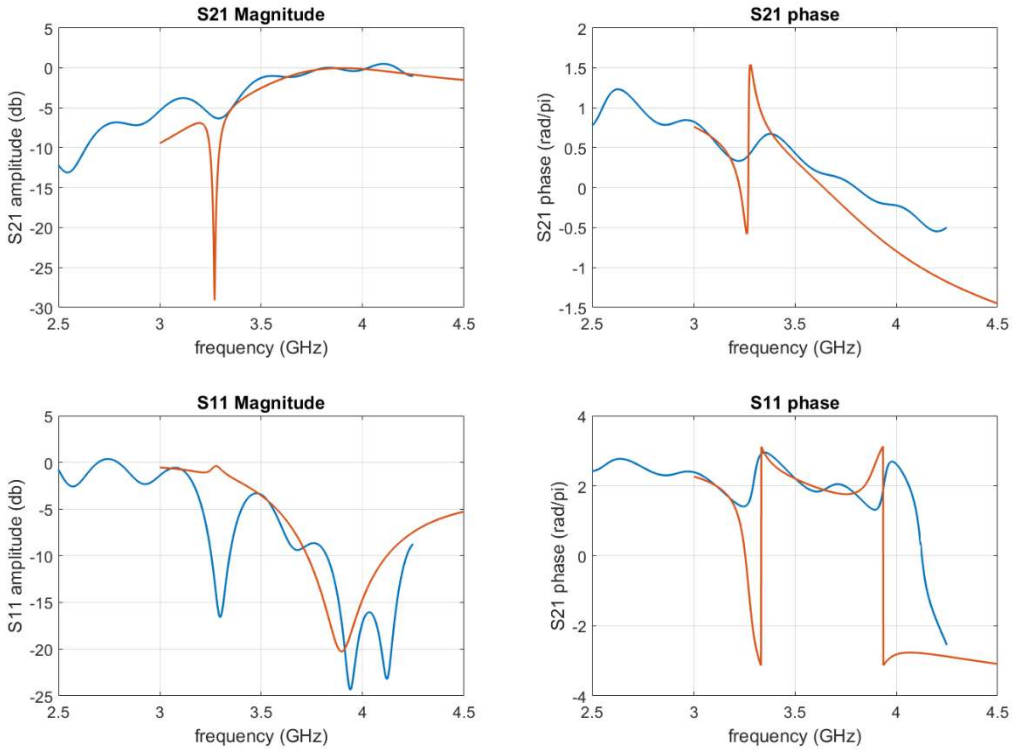

FIGURE 40: 2 CELL SIMULATED STRUCTURE S-PARAMETERS

Figure 40 shows clearly a dip in S21 at 3.3 GHz. This dip reflects similarities with the results obtained in the linear models and that correspond to a combination of a negative permittivity and permeability. This is also reflected in the S11 graph where a peak exists at the same frequency. However, the peak at resonance expected in S21 does not appear and the only noted peak corresponds to the cutoff frequency at 3.9 GHz. Looking at the S-parameters for the 3-cell structure, the dip in S21 at the resonance increases which denotes an increase in the diamagnetic response. This increase induces a steeper slope

of the permeability around the asymptote. The cutoff dip in S11 for the three-cell structure is as well shifted to 3.81 GHz, approaching a more realistic value. The S11 graph shows, similarly to the two-cell structure, a small dip and a peak around the resonance. While a dip should exist at this frequency, it is expected to be followed by a peak corresponding to the first passband of the structure. A few ripples are as well noted in the S-parameter graphs which ca be an indicator of instabilities in the simulations.

From the phase graphs of the S-parameters of all the structures, abrupt phase changes are noticed especially at resonance. It is also unclear if these changes are due to phase wrapping or is an effect of the structure on the incident wave.

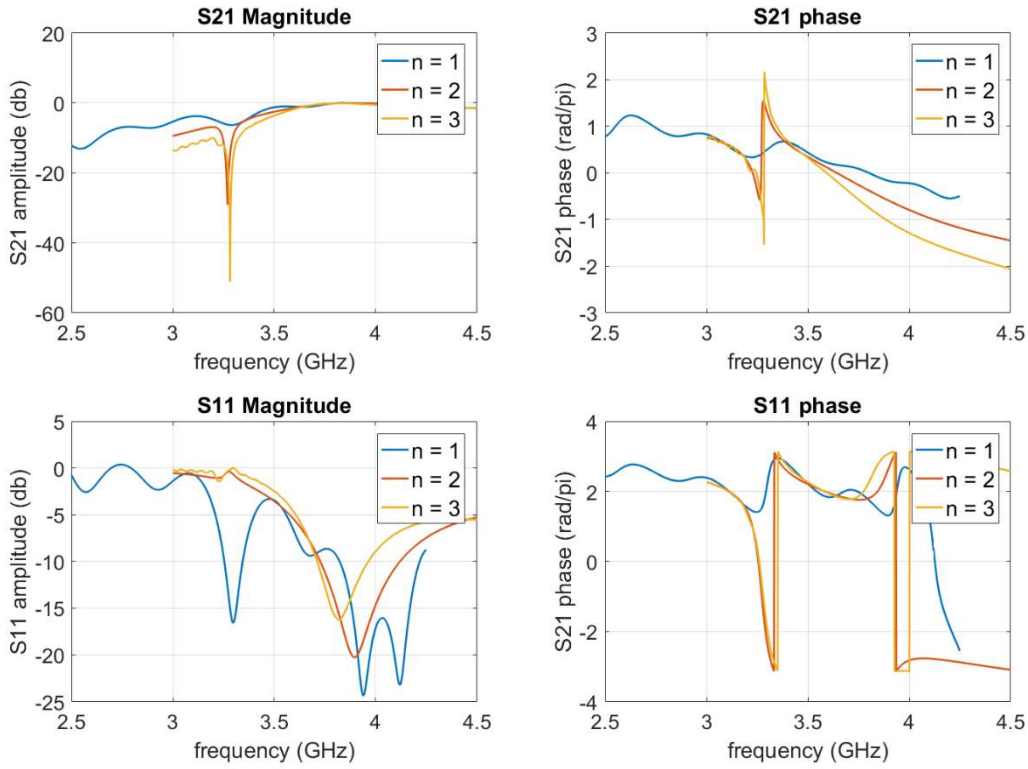

FIGURE 41: S-PARAMETERS OF THE3-CELL SIMULATED STRUCTURE

It is important to note as well that the values of the target frequencies, 3.4 GHz for the resonance and 3.7 for the cutoff are shifted respectively to 3.3 and approximately 3.9

GHz. Using the S11 figures to determine the resonance frequencies of the 1, 2 and 3-cell structures, a sinusoidal signal with a 2 ns rise time is set as an input and propagated. The signal is 50 ns long. Figure 42 shows the time signals of a single cell structure. The transmitted and reflected signal have a delay of 2.5 ns compared to the input. The transmitted and reflected signals both rise to 50% of the input's maximum at 4.5 ns and start decreasing. While the transmitted signal keeps decreasing until it is almost inexistent, the reflected signal decreases and starts increasing again from 8.25 ns.

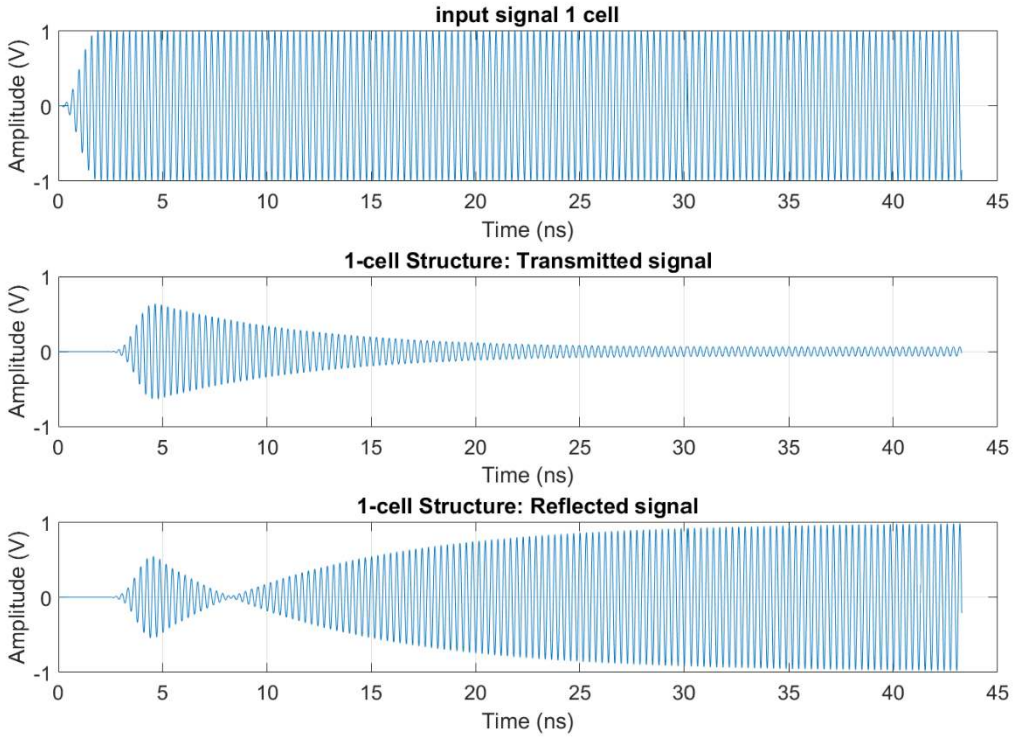

FIGURE 42: TIME SIGNALS THE FOR THE 1-CELL SIMULATED STRUCTURE

Figure 43 represents the time signals of the two-cell structure. The same initial delay of 2.5 ns is observed. The transmitted signal increases initially and then decreases, showing a behavior similar the one-cell structure at first. However, starting from around 7 ns, the signal increases again and a stable behavior is observed, where oscillations decrease slowly to stabilize around a constant. At the end of the 50 ns, the signal is at

44% of the input. When compared to the 1-cell structure, the signal of this structure has a higher amplitude. This can be attributed to the coupling between the rings that allows the signal to propagate and to build up over time. If multiple ring cards were placed, as in [17], the diamagnetic response is expected to be higher, and consequently the amplitude of the transmitted signal should increase as well. The reflected signal graph shows the same initial delay as all the previous cases. It increases up to 62% of the input at 4.61 ns then decreases and increases again to reach a maximum of 1.014 V at 12.47 ns. The reflected signal exceeds the maximum of the input signal which is an indicator of energy storage in the cells. The signal's oscillations then diminish, and the signal settles around a value of 88% of the input at 50 ns

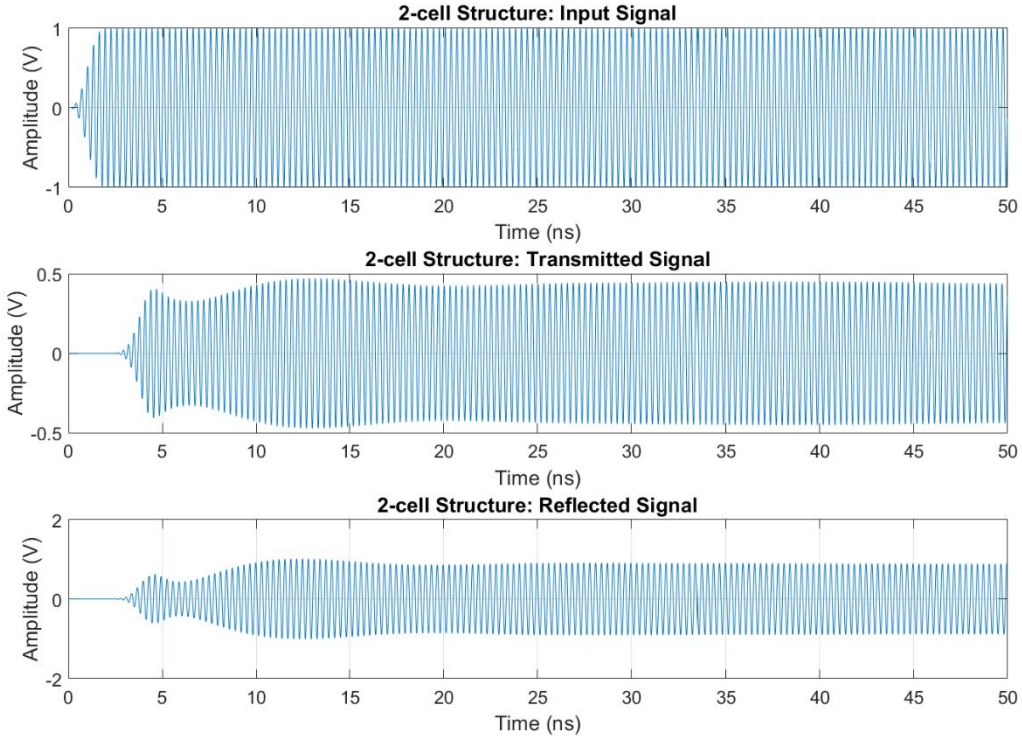

FIGURE 43: TIME SIGNALS THE FOR THE 2-CELL SIMULATED STRUCTURE

Figure 44 shows the signals for the three-cell structure. Initial delay similar to the one and two-cell structures is observed. Oscillations are as well present in the transmitted

and reflected signal but are diminished, and the output signal reaches a steady state faster than the two previous cases. In fact, the signal rises to 47% of the input at 5.2 and decreases slightly and reaches a second maximum at 7.9 ns (52% of the input). The reflected signal sees some oscillations as well before stabilizing at around 0.858% of the input at 50 ns. We note also multiple peaks in the rise time of 0.58V at 4.8 ns and 1.005V at 8.07ns. The signal then decreases and starts to stabilize around the value mentioned above.

The reflected signals in these cases give multiple indications. First, the amplitude of the signal reflected indicates a poor matching of the structure. In fact, the rings' impedance added to the cross-section change from the WR-284 to WR-159 create important changes in the structure's impedance that create important amounts of reflection. The magnitude of the reflected signal exceeding the input's maximum indicated that an amount of energy is stored in the rings and released with a delay.

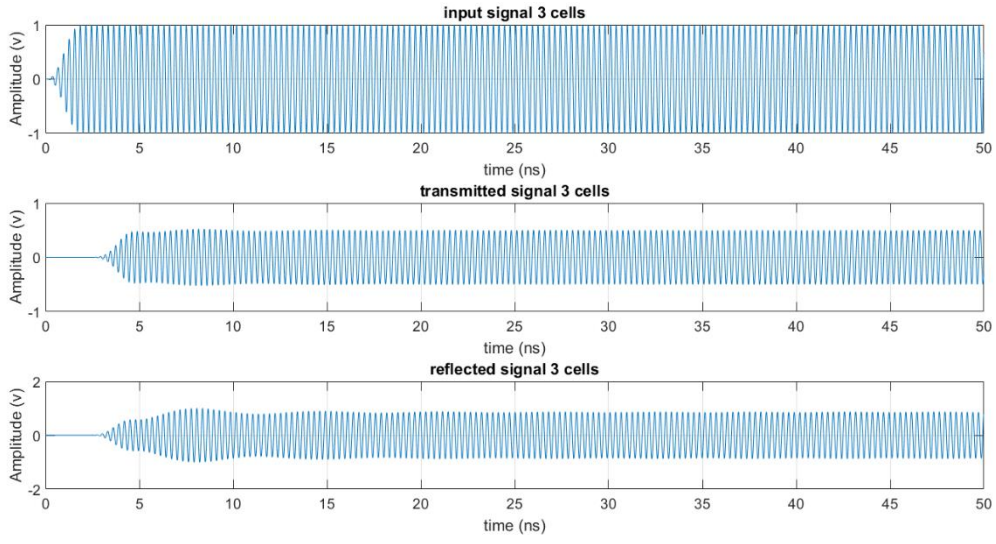

FIGURE 44: TIME SIGNALS FOR THE 3-CELL STRUCTURE

Figure 45 shows the envelopes of the transmitted signals of the structures that are normalized to their respective maximums. The rise time is almost identical for all the

structures. In fact, the three signals show comparable initial rise times of approximately 4.6, 4.5 and 4.8 ns. While the signal of the one-cell structure seems to be the most stable one, it decreases rapidly when compared to the two and three cell structures, to reach a value of 10% of its maximum. This suggests that the behavior of one cell is different than the behavior of multiple cells, as for once cell only, a big portion of the signal gets reflected and the portion that is transmitted is passed on to the output port is attenuated to less than 10% of its maximum peak. The signal is attenuated below 10% of its maximum at 34.6 ns. However, the signals of the two and three-cell structures show an increased output signal compared to the one-cell. The two-cell structure output has an initial rise time similar to the other structures, then decreases and rises again to its maximum at 12. 96 ns. The signal then oscillates in a marginal stability fashion and stays above 90% of its maximum starting from 9.81 ns. The three-cell structure signal shows behavior similar to the previous structure, with a similar initial rise time but a higher peak, and a depth of modulation that is smaller than the two-cell structure. The output reaches its maximum at 8.07 ns and then saturates faster than the previous structure. Zooming on the figures shows also a higher modulation frequency than the previous signal, however, this could be an effect of the envelope calculus.

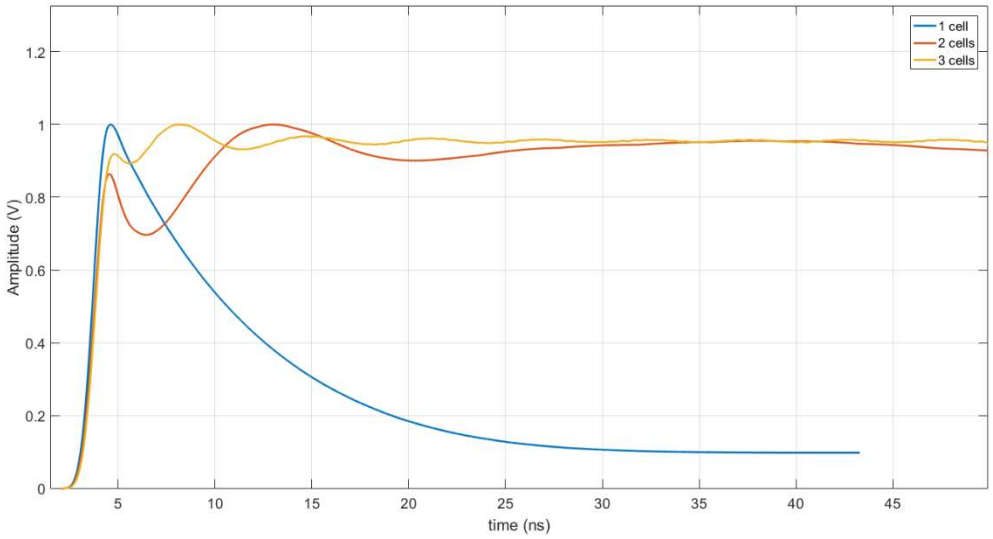

FIGURE 45: NORMALIZED TIME ENVELOPES

In Figure 46, the empty waveguide output was added to the signal, after taking its envelope and normalizing it. The empty waveguide signal shows that the rise time of the structure without any SRRs is very close to the other structures' initial rise times. This demonstrates that the SRRs do not change the initial rise time of the structure and thus, do not play a role in the first time constant in the structure. The no-SRR system shows as well that the rise time of the empty structure is the closest to the one cell structures and is slightly faster than the other structures. The slowed rise time for the multiple cell structure indicates that the rings are loading and switch afterwards to an unloading cycle that leads to an output higher than the input magnitude. The cycles seem as well more frequent with the number of cells. Indeed, the number of rings plays an important role in shaping the output signal and indicates the importance of the coupling between rings in carrying out the output signal. The number of rings seems also to increase the stability with a smaller depth of modulation, a shorter settling time and a higher output magnitude.

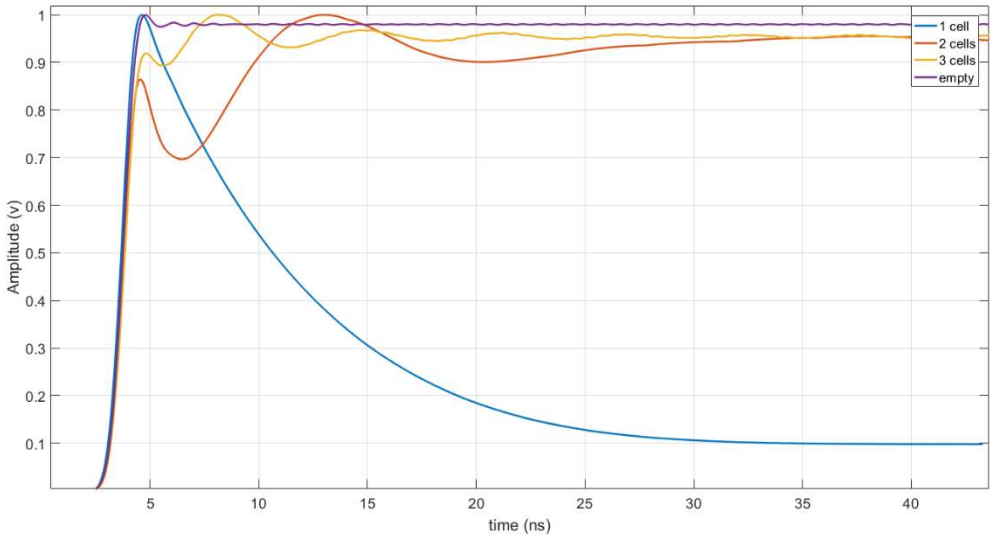

FIGURE 46: NORMALIZED TIME ENVELOPES INCLUDING EMPTY STRUCTURE

3.2. Experimental Setup

3.2.1. Experimental Setup

The experimental set up is the initial set up in [17]. As mentioned in Chapter 2, it is composed of 2 WR-284 waveguide sections with same length as simulations and one section of WR-159 of 11.43 cm with two brass zero-length reducer flanges that add 3.175 cm to the cutoff region. This center waveguide section is filled with the SRRs and the low dielectric foam mentioned previously. The set up shown in figure 47 and described by the diagram in figure 48 is composed as well of:

- One HP8620C sweep oscillator mainframe and HP86290C RF plug-in. the oscillator and the plug-in together constitute a multiband swept signal-source. For the experiment's purposes, the Frequency band used will be 2-6 GHz.
- One HP8566B Spectrum Analyzer, 100 Hz to 22 GHz
- One DG645 digital delay/pulse generator that provides pulses at repetition rates up to 10 MHz.

- One Mini Circuits coaxial fast switch, ZYSW-2-50DR, that functions from DC to 5 MHz with a TTL power supply

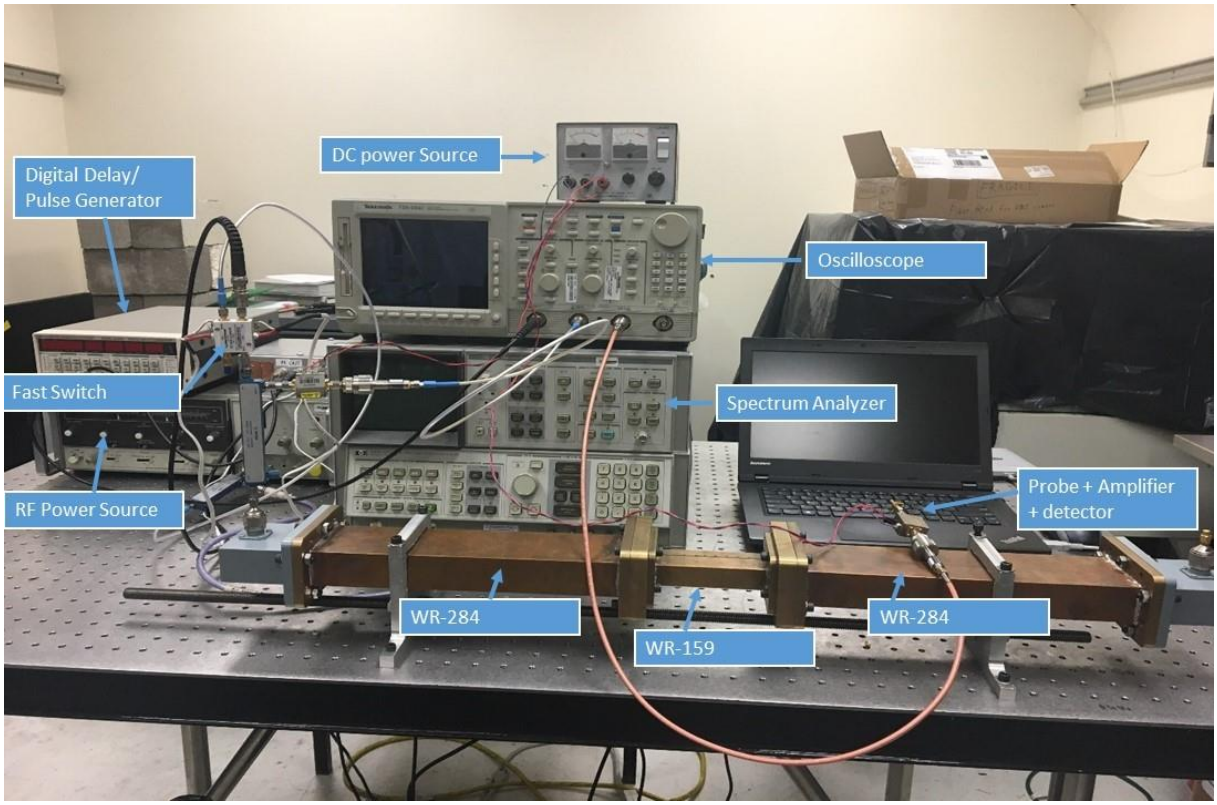

FIGURE 47: EXPERIMENTAL SET-UP

- One LAMBDA LA-300 Regulated DC power supply, 0-20V/0-10A
- Two Krytar 209A zero bias Schottky detectors, that work for a range of frequencies from 100 MHz to 18.5 GHz with a negative output polarity. These detectors take the envelope of the time signal and are useful in looking at the rise time of the signals and to look at the group velocity properties.
- Two Krytar Directional Couplers, Model 1211 with a 10-dB coupling
- One Tektronix TDS 694C Digital Real-Time Oscilloscope with a resolution up to 10 Giga samples per second.
- Mini-circuits connectors, with the dielectric taken off and replaced by Kapton tape

- Two Picosecond Labs 5828A AC coupled, Ultra-Broadband Amplifiers (65 kHz to 15 GHz) with a gain of 10 db.

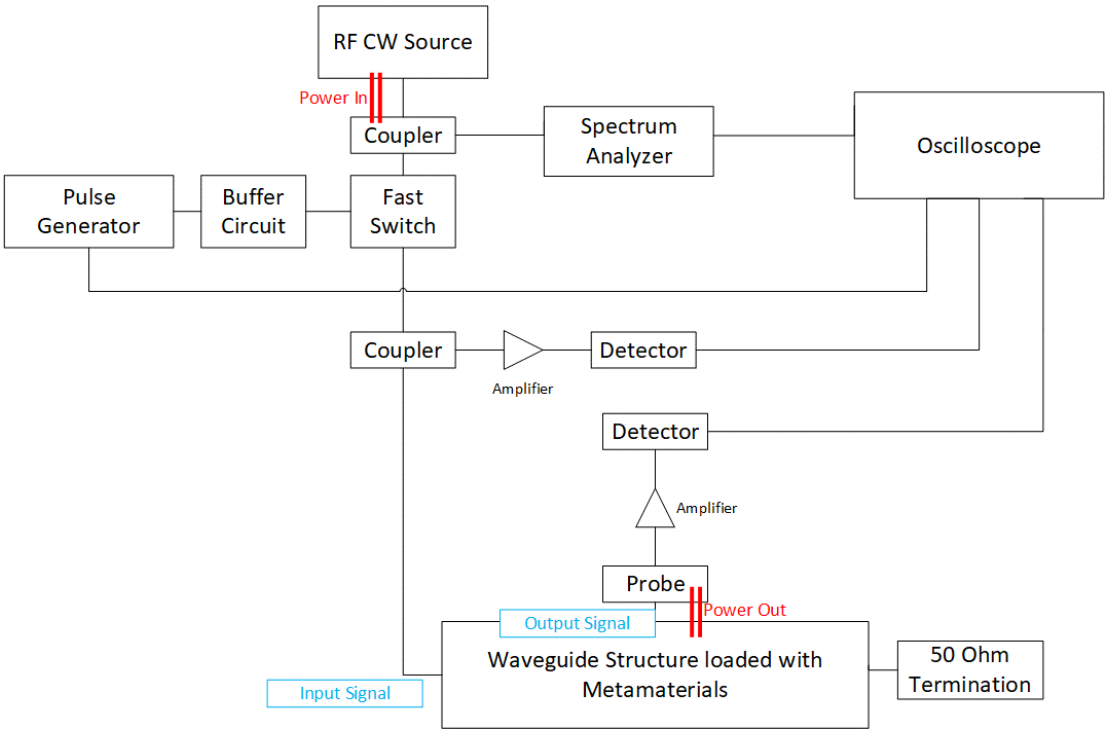

FIGURE 48: SCHEMATIC OF THE EXPERIMENTAL SETUP

- Buffer circuitry is also placed in line between the trigger generator and the switch to protect and power the switch and help reduce losses.

It is important to state that, to be able to measure the signals after 1,2 or 3cells, a slot was cut in the waveguide. Figure 49 shows the WR-159 slotted waveguide section and the probe inserted in it with the amplifier and the Schottkey detector.

For S-parameter measurements, the following equipment was used:

- PNA-X 5247A Vector Network Analyzer (VNA)
- 2.5 mm Calibration kit
- 3.5 to 2.4 mm coaxial adapters

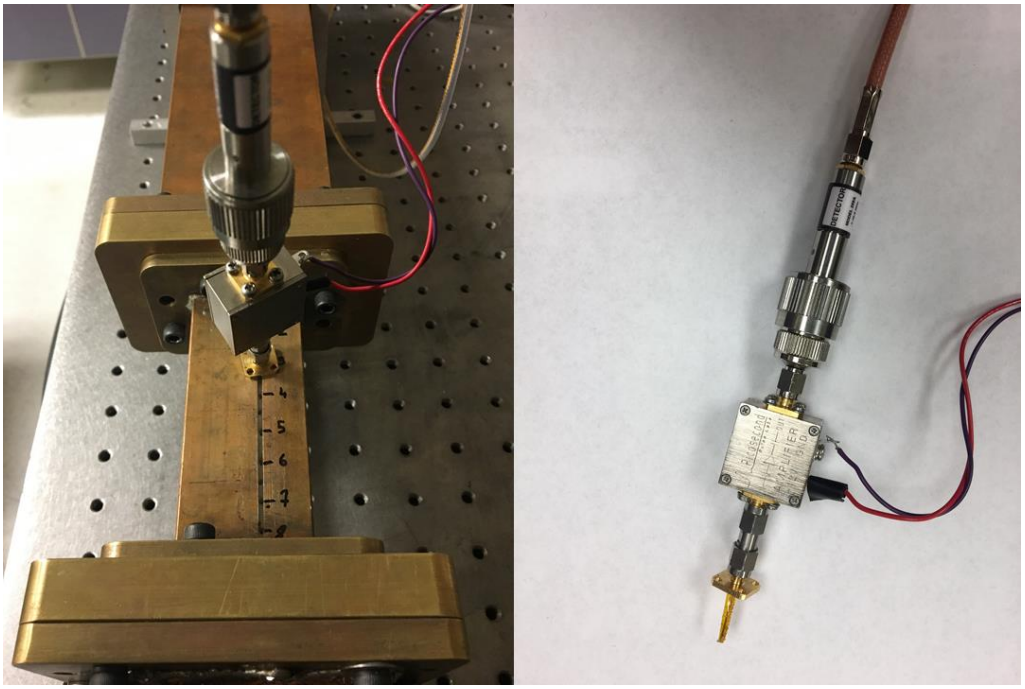

FIGURE 49: LEFT- PROBE +AMPLIFIER + DETECTOR INSERTED INTO SLOTTED WR-159; RIGHT - PROBE + AMPLIFIER + DETECTOR ATTACHED TO AN RF CABLE

3.2.2. Results and Data

The S-parameter of the structure are measured using the Vector Network Analyzer (VNA). Port-1 of the VNA is the input port where the input signal is fed. Since it is impossible to obtain a signal with one, two or three cells by measuring at the output of the structure, the signal is measured from the probe at the cells' edges, with the mini-circuits connector through the slot in the waveguide. Figure 52 shows the slotted waveguide and the probe positions that correspond to a unit cell length. The S-parameter figure shows the presence of multiple dips in S11. While the peaks in S21 are hard to determine, S11 shows the presence of dips at 2.82, 3.28 and at 4.06 GHz. Given that the experimental set-up has several discrepancies with the simulation, it is expected that the resonance frequency will be shifted from its theoretical value. Indeed, materials such as copper, the dielectric, the foam need to be accounted for.

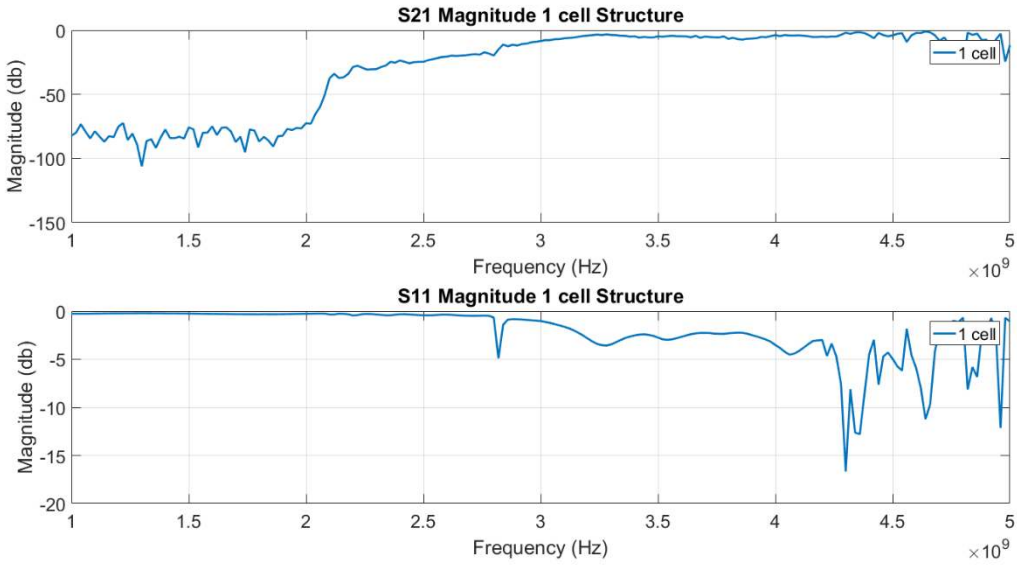

FIGURE 50: MEASURED S-PARAMETERS OF 1-CELL STRUCTURE

Other parameters like the waveguide slot, the alignment of the SRR cards, the impedance difference between the WR-284 and the SRR-filled waveguide or the probe can affect the resonance as well. Similar shifts in frequency have been seen in the set-up of [17] which uses the same rings. The position of the rings and the probe have also a crucial importance in determining the resonance frequency. In fact, the rings need to be perpendicular to the H-field direction to assure a maximum diamagnetic response which can be cumbersome to achieve when the cards contain only up to three rings. The first dip in S11 at 2.82 GHz is attributed to the resonance. The second dip at 3.28 GHz is however unclear. It either corresponds to a second passband in the filter structure, which suggests that the permeability changes sign multiple times in the frequency band. This assumption is in contradiction with the well-established equations in [16]. This also can correspond to the cutoff frequency that might have been shifted due to all the aforementioned parameters and/or to a change in permittivity. While it is known that the SRRs have an influence on the relative permittivity of the structure, it

is expected to happen at the resonance and not in a frequency that is between the measured and expected frequencies of resonance.

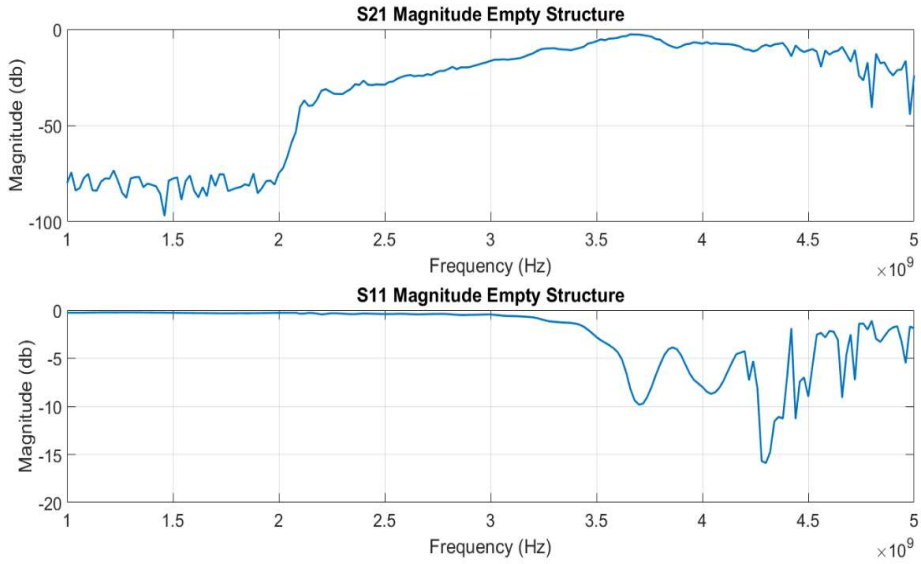

FIGURE 51: EMPTY STRUCTURE (NO SRR) MEASURED S-PARAMETERS

Figure 51 shows the S-parameters of the empty structure. As expected, the waveguide starts passing signals at its cutoff frequency; 3.7 GHz. The dip at 3.28 GHz value will be then attributed to the cutoff frequency as a certain amount of power transmitted can be observed starting from this frequency. The third dip in S11 is then simply attributed to the region of maximum transmission for the 1-5 GHz frequency band.

For the 2-cell structure, signals are probed at the end of the first and at the end of the second cell. Since one cell is 1.2 cm long, the signals are probed at 1.2 and 2.4 cm from the edge of the waveguide. The characteristics are identical to the 1 cell structure's as we see dips in S11 at 2.82, 3.28 and at 4.06 GHz. Besides that, the S21 graph shows the presence of a dip followed by a peak around 2.8 GHz which is attributed to the asymptotic behavior of the permeability. This confirms that the transmission seen at that frequency is due to the resonance of the SRRs. The purpose of measuring S-parameters after the first cell is to observe coupling between two

consecutive cells in the structure. The dips and peaks in S21 and S11 at 2.4 cm are slightly shifted from the ones at 1.2 cm. These results are heavily affected by the position of the connector inserted.

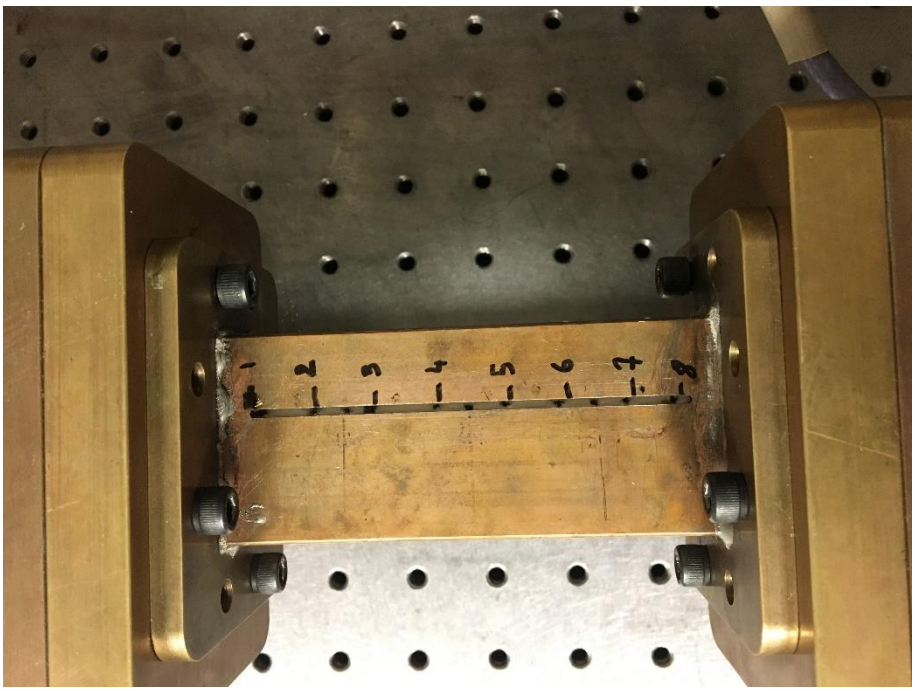

FIGURE 52: SLOTTED WR-159 WITH DEFINED PROBE POSITIONS EQUAL TO 1 CELL LENGTH

The same experiment is repeated with the 3-cell structure where S-parameters are measured after 1, 2 and 3 cells respectively at 1.2cm, 2.4cm and 3.6 cm. For the 3-cell structure, the first S11 dip corresponds to the previous structures. The following dips are however slightly shifted, with the peak of resonance corresponding to 3.48 GHz and the waveguide cutoff corresponding to 4 GHz.

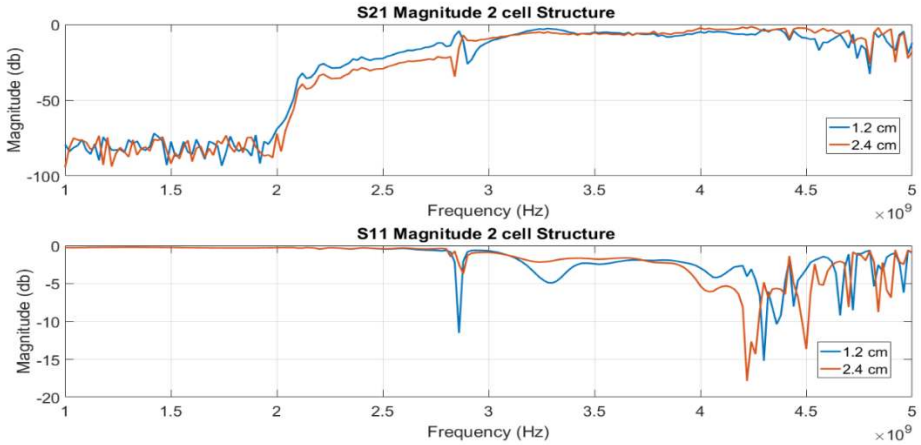

FIGURE 53: 2-CELL STRUCTURE MEASURED S-PARAMETERS AT 1.2, 2.4 CM POSITIONS

Figure 55 illustrates the time-signals for the 1- cell structure. The pulse delay from the pulse generator is set to 100 ns, which is the lowest delay for which a signal could be detected. The frequency of the input signal is visualized in the spectrum analyzer.

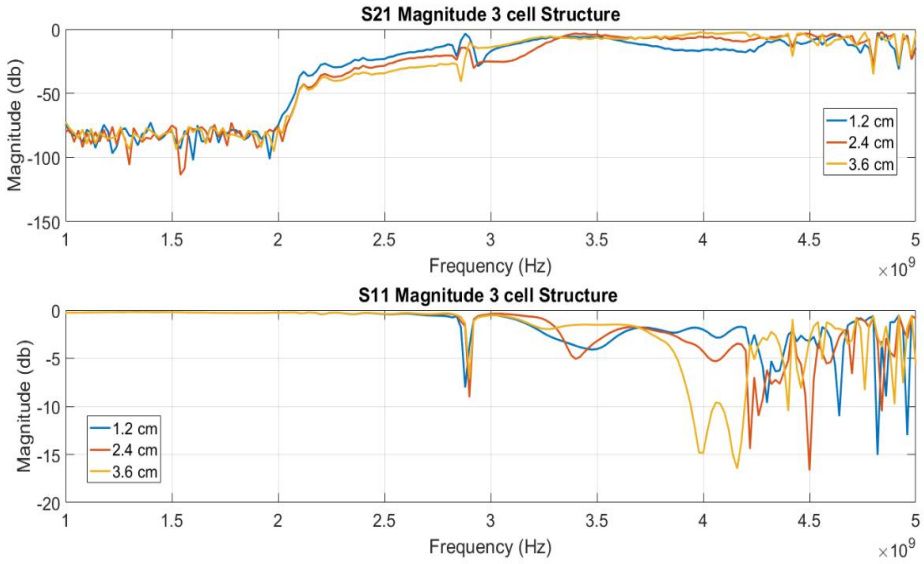

FIGURE 54: 3-CELL STRUCTURE MEASURED S-PARAMETERS AT 1.2, 2.4, AND 3.6 CM POSITIONS

The structure's input signal is obtained from the coupler placed after the switch. This signal observation allows to calculate the delay generated by the system from the input to the input port of the waveguide structure. Like the S-parameter measurements, the output time signal is taken measured using the mini-circuits connector inserted in

the slot at different positions representing the edge of the rings. The measurements are taken at the first peak of transmission, which corresponds to the first dip observed in the S11 graphs. The figure shows a delay of 25 ns between the pulse and the input and output. This delay is caused by the elements between the pulse generator and the input of the waveguide structure (switch, cables, couplers, etc.). However, the delay between the input and the output signal is only a few nanoseconds (2.4 ns). Besides that, both signals have an initial rising curve composed of three linear slopes before saturation. Looking also at the decay of the signals, the input-output delay is slightly increased to 4 ns in the decay phase. Observing the decay slopes, we note that the input and output slope are linear and follow the decay of the pulse.

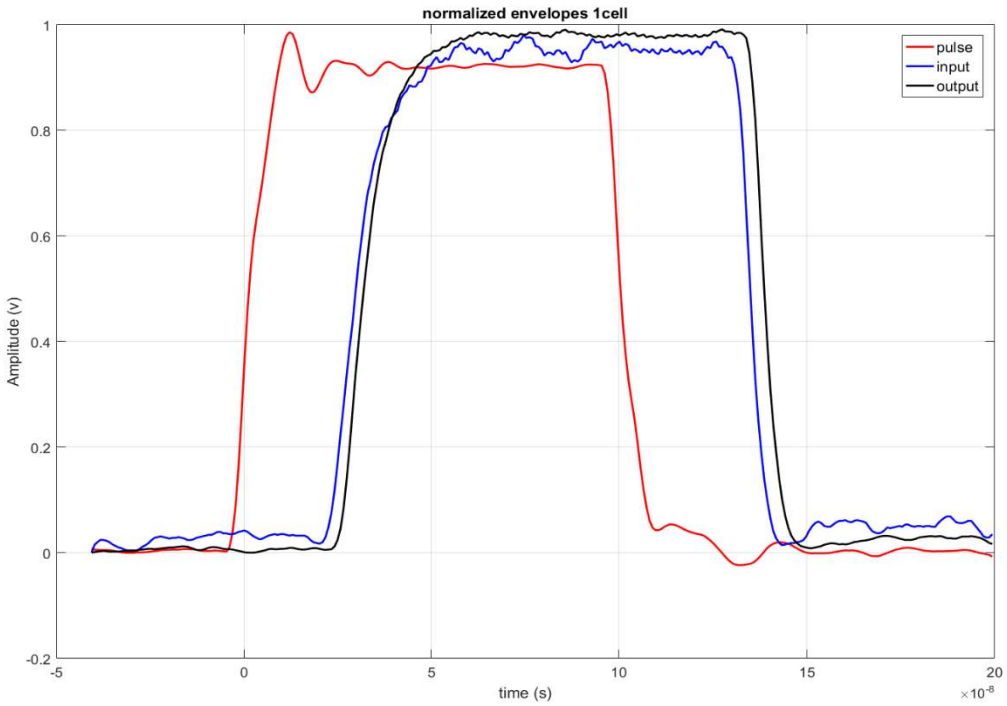

FIGURE 55: NORMALIZED ENVELOPES OF MEASURED TIME SIGNALS - 1 CELL

If we observe the sinusoidal signals and normalize them (figure 56), it is unclear which signal starts to rise first, however the peak wave fronts of the output are leading the peaks of the input. Since the system is causal, the output cannot be generated when

there is no input. However, the phase delay between input and output can be between $\pi + 2k\pi$ and $2(k+1)\pi$ rad. This phase delay indicates the presence of a backward wave since, as seen, the output signal is leading the input, but the output envelope is lagging. This shows that the phase and group velocity are antiparallel.

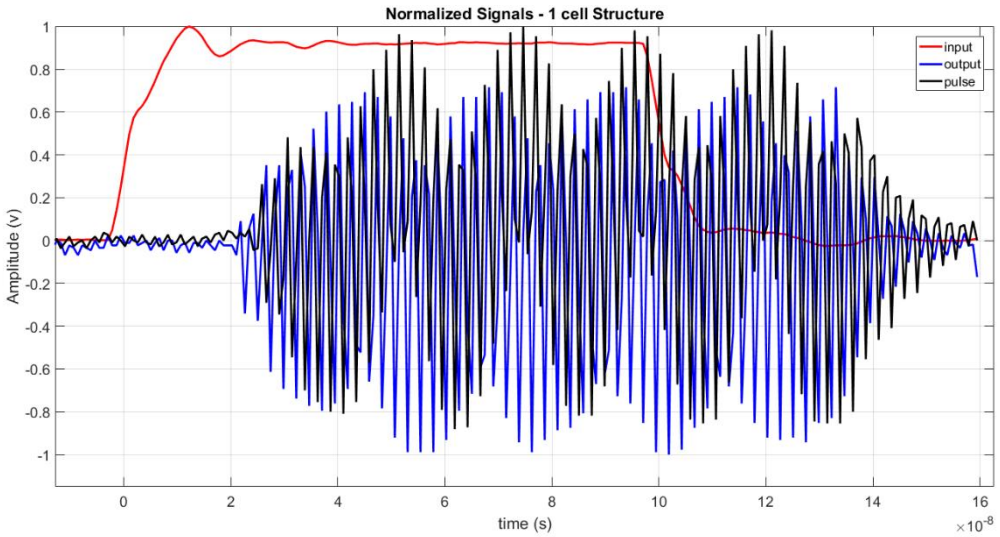

FIGURE 56: NORMALIZED MEASURED TIME SIGNALS FOR 1 CELL STRUCTURE

Figure 57 represents the signals measured for the two-cell structure. The output is measured between the two cells and at the end of the second cell. The initial delay between the input and outputs is of 3.8 ns. The signals at 1.2cm and 2,4 cm seem to start increasing at the same time at first, but the signal at 2.4 cm takes more time to reach its maximum and the delay increases at 6.7 ns at 96% of the maximum. Looking at the decay phase, both signals have a comparable behavior where they decay linearly and almost simultaneously. Both outputs are delayed by 3 ns from the input.

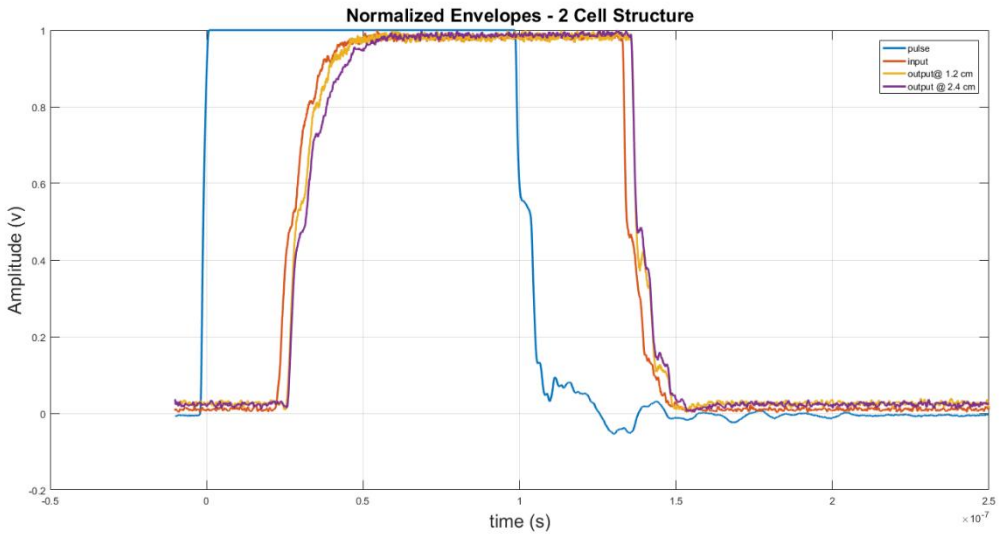

FIGURE 57: NORMALIZED TIME SIGNAL ENVELOPES - 2 CELL STRUCTURE

Looking as well at the sinusoidal signals in figure 58, the signal at 2.4 cm leads the signal at 1.2 cm. The delay between input and outputs increased drastically to 30 ns as well, indicating that more power is being stored in the structure. The delay however between the two output positions is minimal (below 3ns), seems to be negative although this cannot be verified.

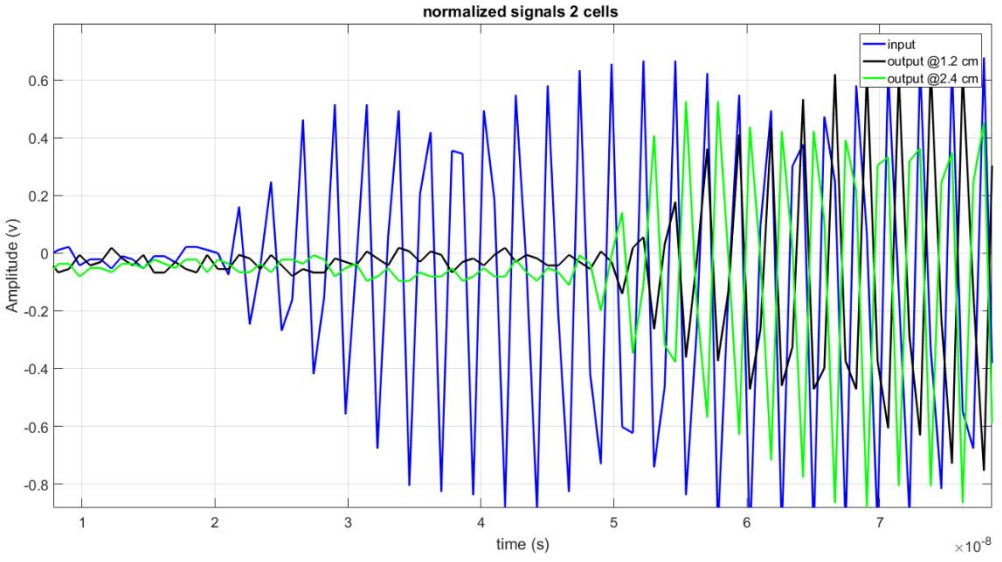

FIGURE 58: NORMALIZED MEASURED TIME SIGNALS FOR 2 CELL STRUCTURES

For the 3-cell structure, the behavior is similar to the behavior observed previously. The initial delay between input and output signals approaches 2.5 ns. We also note that the rise time of the envelope is inversely proportional to the number of SRR cells. In fact, the signal at 1.2 cm has a faster slope than the signal measured at 2.4 cm and similarly, the signal at 2.4 cm has a faster slope than the signal at 3.6 cm. Looking at the decay of the pulse, it is noted that the signal at 1.2 cm decays faster than the other two measured signals, which have a very similar decay slope. Besides that, the sinusoidal signals show the same behavior observed previously, reinforcing the idea that the negative phase velocity is causing this delay to look negative.

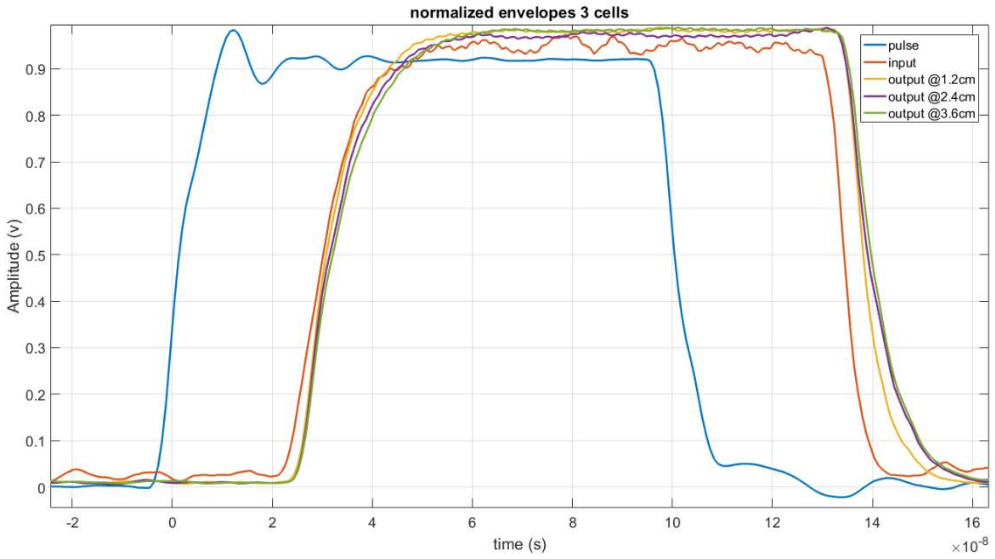

FIGURE 59: NORMALIZED MEASURED TIME SIGNAL ENVELOPES - 3 CELL STRUCTURE

The interpretation of the observed measurements is difficult as the results are not always repeatable. However, in all these different measurement set-ups, a certain degree of repeatability is observed, and some characteristics are preserved across all measurement cases. All the signals in the structure show a rise time composed of three slopes. These slopes, which were already mentioned in [17] are a result of the behavior

of the SRRs and the combination of all the other parameters, such as the time characteristics of instrumentation, the time behavior of the waveguide. Figure 60 shows the measured envelope signals for an empty waveguide structure. The input and output are almost superimposed when the signal starts rising. Both signals have at least two rising linear slopes. However, the output signal takes more time to decay than the input and has two decay slopes instead of a very fast linear one. This is most likely an effect of the dispersion characteristic of the waveguide combined with the system's losses. The absence of an important delay in the rising phase of the input and output signals for this case comforts the hypothesis of the SRRs in slowing down the rising slope of the output. The SRR cards are reactive structures that absorb energy and slow down the propagation of the signals. This interpretation is in phase with the approximations of Marques and Caloz and reasserts the findings in [17].

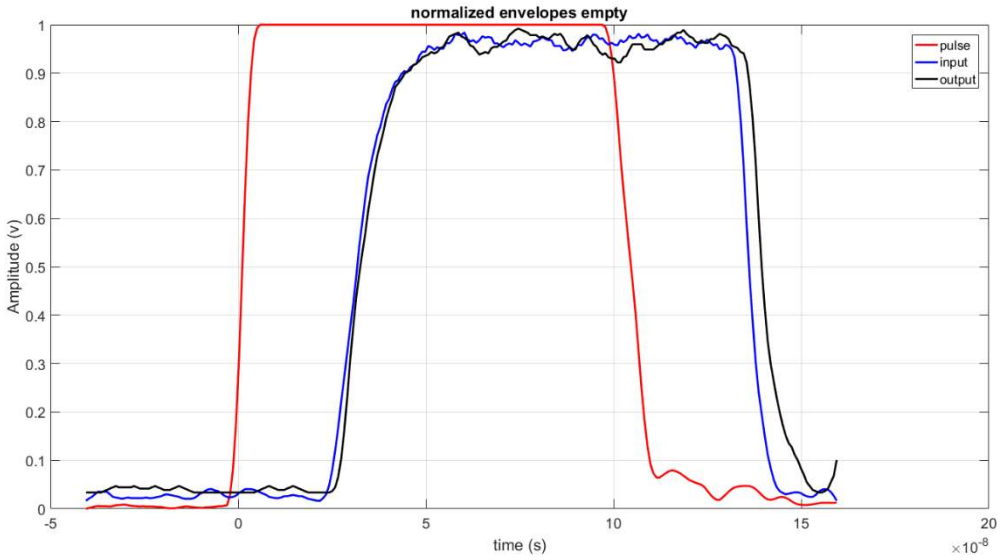

FIGURE 60: NORMALIZED TIME SIGNAL ENVELOPES – NO SRR STRUCTURE

3.2.3. Summary

The simulations and Measurements presented in this chapter showed interesting similarities that give hints about the SRR behavior in the cutoff waveguide. There's an agreement across all time-domain figures that the initial delay is independent from the SRRs and is most likely due to the delay in the WR-284 sections. Moreover, the simulations and experiment have shown resonance peaks in S21 at frequencies that are comparable, if the losses and effects of the materials and instrumentation are considered for the experimental setup. The simulations have shown also that the rise of the signal is similar for the 1, 2 and 3-cell structures. In the meantime, the settling time for the structures increases with the number of cells while the oscillations decrease in depth but have a faster frequency. The measured signals showed that the delay between input and output increases with the number of cells and that all the signal envelopes showed a rise time composed of 3 slopes, as found in [17]. An interpretation of the behavior observed could be that the coupling between the rings enables the power to fluctuate through the structure, allowing the power to exit out from the output port. The coupling between the rings reinforces the oscillations and create a marginal stability to enable power to come out. This is confirmed by figure 46 where the oscillations in the envelope decrease with the number of cells. This behavior unfortunately was hard to observe in the measurements.

While these interpretations remain attempts in explaining the behavior of SRRs and cannot be taken as conclusions, the repeatable characteristics between simulations and measurements in both time and frequency domains, constitutes a basis for determining if the model converges with them and could potentially give, an easier, more predictable and accurate enough way to determine the characteristics of SRRs.

4. Chapter 4: Modeling Results and interpretations

This Chapter presents the results obtained from the linear model obtained in Chapter 2. The model is based on Marques' and Caloz's assumptions, where the cell is formed of distributed reactive elements. These cells can be approximated to lumped elements multiplied by a unit cell length. As opposed to Caloz's model, these elements are not known in advance but are determined by the permeability and permittivity equations developed by Marques (Eq 1.14 and Eq 1.16). The line characteristics and the results showed a matching behavior with metamaterial behavior as shown in paragraph 2.3.3 where a band pass filter was present, with both medium characteristics being negative for the passband. The results showed also that the group and phase velocity wee antiparallel.

In [8], Caloz considered the transmission line as linear time invariant. This means that the constitutive reactive elements of a single cell are not time-dependent. Indeed, in transmission line theory, the elements are only dependent on the length of the TL. Since we are considering a unit cell, the reactive element values are then constants. The S-parameters also being linear, S21 is the transfer function between the input and the output of the structure. Consequently, the structure constitutes a linear time-invariant system and thus, time signals can be calculated using Laplace's transform. The state-space approach is considered in order to visualize the system's states, and to be able to deduce some of the system's properties using linear control theory.

4.1. Time-Domain Results of the Model

As for the simulations, the input signal is an exponential sine of 50 ns length with a rise time of 2 ns. The frequency of the signal matches the first S21 peak,

corresponding to the first passband of the structure. As seen in figure 32 of Chapter 2, this frequency is 3.642 GHz for a one cell structure. Figure 30 shows that this frequency corresponds to a zero permeability and a negative permittivity. This frequency does not correspond to the negative asymptotic behavior of the permittivity. This is a result of the electric polarizability that induced a positive value of the permittivity at the expected resonance frequency, which associated with the negative permeability, leads to a stop band at that frequency (3.41GHz). Taking the Laplace transform of the S21 magnitude, the time output signal of the cell is obtained.

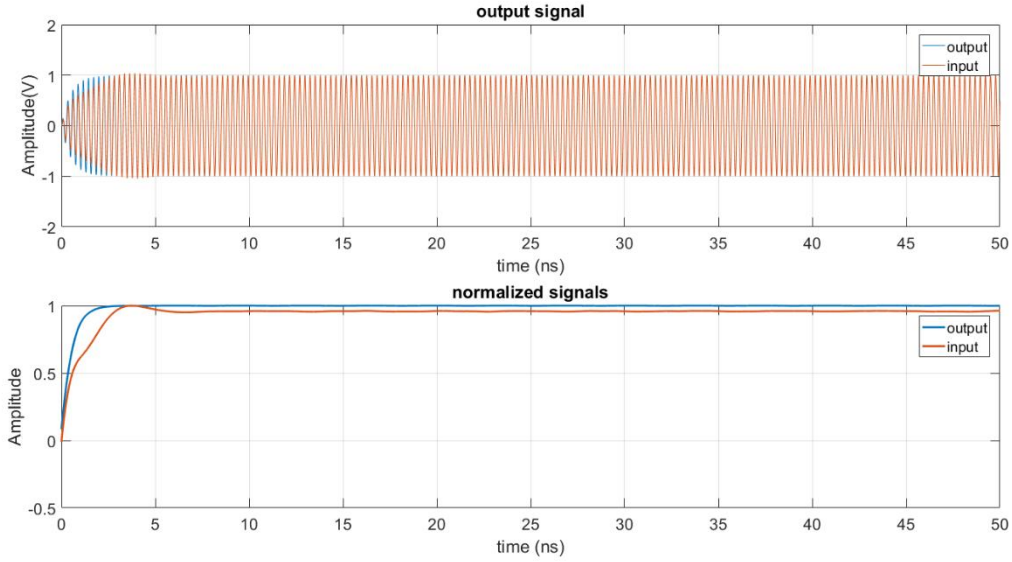

FIGURE 61: TIME SIGNALS AND ENVELOPES FOR 1 CELL STRUCTURE

In Figure 61, the output signal does not have an initial delay, confirming that the delay is the result of the WR-284 waveguides added in the structure. the reader is reminded that these waveguides are not accounted for in the model. Additionally, the output signal envelope shows two distinct rise slopes before reaching saturation. The signal reaches 50% of its maximum at 0.59 ns. The rise slope then flattens, and the signal reaches its maximum at 3.7 ns. A 3rd time constant can be considered when the signal reaches saturation. This 3rd slope is however less intuitive than the two first ones

as the signal decreases before reaching its final value. This indicates as well that the output energy exceeds the input energy at 3.7 ns, reinforcing the idea that power is stored in the cells before being delivered to the output port. The signal stabilizes at 95% of its maximum.

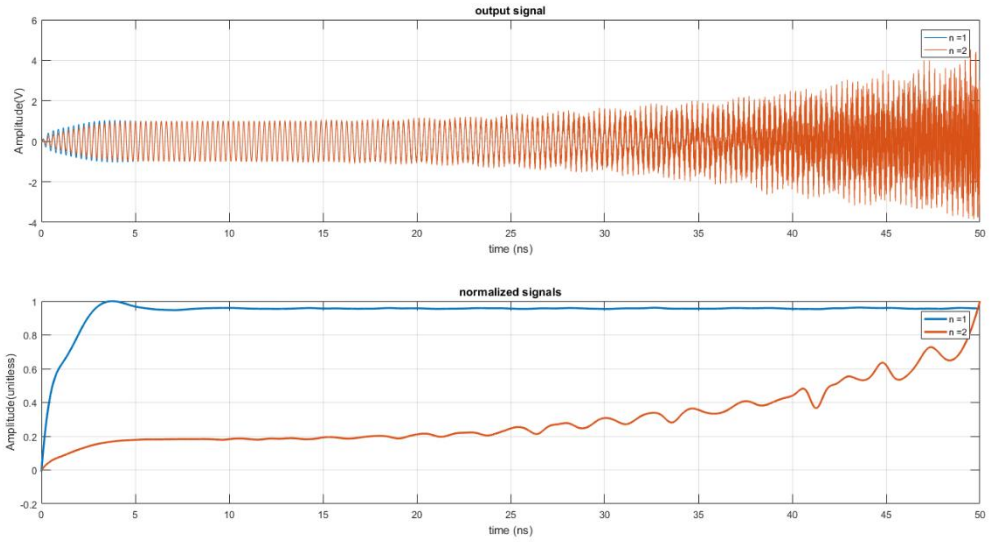

FIGURE 62: TIME SIGNALS AND ENVELOPES FOR 2 CELL STRUCTURE

In Figure 62, for the 2-cell structure, the output increases significantly. Since the system does not create energy, it is impossible to have output power that is much higher than the output. This means that the system is unstable. Looking back at the media characteristics, the frequency of the time signal is where the permeability is very close to zero and thus could be considered either positive or negative by the software. Added to that, we have in the region where resonance is supposed to happen a very high positive value that is very close to a very high negative value (asymptotic behavior of the permittivity). Since in literature, the permittivity for DNG materials is always considered negative, we remove the electric polarizability effect from the permittivity equation. The permittivity then is considered negative by considering solely the below

cutoff waveguide. The media characteristics and line properties are replotted. Figure 63 shows the permittivity and permeability of 1 and 2-cell structures over the frequency.

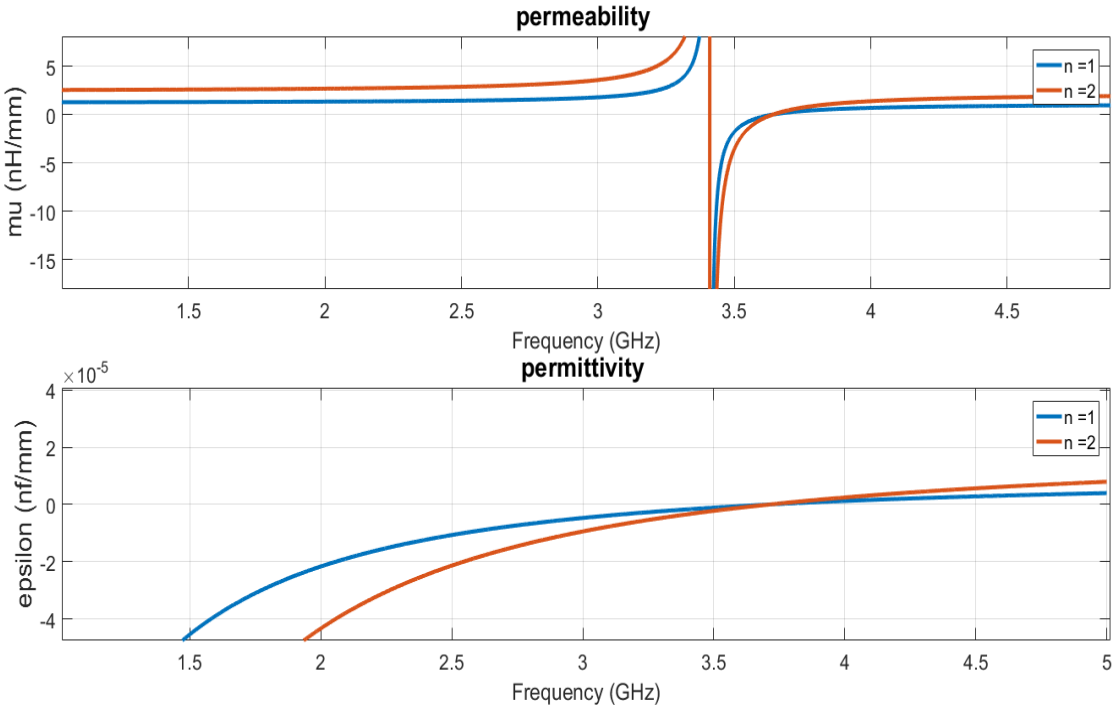

FIGURE 63: CORRECTED PERMITTIVITY AND PERMEABILITY

The figure shows clearly that the asymptotic behavior of the permittivity, caused by the electric polarizability, was removed. The permittivity is now simply negative and increases until it becomes positive at 3.714 GHz, the cutoff frequency of the waveguide. From figure 64, we note that while the dispersion graph changed. The phase and group velocity are still antiparallel for the same frequency region. However, the slope of the dispersion graph in the region gets steeper for higher frequencies. The slope for the region above cutoff is as well steeper compared to figure 31.

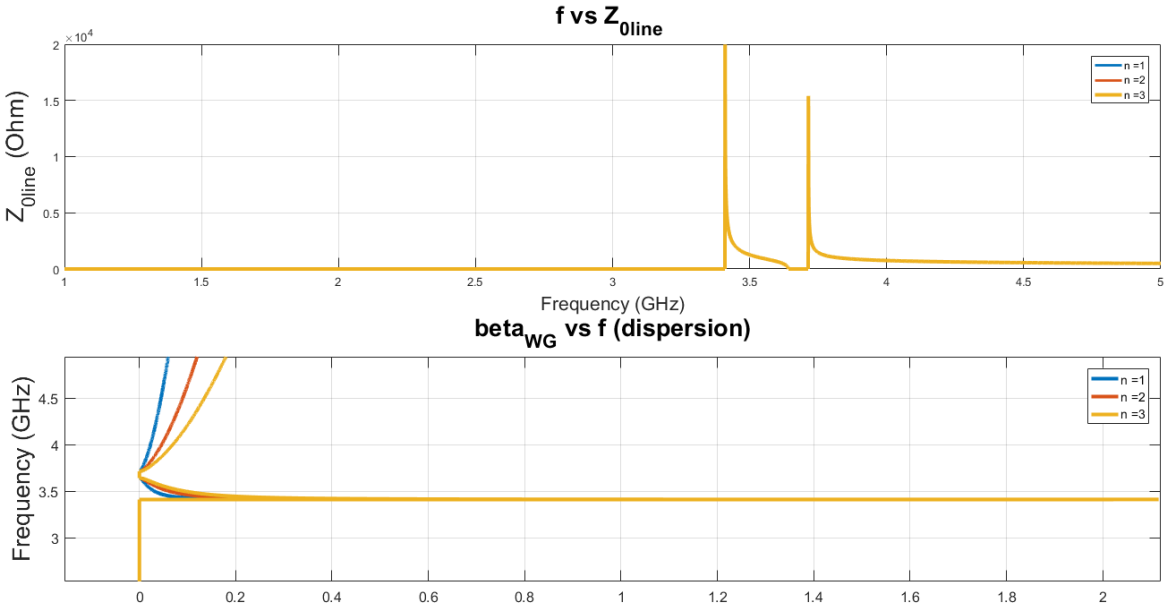

FIGURE 64: LINE CHARACTERISTICS - ADJUSTED MODEL

In figure 32, in the S21 graph, peaks very close to the resonance frequency were observed. Replotting the S-parameters with a tighter frequency band around the expected resonance frequency (3.41 GHz), all the structures show the presence of passbands.

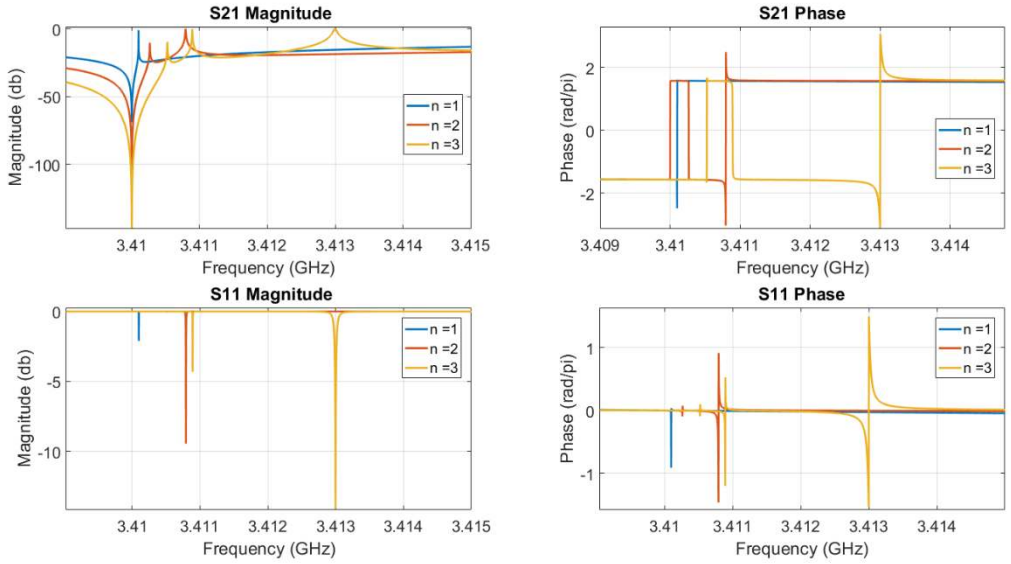

FIGURE 65: S-PARAMETERS OF THE 3 STRUCTURES

The resonance frequencies in figure 65 1, 2 and 3-cell structures are respectively 3.4101, 3.4108 and 3.4130 GHz. These values are very close to the expected resonance frequency. Additionally, for each structure, the number of peaks in S21 correspond to the number of cells in the structure. However, time signals for these values do not show a behavior that is typical of the structure studied. Due to the closeness of these values to the asymptote, and to the increased resolution of the calculated time signals, the outputs obtained in figure 66 show that the signals are evanescent, and/or unstable for a higher number of cells. In fact, the closeness to the asymptote might affect the calculations, as a higher resolution is needed to differentiate between the dip in S21 and the following peak that are very close. Moreover, the increased resolution induces calculation instabilities due to the either very high or very low coefficients of the time differential equation characterizing the structure.

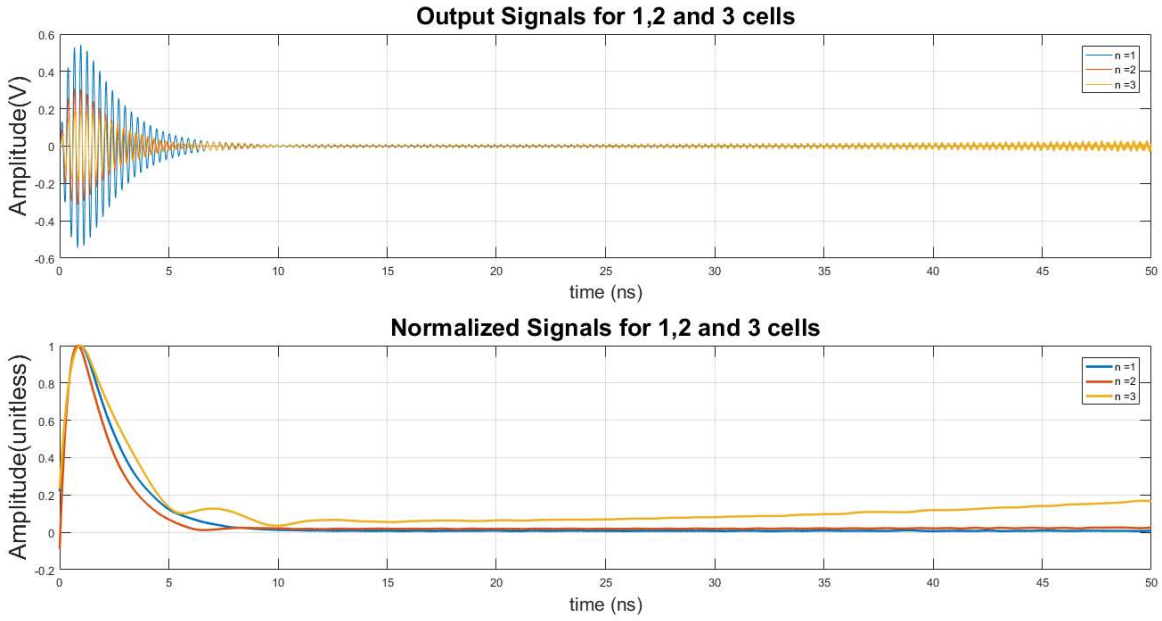

FIGURE 66: TIME SIGNALS AT 3.4101 ,3.4108 AND 3.4130 GHZ

However, decreasing the frequency resolution might cause the omission of the very narrow passband that exists and is close the asymptote. Due to software numeric limitations and to the nature of the behavior of the metamaterial medium (fast

transitions from positive to negative permittivity and permeability), a signal corresponding to the expected behavior at the expected frequency was not found. In the meantime, A higher passband was seen for a higher number of cells. Added to that, the line impedance figure shows that there is a real positive line impedance for all the structures between the expected resonance at 3.41 GHz and 3.642 GHz which is the frequency at which the impedance changes from real to imaginary (and the permeability from negative to positive). The frequencies 3.6413, 3.6411, 3.6411 are considered respectively the resonance frequencies for 1, 2 and 3 cell structures.

In the output time signals for 1 and 2 cell structures graph (figure 67), both signals are stable. In this case, the output for 2 cells has a longer rise time and its amplitude does not exceed the input's maximum amplitude. The graph shows also 3 time constants before the signal reaches its maximum at 6.35 ns. An interpretation of this could be that the energy stored by the structure is passed on from the first cell to the second, leading to a slower output signal and lower in amplitude until saturation is reached. The structure absorbs a portion of the input power until it saturates and then it passes along to the second ring during discharge. that couples part of this power out. This happens until the rings are saturated and the maximum power is sent through the output.

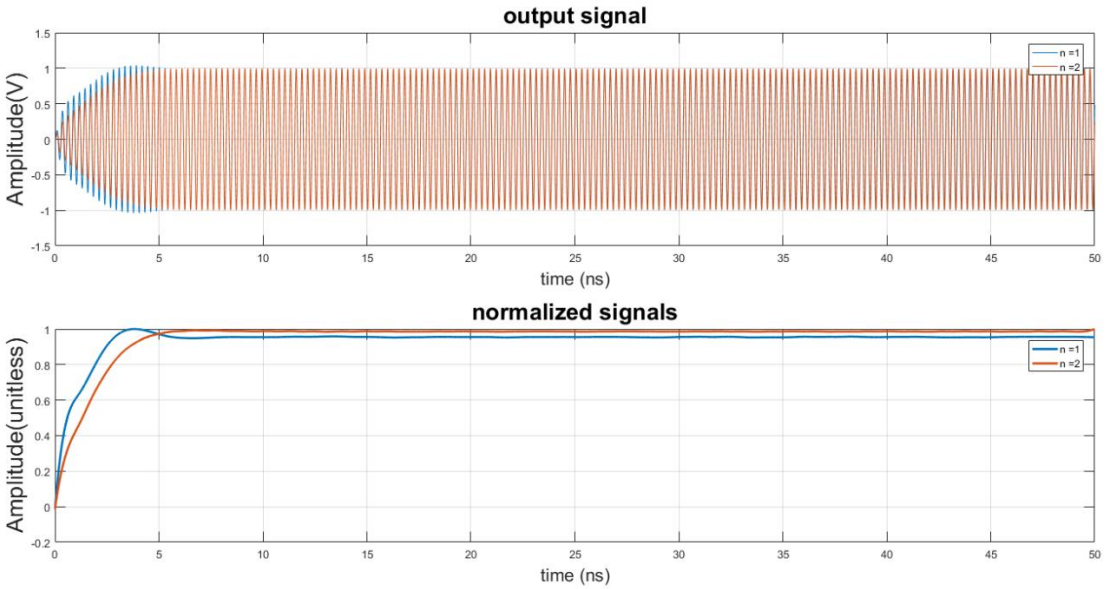

FIGURE 67: 1 AND 2 CELL TIME SIGNALS

The 3-cell structure shows a similar behavior as well. The rising slope of the signal is flatter than the previous structures and shows three distinct slopes. The signal saturates at a value greater than 99% of the input's maximum and reaches this saturation at 10.16 ns. A higher number of cells corresponds to a higher capacity of the structure to store energy, and in this case, it seems that saturation has not been reached as opposed to the 1-cell structure. As in the previous structure, the power stored in the first cell is passed on to the next cell and so on, leading to a slower output.

It is important to state that, in order to obtain a meaningful response from this system, adjustments between time resolution, frequency resolution, maximum number of cells and choice of resonant frequency must be made. All these parameters affect significantly the output signal. Several tries and corrections have been made to obtain the previously mentioned output signals, and an error margin must be considered.

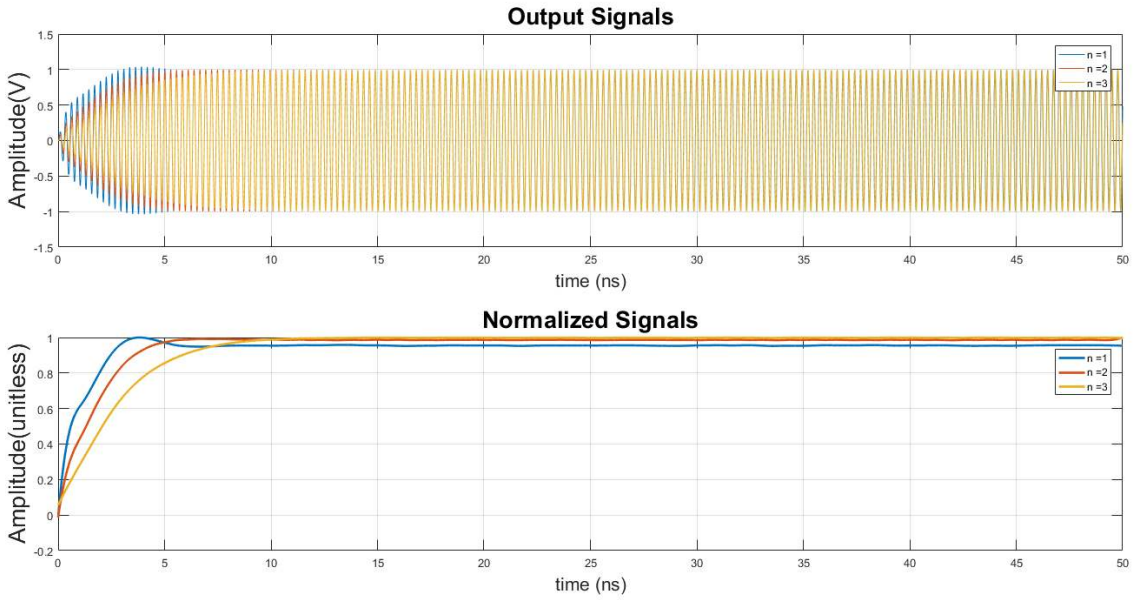

FIGURE 68: TIME SIGNALS OF THE 3 STRUCTURES

For a closer analysis of the time domain features, a gaussian pulse input is set for the same 1,2 and 3 cell structures. The gaussian pulse has a center frequency corresponding to the resonance frequency, a span going from – 50 to 50 ns and a fractional bandwidth of 0.5. The pulse is then shifted by 5ns. In figure 69, normalized gaussian pulses and their envelopes are observed.

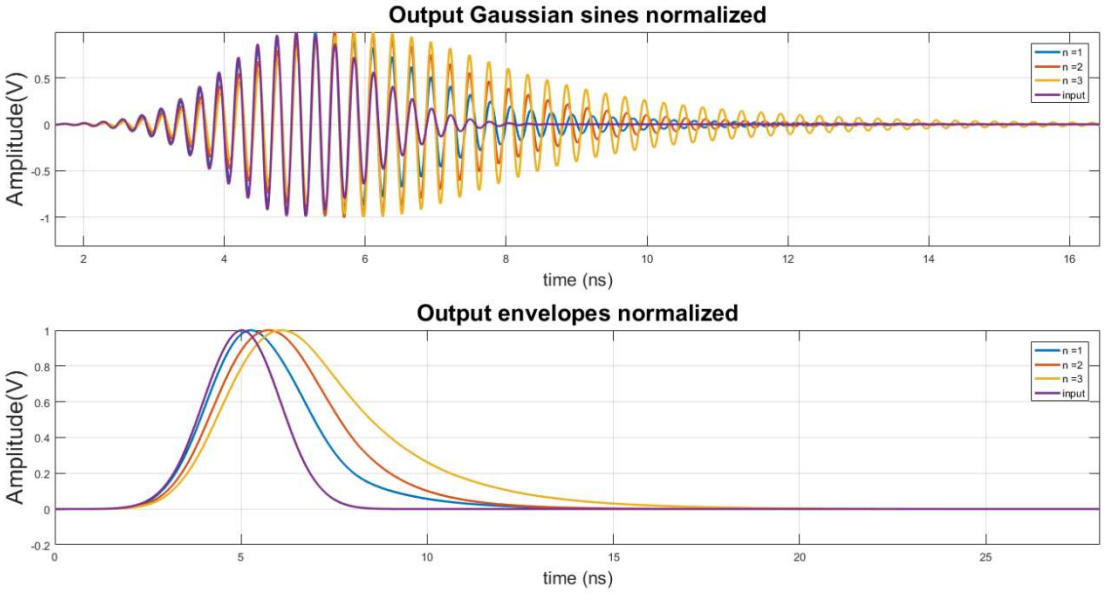

FIGURE 69: TIME GAUSSIAN SIGNALS FOR THE 3 STRUCTURES

The pulse figure shows several features observed previously. The envelopes show a flatter rise time for increased number of cells. The decay of the envelopes also show that the decay time significantly slows down with the number of cells, and the presence of multiple time constants. Looking at the peaks of the envelopes, we note that the peaks of the output signals are delayed compared to the input, suggesting an increased group delay with a higher number of cells, corresponding to a lower group velocity. However, the delay between the 2 and 3 cell structure is smaller than the delay between 1 and 2 cells, indicating that the group delay is not proportional to the number of cells. In the sinusoidal signals' figure, the increased oscillations with the number of cells are obvious. Zooming on the sine peaks of the signals show in the beginning of the pulse, that the input's peaks are leading, followed by the 1, 2 and 3 cell structures. The output signals however, compensate this delay over time and we can see the phase changing. The delay compensation is more important with number of cells. When the signals decay, the 3-cell structure signal is leading, followed by the 2. 1 cell signals and finally the input. This phenomenon coupled with the previous observations are another indicator of negative phase velocity and group phase velocity.

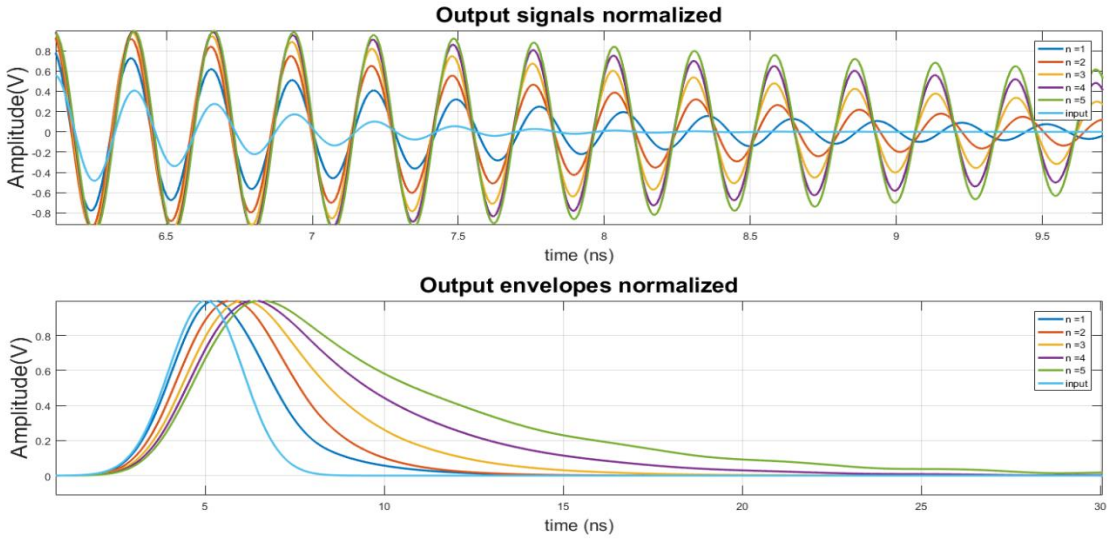

FIGURE 70: GAUSSIAN TIME SIGNALS FOR 5 CELLS

The number of cells is increased to 5 in figure 70 to verify if the previous claims hold for a higher number of cells. By zooming on the sinusoidal gaussian figure, the phase delay shifts from positive to negative between input and outputs. It is noted also that the phases of the signals for 4 and 5 cells are close and almost equal. In the envelope figure, the previous trends are confirmed, and we see the group delay increasing between input and outputs while decreasing between two consecutive output signals.

4.2. State-space approach of the model

A closer look into the state-space aspect of the model is taken in this section. The model, as explained previously, being LTI (linear time-invariant), S21 can be considered as the transfer function and can be transformed using Laplace's transform into a system of differential equations describing the state of the system. This system being single-input single-output, the states calculated are the derivatives of the main state. This means that a single differential equation can describe the system. However, using state-space system enables us to deduce a few properties that are useful for understanding the model and the system.

We must note also that since S-parameters are being used, cascading the transfer functions will not lead to the response for multiple cells, the input and output impedances for each system with any number of cells have to be included in the transfer function. A general form for a state-space system is

$$\begin{cases} \dot{x} = A\,x + B\,u \\ y = C\,x + D\,u \end{cases}$$

Where x, y, A, B, C, D and u represent respectively, the state vector, the output vector, the state matrix, the input matrix, the output matrix, the feedthrough matrix and the input vector. The input and output in this case are signals, thus, the vectors and matrices here are reduced to one-dimension. We also remind that since the system is LTI, A, B,

C and D are constants. The stability of the system is easily deduced from the eigenvalues of A, the state-matrix. These eigenvalues equivalent to the poles of S21. The real part of the eigenvalues must be negative for the system to be stable, and the closer they are to zero, the closer to marginal stability the system becomes. The output signal's oscillations are then increased before reaching stability. For a 1, 2 and 3-cell structures, the state-space system have respectively 8, 12 and 16 states. All the eigenvalues have negative real parts which indicates that the systems are stable. However, some of the real parts of eigenvalues of these systems are very small and close to zero, which increases the oscillations in the system and drives it towards a marginal stability. In fact, the number of eigenvalues that are between -1 and 0 is 5, 7 and 9 for the 1,2 and 3 cell structures. At the 4^{th} cell, eigenvalues with positive real parts exist and the system becomes unstable. These results depend on the resolution of MATLAB and on the scale of the system. In fact, the size of the system increases with the number of cells and the Matrices coefficients become very high and can drive the memory to overflow and bias the response. Theoretically, since for any number of cells in the structure output exists, then the system should always be stable. The instabilities in the calculation are then attributed to software and numerical errors. Nevertheless, the 1, 2 and 3 cell model state-space systems give an indication about the complexity of the system and the caution that needs to be used, to not drive the system to instabilities. Normalization to avoid these problems have been applied to the system. Added to that, observability and controllability properties of the system can be derived. These matrices determine how many states of the system can be controlled and/or seen. While the controllability gives an indication about a potential feedback that we can apply to the system to change its properties, observability gives an indication about the number of states that are enabled for observation to see the output. In this case, the output is always

available through measurement, and thus, the observability matrix gives an indication about the observable states, corresponding in this case to the derivatives of the output. For the 1-cell structure, the controllability and observability matrices are rank-deficient, meaning that the system is neither controllable nor observable. These results are however altered by the coefficients of the matrices as the controllability matrix has a coefficient of 10^18 and the observability matrix has a coefficient of 10^29. These values can be critical for establishing the rank of the system. The coefficients of these matrices keep increasing with the number of cells as the system gets bigger. The controllability matrix gives a great indication on the number of controllable states in the system. This information can be used to potentially stabilize the system or control its performances for a faster response.

4.3. Comparison between simulation, measurements and model

All the simulation, experiment and model share multiple metamaterial characteristics between each other. The model and simulation have shown similar behavior in both frequency and time domains. In both configurations, the S-parameter figures show a dip followed by a peak corresponding to the asymptotic behavior of the system. While the values of these peaks do not necessarily match in value, we need to take into account the fact that the model does not consider the input and output WR-284 waveguides. From the experimental measurements, a passband is seen around 2.9 GHz. This passband is far from the expected resonance but is still reasonable considering the losses and the impedance mismatch caused by the ring and the cross section change between the WR-284 waveguides and WR-159 section. However, in the time-domain figures, interpretation is a little more delicate as the resolution is not high enough and losses are increased. The rise curves however are harder to interpret due to their closeness even though the envelope of the 3-cell curve is delayed in regard with

the 2 and 1-cell structure plots. Output peaks leading the input signal peaks were observed in the measurements as well as in the model. This feature has been observed as well in the simulation and confirms the negative phase velocity in all the configurations. The output sine peaks are at first delayed compared to the input but as the signal grows, these peaks become leading. Looking back at the S-parameter figures of the model, a change of the sign of the S-parameter phase is observed at the resonance and could explain the change in phase between the input and the output. While this is not necessarily the cause of the change in delay, it still shows an interesting behavior that could be analyzed more thoroughly. It is also reasonable to expect that the metal inclusions that constitute the rings would result in multiple reflections changing the phase of the signal while it travels along the structure.

Signals in simulation and model have shown a common behavior where the output signal exceeds the maximum of the input giving a hint about energy storage in the structure. Besides that, the oscillations increased with the number of cells. The model showed how this is related to the dynamics of the system which get more complicated with the number of cells. Stability is as well affected by the number of cells as the settling time increases with the number of cells. The measured signals, however, did not show instabilities. It is important to note as well that for the measured signals, losses are much higher which contribute in changing the dynamics of the system and potentially stabilizing it.

4.4. Interpretation and possible explanation

Based on the data collected during this work, and previous research work done, a physical explanation can be deduced. While there's partial convergence in the results,

this explanation remains a result of observations and cannot be asserted without further research to support it. If the model correctly emulates the structure's behavior, when an incident signal hits the structure, the first cell, which is a combination of inductances and a capacitance, will store a portion of the incident energy. The diamagnetic response, resulting in a negative permeability, a current in the inductors. This current flowing through the capacitor, transforms into a capacitive energy stored between the armatures of the capacitor, which are the edges of the rings in a single SRR cell in this case. At the time of discharge, the capacitor is saturated, and the energy is released leading to a current flowing through the second inductor that maintains the diamagnetic response across the structure and delivers power to the output. The output signal seen is the superposition of the released stored energy added to the signal flowing in the structure. This superposition leads to an output that can exceed the maximum of the input for a small period. The signal is as well delayed by this oscillatory behavior. Adding more cells to the structure, this behavior is maintained, adding more oscillations. In fact, the energy stored in the first cell is released and restored by the second cell and so on, slowing the propagation down. A stable output will be obtained once all the rings are saturated. The overall storage capacity will increase with the number of cells which explains the slowed rise time of the output when the number of cells is increased. This interpretation matches the explanation given in [17] and based on field simulation observations.

5. Conclusion and Future Work

5.1. Summary and Conclusion

The main goal of this thesis was to get more understanding of the time behavior of metamaterials in general and split-ring resonator in particular. For this purpose, experiments were conducted and analyzed, several simulations were run, and a model has been developed in an attempt to emulate and predict the SRR in a below-cutoff waveguide. In all these different configurations, the analysis emphasized on asymptotic behavior of the metamaterial, where the permeability and subsequently, the diamagnetic response change significantly in a very small bandwidth and creates the desired phenomenon. Discrepancies existed between simulation, measurements and model due to systematic and random errors that reside in losses, instrument coupling, random parameters or software errors and limitations. However, agreement was found between the three configurations:

- Frequency-domain results showed similar behavior and comparable resonance frequencies; 3.3 GHz, 2.82 GHz and 3.41 GHz for respectively, the simulation, measurement and model. The shift in the resonance for the measurement is due to losses and to the different errors emanating from the experimental setup
- Phase and group velocity showed an antiparallel behavior for the experimental results and the model results. These results confirm the presence of a backward wave in the structure
- The rise time of the time-signals in all the configurations is composed of three time constants/slopes. The initial delay in the output signals is not caused by the SRRs but rather by the input and output WR-284. Increasing the number of cells leads to a slower rise time. This is attributed to the energy storage in the rings.

All the systems all showed that the diamagnetic response was increased with the number of cells inducing less oscillations around the saturation value but also a longer rise time due to the increased overall storage capacity of the whole structure. Since the magnetic field induced by the diamagnetic response is perpendicular to the cross-section of the rings, it is expected that the diamagnetic response increases when cells are stacked in the direction of the magnetic field. However, all simulations, model and measurements demonstrated that the permittivity, the diamagnetic response is higher when the cells are increased longitudinally. Added to that, the model exhibited the effect of the electromagnetic polarizability on the structure, which adds more complexity to the behavior of the SRRs. In fact, the electromagnetic polarizability has a non-negligible effect on the permittivity and induces a change in the passbands and stop bands of the structure based on the sign change of the permittivity. These changes happen in a frequency region very close to resonance and drives the model to instability. This can be an indicator that a simple LTI circuit is not enough to emulate the structure with a high precision level. It is necessary to remind the reader as well that the system might have multiple reflections inside the structures, which should be represented by a feedback in the LTI system. This feedback can have an effect on the stability of the system. Nevertheless, the simple LTI model for emulating the structure is very useful for its simplicity, but also for the features that if offers from a control system perspective, where the time characteristics could be manipulated to track a reference or to a certain desired behavior. Multiple other aspects in the model could be focused on, like the abrupt phase change seen at the resonance in the S-parameters.

Looking back at the model inspired from Caloz and Marques, the nature of the inductive elements is not determined, as opposed to Caloz's LHTL or CRLHTL. However, the permeability, permittivity and reactances of the cell elements can be determined using

$$\begin{cases} Z' = j\omega\mu \\ Y' = j\omega\varepsilon \end{cases}$$

In fact, looking at figure 71, the reactances follow the same behavior as the medium characteristics. Z'has an asymptote at $f_\omega = 3.41GHz$ and crosses the x-axis at $f_0 = 3.642\ GHz$. Y' crosses the x-axis at the cutoff frequency, corresponding to $f_{WG} = 3.71\ GHz$.

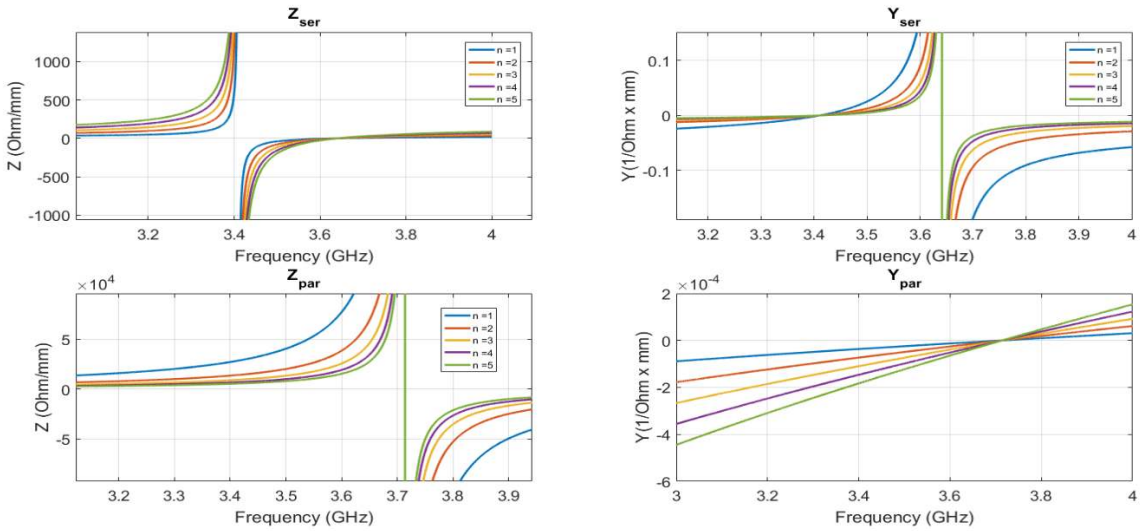

FIGURE 71: IMPEDANCES AND ADMITTANCES OF ELEMENTS OF STRUCTURE

The model of a simple cell constituted of one reactance in series and one reactance in parallel, the following sign table is deduced

f	f_ω	f_0	f_{WG}
Z'	+ + + ∞ - - -	0 + + + + + +	
Y'	- - - - - - -	- - - - 0 +	

For $f < f_\omega$ and $f > f_{WG}$, Z' is positive and the behavior is mainly inductive, while it is capacitive for $f_\omega < f < f_0$. The sign of Z', shows that it has at least one zero at f_0 and at least one pole at fw while Y' has only a zero at f_{WG}.

$$Z' = \frac{K(1-\left(\frac{f}{f_0}\right)^i)}{(1-\left(\frac{f}{f_\omega}\right)^j)}$$

With K a coefficient and i and j two positive integers representing the orders of the polynomials.

For Y' we obtain

$$Y' = K'(\left(\frac{f}{f_{WG}}\right)^k - 1)$$

By simply putting Z' as a series impedance and Y' as a parallel admittance in a cell, the transfer function is obtained

$$T = \frac{Z'Y'}{Z'Y' + 1}$$

$$T = \frac{\frac{K(1-\left(\frac{f}{f_0}\right)^i)}{(1-\left(\frac{f}{f_\omega}\right)^j)} \times K'(\left(\frac{f}{f_{WG}}\right)^k - 1)}{\frac{K(1-\left(\frac{f}{f_0}\right)^i)}{(1-\left(\frac{f}{f_\omega}\right)^j)} \times K'(\left(\frac{f}{f_{WG}}\right)^k - 1) + 1}$$

While these equations do not determine the lumped element values, they can be used in a genetic algorithm with different i, j and k coefficients to determine the values of the reactances of the cell. The model created lays the ground for time-domain analysis research work as well as control system oriented research for controlling the time characteristics of the structure

5.2. Future Work

Several questions from this research work can be raised and answered to get a better explanation of the interaction of the rings with the incident wave

- The effect of the losses on the system and its impact on the stability and the states can be studied. Losses have as well an effect on the rise time and energy storage capabilities of the system. Also, with adding losses to the model, a backwards approach could be taken by considering the model and building a structure having the distributed element properties of the model.

- From the modeling perspective, feedback can be applied to the system as a way of stabilizing it or to modify its time response. A version of the system at lower frequencies could be studied to avoid the numeric limitations faced during this work. This could help as well to study systems with a higher number of cells to confirm the behaviors seen in the 1,2 and 3-cell structures.

- Understanding discrepancies between simulations, measurements and model is also important. Adding delay to the simulation and to the model that would account for the systematic error of the experimental set-up could help determine the origin of the random component of the errors.

References

[1] J. B. Pendry, A. J. Holden, D. J. Robbins, and W. J. Stewart, “Magnetism from Conductors and Enhanced Nonlinear Phenomena,” IEEE Trans. Microw. Theory Tech., vol. 47, no. 11, pp. 2075-2084, 1999.

[2] D.R. Smith, D.C. Vier, N. Kroll, and S. Schultz, “Direct calculation of permeability and permittivity for a left-handed metamaterial”, Appl. Phys. Lett, vol. 77, no. 14, pp. 2246-2248, 2000.

[3] Shelby, R. A., D. R. Smith, and S. Schultz. "Experimental Verification of a Negative Index of Refraction.", Science, vol. 292 no.77, pp. 77-79, 2001.

[4] D. R. Smith, D. Schurig, and J. B. Pendry, “Negative refraction of modulated electromagnetic waves”, Appl. Phys. Lett, vol. 81, no. 15, pp. 2713-2715, 2002.

[5] S. Foteinopoulou, E. N. Economou, and C.M. Soukoulis, “Refraction in Media with a Negative Refractive Index”, Phys. Rev. Lett., vol. 90, no. 10, pp. 107402-1- 107402-4, 2003.

[6] R. Marqués, J. Martel, F. Mesa, and F. Medina1, “Left-Handed-Media Simulation and Transmission of EM Waves in Subwavelength Split-Ring-Resonator-Loaded Metallic Waveguides”, Phys. Rev. Lett., vol. 89, no. 18, pp. 83901-1- 83901-1, 2002.

[7] C. Caloz and T. Itoh, “Transmission Line Approach of Left-Handed (LH) Materials and Microstrip Implementation of an Artificial LH Transmission Line,” IEEE Trans. Antennas Propag., vol. 52, no. 5, pp. 1159-1166, 2004.

[8] A. Lai, C. Caloz, and T. Itoh, “Composite Right/Left-Handed Transmission Line Metamaterials,” IEEE Microwave Mag., vol. 5, no. 3, pp. 34 - 50, 2004.

[9] D. Shiffler, R. Seviour, E. Luchinskaya, E. Stranford, W. Tang, and D. French, "Study of split-ring resonators as a metamaterial for highpower microwave power transmission and the role of defects," IEEE Trans. Plasma Sci., vol. 41, no. 6, pp. 1679–1685, 2013.

[10] S. Hrabar, J. Bartolic, and Z. Sipus, "Waveguide miniaturization using uniaxial negative permeability metamaterial," IEEE Trans. Antennas Propag., vol. 53, no. 1, pp. 110–119, 2005.

[11] I. McGregor and K. M. Hock, "Complementary split-ring resonator coupled traveling wave accelerating structure," Phys. Rev. Special Topics-Accel. Beams, vol. 16, no. 8, p. 080102, 2013.

[12] J. B. Pendry, "Negative refraction makes perfect lens." Phys. Rev. Lett., vol. 85, pp. 3966–3969, 2000.

[13] R. Marqués, M. Ferran and M. Sorolla. "Metamaterials with Negative Parameters," John Wiley & Sons, Inc., 2008.

[14] D. M. Pozar, "Microwave Engineering," 4th edition. John Wiley & Sons, Inc., 2012.

[15] V. G. Veselago, "The Electrodynamics of Substances with Simultaneously Negative Values of ε and μ," USPEKHI, vol. 4, pp. 509–514, 1968.

[16] R. Marqués, F. Mesa, J. Martel, and F. Medina, "Comparative analysis of edge- and broadside-coupled split ring resonators for metamaterial design—Theory and experiment," IEEE Trans. Antennas Propag., vol. 51, no. 10, pp. 2572–2581, 2003.

[17] T. Wynkoop, "Design and Characterization of Split-Ring Resonator Arrays in Waveguide", M.S. thesis, Univ. of New Mexico, Albuquerque, NM, USA, 2015.

[18] G. F. Craven, C. K. Mok, “The Design of Evanescent Mode Waveguide Bandpass Filters for a Prescribed Insertion Loss Characteristic IEEE Trans. Microw. Theory Tech., vol. 19, no. 3, pp. 295-308, 1971.

[19] R. W. Ziolkowski, E. Heyman, “Wave propagation in media having negative permittivity and permeability,” Phys. Rev. E 64, 056625, pp. 1-15, 2001.

[20] E. A. Semouchkina, G. B. Semouchkin, M. Lanagan and C. A. Randall, “FDTD Study of resonance Processes in Metamaterials,” IEEE Trans. Microw. Theory Tech., vol. 53, no. 4, pp. 1477-1487, 2005.

[21] T. Kokkinos, C. D. Sarris and G. V. Eleftheriades, “Finite-difference time-domain analysis of metamaterial-based leaky-wave antennas”, Antennas and Propagation Society Int. Symp., Washington, DC, USA, 2005, pp 26-29

[22] J.S. Gómez-Díaz, S. Gupta A. Alvarez-Melcon and C. Caloz, Efficient time-domain analysis of highly dispersive linear and non-linear metamaterial waveguide and antenna structures operated in the impulse-regime, IET Microw. Antennas Propag, vol.4, no. 10, pp 1617-1625, 2010.

[23] A. Grbic and G. V. Eleftheriades, “Waveguide miniaturization using uniaxial negative permeability metamaterial,” IEEE Trans. Antennas Propag., vol. 51, no. 10, pp. 2604–2611, 2003.

[24] P. P. M. So and W. J. R. Hoefer, “Time Domain TLM Modeling of Metamaterials with Negative Refractive Index”, Microw. Symp. Dig., Fort Worth, TX, USA, pp 1779-1782, 2004

[25] T. Kokkinos, R. Islam, C. D. Sarris, G. V. Eleftheriades, “Rigorous Analysis of Negative Refractive Index Metamaterials Using FDTD with Embedded Lumped Elements”, Microw. Symp. Dig., Fort Worth, TX, USA, pp 26-29, 2004

[26] S. Erickson, J. Wong, T. Kokkinos, C.D. Sarris, “Modeling of metamaterial structures using an extended finite-difference time-domain (FDTD) approach”, IEEE/ACES Int. Conf. on Wireless Communications and Applied Computational Electromagnetics, 2005.